The Astrophysical Journal, 998:86 (51pp), 2026 February 10 https://doi.org/10.3847/1538-4357/ae2c60

On the Use of Field RR Lyrae as Galactic Probes. VIII. Early Formation of the Galactic Spheroid*

G. Bono[1,2], V. F. Braga[2], M. Fabrizio[2,3], M. Tantalo[2], K. Baeza-Villagra[1,2], J. Crestani[1], V. D'Orazi[1,4], M. Dall'Ora[5], M. Di Criscienzo[2], G. Fiorentino[2], M. Gholami[5], M. Marengo[6], C. E. Martínez-Vázquez[7], M. Monelli[2,8,9], J. P. Mullen[10], A. Nunnari[1,2], V. D. Pipwala[1,2], Z. Prudil[11], C. Sneden[12], G. Altavilla[2,3], M. Bergemann[13], G. Böcek Topcu[1,2], R. Buonanno[2], A. Calamida[14], E. Carretta[15], G. Ceci[1,2,16], B. Chaboyer[17], M. Correnti[2,3], R. da Silva[2,3], I. Ferraro[2], F. A. Gómez[18], G. Iannicola[2], R.-P. Kudritzki[19,20], A. Kunder[21], S. Kwak[22], M. Marconi[5], S. Marinoni[2,3], N. Matsunaga[23], F. Matteucci[24,25,26], A. Monachesi[18], I. Musella[5], M. G. Navarro Ovando[2], G. W. Preston[27], V. Ripepi[5], M. Salaris[28,29], M. Sánchez-Benavente[8,9], E. Spitoni[24], P. B. Stetson[30], F. Thévenin[31], I. B. Thompson[27], P. B. Tissera[32,33], T. Tsujimoto[34], E. Valenti[11,35], A. K. Vivas[36], A. R. Walker[36], M. Zoccali[32,37], and A. Zocchi[38]

[1] Dipartimento di Fisica, Università di Roma Tor Vergata, via della Ricerca Scientifica 1, I-00133 Roma, Italy; bono@roma2.infn.it
[2] INAF—Osservatorio Astronomico di Roma, via Frascati 33, I-00078 Monte Porzio Catone, Italy
[3] ASI—Space Science Data Center, via del Politecnico snc, I-00133 Roma, Italy
[4] INAF—Osservatorio Astronomico di Padova, vicolo dell'Osservatorio 5, I-35122 Padova, Italy
[5] INAF—Osservatorio Astronomico di Capodimonte, Salita Moiariello 16, I-80131 Napoli, Italy
[6] Florida State University, Department of Physics, 77 Chieftain Way, Tallahassee, FL 32306, USA
[7] NSF NOIRLab, 670 N. A'ohoku Place, Hilo, Hawai'i 96720, USA
[8] Instituto de Astrofísica de Canarias, Calle Via Lactea s/n, E-38205 La Laguna, Tenerife, Spain
[9] Departamento de Astrofísica, Universidad de La Laguna (ULL), E-38200, La Laguna, Tenerife, Spain
[10] Department of Physics and Astronomy, Vanderbilt University, Nashville, TN 37240, USA
[11] European Southern Observatory, Karl-Schwarzschild-Straße 2, D-85748 Garching, Germany
[12] Department of Astronomy and McDonald Observatory, The University of Texas, Austin, TX 78712, USA
[13] Max-Planck-Institut für Astronomie, Königstuhl 17, D-69117 Heidelberg, Germany
[14] Space Telescope Science Institute, 3700 San Martin Drive, Baltimore, MD 21218, USA
[15] INAF - Osservatorio di Astrofisica e Scienza dello Spazio di Bologna, Via P. Gobetti 93/3, I-40129 Bologna, Italy
[16] Dipartimento di Fisica, Sapienza Università di Roma, Piazzale Aldo Moro 5, I-00185 Roma, Italy
[17] Department of Physics and Astronomy, Dartmouth College, 6127 Wilder Laboratory, Hanover, NH 03755, USA
[18] Departamento de Astronomía, Universidad de La Serena, Avenida Raúl Bitrán 1305, La Serena, Chile
[19] Institute for Astronomy, University of Hawai'i at Manoa, Honolulu, HI 96822, USA
[20] LMU München, Universitätssternwarte, Scheinerstraße 1, 81679 München, Germany
[21] Saint Martin's University, 5000 Abbey Way Southeast, Lacey, WA 98503, USA
[22] Leibniz Institut für Astrophysik Potsdam (AIP), An der Sternwarte 16, D-14482 Potsdam, Germany
[23] Department of Astronomy, School of Science, The University of Tokyo, 7-3-1 Hongo, Bunkyo-ku, Tokyo 113-0033, Japan
[24] INAF—Osservatorio Astronomico di Trieste, via G.B. Tiepolo 11, I-34131 Trieste, Italy
[25] Dipartimento di Fisica, Sezione di Astronomia, Università di Trieste, Via Giovanni Battista Tiepolo 11, I-34143 Trieste, Italy
[26] INFN—Sezione di Trieste, via Valerio 2, I-34134 Trieste, Italy
[27] Carnegie Observatories, 813 Santa Barbara Street, Pasadena, CA 91101-1292, USA
[28] Astrophysics Research Institute, Liverpool John Moores University, 146 Brownlow Hill, Liverpool L3 5RF, UK
[29] INAF—Osservatorio Astronomico d'Abruzzo, via M. Maggini, s/n, I-64100, Teramo, Italy
[30] Herzberg Astronomy and Astrophysics, NRC, 5071 West Saanich Road, Victoria, British Columbia V9E 2E7, Canada
[31] Université de Nice Sophia-Antipolis, CNRS, Observatoire de la Côted'Azur, Laboratoire Lagrange, BP4229, F-06304 Nice, France
[32] Instituto de Astrofísica, Pontificia Universidad Católica de Chile, Avenida Vicuña Mackenna 4860 Santiago, Chile
[33] Centro de AstroIngeniería, Pontificia Universidad Católica de Chile, Avenida Vicuña Mackenna 4860, Santiago, Chile
[34] National Astronomical Observatory of Japan, Mitaka, Tokyo 181-8588, Japan

* Based in part on observations made with the Southern African Large Telescope (SALT): Program IDs: 2017-2-SCI-041, 2018-1-SCI-018, 2018-2-SCI-025, 2019-1-SCI-013, 2021-2-SCI-028, 2022-2-DDT-001, PI: B. Chaboyer). Based in part on data obtained in the Observatorios de Canarias del Instituto de Astrofisica de Canarias (IAC) with: the STELLA robotic telescope, an AIP facility jointly operated by AIP and IAC at the Teide Observatory in Tenerife, Spain; the Italian Telescopio Nazionale Galileo (TNG) operated by the Fundación Galileo Galilei of the INAF, the Nordic Optical Telescope (NOT) owned in collaboration by the University of Turku and Aarhus University and operated jointly by Aarhus University, the University of Turku and the University of Oslo, representing Denmark, Finland and Norway, the University of Iceland and Stockholm University, and the Mercator telescope operated by the Flemish Community, all at the Observatorio del Roque de los Muchachos of the IAC, La Palma, Spain (Program IDs: 101-MULTIPLE-4/21B, 107-MULTIPLE-4/22A, 120-MULTIPLE-2/23B, 165-Stella12/20A, PI: M. Monelli; Program ID: 108-MULTIPLE-2/25B, PI: M. Sánchez-Benavente).

[35] Excellence Cluster ORIGINS, Boltzmann-Straße 2, D-85748 Garching bei München, Germany
[36] Cerro Tololo Inter-American Observatory/NSF NOIRLab, Casilla 603, La Serena, Chile
[37] Millennium Institute of Astrophysics, Avenida Vicuña Mackenna 4860, Santiago, Chile
[38] Department of Astrophysics, Türkenschanzstraße 17 (Sternwarte), 1180 Wien, Austria
Received 2025 October 6; revised 2025 November 19; accepted 2025 November 26; published 2026 February 4

Abstract

We introduce a new photometric catalog of RR Lyrae (RRL) variables (∼300,000) mainly based on data available in public datasets. We also present the largest and most homogeneous spectroscopic dataset of RRLs and blue horizontal branch (BHB) stars ever collected. This includes radial velocity measurements (∼16,000) and iron abundances (ΔS method for 8140 RRLs, plus 547 from literature). Elemental abundances based on high-resolution spectra are provided for 487 RRLs and 64 BHB stars. We identified candidate RRLs associated with the main Galactic components and their iron distribution function (IDF) becomes more metal rich when moving from the halo ([Fe/H] = −1.56) to the thick disk (TCD; [Fe/H] = −1.47) and thin disk (TND; [Fe/H] = −0.73). Furthermore, halo RRLs and RRLs in retrograde orbits are α enhanced ([α/Fe]=0.27, σ = 0.18), while TCD RRLs are either α enhanced ([Fe/H] $\leqslant -1.0$) or α poor ([Fe/H] > -1.0), and TND RRLs are mainly α poor ([α/Fe] = −0.01, σ = 0.20). We also identified RRLs associated with the main stellar streams—Gaia–Sausage–Enceladus (GSE); Sequoia, Helmi, and Sagittarius—and we found that their IDFs are quite similar to halo RRLs. However, GSE RRLs lack the metal-poor/metal-rich tails and their α-element distribution is quite compact. The iron radial gradient in Galactocentric distance for TND, TCD, and halo RRLs is negative and it decreases from −0.026, to −0.010, and to −0.002 dex kpc^{-1}. The iron radial gradient based on dry halo (halo without substructures) RRLs is, within the errors, equal to the global halo. We also found a strong similarity between iron and [α/Fe] radial gradients of Milky Way RRLs and M31 globular clusters throughout the full range of galactocentric distances covered by the two samples.

Unified Astronomy Thesaurus concepts: RR Lyrae variable stars (1410); Milky Way dynamics (1051); Milky Way evolution (1052); Chemical abundances (224); Metallicity (1031)

Materials only available in the online version of record: machine-readable tables

1. Introduction

In spite of the relevant improvements in the understanding of the early formation and evolution of Milky Way (MW), we still lack a "canonical" model, i.e., a comprehensive view of the physical mechanisms and timescales behind the formation of the old Galactic component (halo). The two most popular theories concerning the early formation of the stellar halo date back to more than 40 yr ago. The first was introduced by O. J. Eggen et al. (1962) and suggests a dissipative process on a rapid timescale, while the second was suggested by L. Searle & R. Zinn (1978) and relies on a dissipationless hierarchical mechanism and a slower formation.

A modern approach to cast this long-standing problem is to establish on a quantitative basis the fraction of stars that formed in situ from those that were accreted (or formed ex situ). In a dissipative scenario, a significant fraction of the halo stellar content was formed inside the Galaxy in the early epochs of its formation (A. Zolotov et al. 2009; A. P. Cooper et al. 2015). In a dissipationless scenario, a (significant) fraction of the halo stellar content was formed ex situ by the accretion and tidal disruption of dwarf galaxies. The latter mechanism is the hierarchical assembly predicted by cold dark matter (CDM) cosmological models (J. S. Bullock & K. V. Johnston 2005; A. S. Font et al. 2011) and it is an ongoing mechanism taking place on very long timescales. The key prediction of this merging scenario is that stellar halos should host a large number of stellar streams and small satellites in the process to be accreted and covering a large range in Galactocentric distances (A. Helmi et al. 1999; F. A. Gómez et al. 2013). Although, the CDM cosmology is nowadays considered the "concordance model," the current empirical scenario for hierarchical galaxy formation is far from being settled. To investigate the hierarchical merging mechanism(s), their timescale, and the mass assembly history of galaxies, one can analyze the metallicity distribution and kinematics of field stars. Below, we outline some of the most recent findings in this area, along with their respective strengths and limitations.

Chemical–orbital properties. The current investigations are mainly based on spectroscopy of bright field red giant (RG) stars (D. Carollo et al. 2007, 2010; S. Liu et al. 2018), but their individual distances can hardly be more accurate than 10–20% (R. Schönrich et al. 2011). D. Carollo et al. (2007) identified two halo components: a more spherical and prograde "inner halo" that is "metal rich" ([Fe/H] ∼ −1.6) and with highly eccentric orbits, and an "outer halo" that is retrograde and more metal poor ([Fe/H] ∼ −2.2). Note that their targets are mainly located in the solar neighborhood (heliocentric distance $d \leqslant 4$ kpc), therefore they were able to investigate a large halo volume only by taking into account the maximum vertical extent of their orbits. This is the reason why the transition between inner and outer halo ranges from 15 to 35 kpc (Y. K. Kim et al. 2019; S. E. Dietz et al. 2020). C. Conroy et al. (2019a) found, using high-resolution (HR) spectra for more than 4200 field RGs, a unimodal iron distribution function (IDF) peaking at −1.2 dex. This estimate is at least 0.3 dex more metal rich than previous estimates based on low-resolution (LR) spectra and a broad range of stellar tracers. Recent investigations based on field RR Lyrae (RRL) and blue (hot) horizontal branch (BHB) stars further support the dual nature of the halo (K. Hattori & Y. Yoshii 2011;

T. D. Kinman et al. 2012). They found that inner and outer halos have different density profiles (flattened versus spherical, I. G. McCarthy et al. 2012), kinematics, and metallicity: the inner halo is more metal rich and with a modest net prograde rotation, while the outer halo has a net retrograde rotation and the peak in the metallicity distribution is 1/3 more metal poor than the inner halo. However, G. Iorio & V. Belokurov (2019) using RRLs from Gaia DR2 detected a transition from a spherical-to-triaxial halo, moving from the inner to the outer regions. Furthermore, P. E. Nissen & W. J. Schuster (2010) investigated the in situ and the ex situ stellar components of the Galactic halo by using accurate elemental abundances and kinematics of nearby dwarf stars.

Chemical tagging. Chemical tagging plays a crucial role in tracing in space and in time the chemical enrichment of the different Galactic components. Among the different Galactic components—halo, bulge, thick disk (TCD), and thin disk (TND)—hosting truly old ($t > 10$ Gyr) stellar populations, the halo plays a crucial role in constraining its early formation. The CDM models predict that pristine dwarf galaxies (clustering around mini dark matter halos) are the main building blocks of large galaxies (E. Tolstoy et al. 2009). This means that the halo hosts the relics of accreted dwarf galaxies, preserved as stellar streams with peculiar kinematics, chemical enrichment histories (V. Belokurov et al. 2006), and distinct pulsation properties (E. Luongo et al. 2024).

Metallicity estimates for field RRL stars are somewhat heterogeneous, relying primarily on the analysis of the light curves (C. Mateu et al. 2012; J. P. Mullen et al. 2021, 2023), pulsation properties (A. Sarajedini 2024, 2025), machine learning algorithms (T. Muraveva et al. 2025), or of metallicity indicators such as hydrogen lines and the Ca II K line (ΔS method, G. W. Preston 1959; N. B. Suntzeff et al. 1991, 1994; A. C. Layden 1994, 1995). More recently, metallicities for field RRLs were derived either from the Sloan Digital Sky Survey/Sloan Extension for Galactic Understanding and Exploration (SDSS/SEGUE, DR8; Y. S. Lee et al. 2008; A. J. Drake et al. 2013) or from the Dark Energy Spectroscopic Instrument (DESI; G. E. Medina et al. 2025a) LR spectra. However, their mean iron abundances were estimated using several spectroscopic indicators and spectra collected at different pulsation phases. Therefore, they are very inhomogeneous and a detailed abundance analysis of MW RRLs is still lacking.

A new spin on the halo IDF has been recently provided by J. Crestani et al. (2021a, 2021b, hereinafter C21a; C21b) and by M. Fabrizio et al. (2021, hereinafter F21) using a homogeneous sample of more than 8000 field RRLs. Their RRL spectroscopic catalog includes both HR (∼220), and SDSS/SEGUE and the Large Sky Area Multi-Object Fiber Spectroscopic Telescope (LAMOST) LR spectra (∼8000). They found that the IDF is unimodal and it peaks at [Fe/H] ∼ −1.55. Although field RRLs are less numerous compared with RG and MS stars, they trace a significant fraction of the MW spheroid ($5 \leqslant R_G \leqslant 100$ kpc) with high accuracy (3%–5% on individual distance, V. F. Braga et al. 2021; J. P. Mullen et al. 2023).

Metallicity gradient. The possible occurrence of a halo metallicity gradient makes the MW assembly scenario more complex. Indeed, A. C. Layden (1995) found, using LR spectra for 302 field RRLs, that the halo iron gradient is quite flat between 10 and 40 kpc with a typical value of [Fe/H] ∼ −1.65. Moreover, he found evidence of a steady increase in metallicity within the solar circle ($R_G \leqslant 8$ kpc). More recently, X.-X. Xue et al. (2015) selected ∼1800 K giant stars with [Fe/H] $\leqslant -1.2$ (SDSS/SEGUE) and found evidence of a shallow metallicity gradient showing a decrease in the mean metallicity of 0.1–0.2 dex when moving from $R_G \sim 10$ to 100 kpc. On the other hand, C. Conroy et al. (2019a) based on HR optical spectra (H3 survey; C. Conroy et al. 2019b) of ∼4200 giants, and E. Fernández-Alvar et al. (2017) based on HR near-infrared (NIR) spectra of ∼3900 RGs (Apache Point Observatory Galactic Evolution Experiment; APOGEE), found no evidence of a gradient over a wide range of Galactocentric distances (10–80 kpc).

The main aim of this investigation is to address the chemo-dynamical properties of field RRLs collected by our group (B.-Q. For et al. 2011; M. Chadid et al. 2017; C. Sneden et al. 2017; C21a; C21b; F21; C. K. Gilligan et al. 2021, hereinafter G21; V. D'Orazi et al. 2024, hereinafter D24; V. D'Orazi et al. 2025a, hereinafter D25) for which we do have spectroscopic estimates of chemical abundance(s) and/or radial velocity (RV). The current sample was complemented with data already available in the literature for BHB stars based on both LR and HR spectra. We also take advantage of the astrometric properties (proper motion, position) provided by Gaia DR3 to perform a solid selection of RRLs belonging to the different Galactic components and to the most populous stellar streams. Moreover, we also perform a detailed analysis of the metallicity distribution functions to constrain their early formation and evolution.

In more detail, the structure of this paper is as follows. In Section 2, we introduce the different photometric datasets adopted in the Photometric Rome RRL catalog (PR3C), and discuss in more detail the spectroscopic datasets based on LR, medium-resolution (MR), and HR spectra we collected for the Spectroscopic Rome RRL Catalog (SR3C, see Appendix D). In this section, the RV and abundance measurements are also outlined. The criteria adopted to perform the kinematic selection of the RRLs belonging to the main Galactic components and to the most populous stellar streams are discussed in Section 3, together with their metallicity distributions. The comparison with the metallicity distributions available in the literature for field stars, globular clusters (GCs), and dwarf galaxies are presented in Section 4. The radial metallicity gradients for the main Galactic components and the major stellar streams, together with linear and logarithmic fits and the comparison with similar Galactic estimates are introduced and discussed in Section 5. Section 6 is focused on the comparison between MW radial gradients based on RRLs with similar estimates available in the literature, while in Section 7 we discuss the comparison between MW and M31 radial gradients for the global halo, the dry halo, and the major stellar streams. A summary of the results is included in Section 8, where we also briefly outline the near future developments of the current project.

2. Photometric and Spectroscopic Datasets

To provide firm constraints on the metallicity distribution across the Galactic spheroid we used different photometric and spectroscopic catalogs based either on proprietary data or available in the literature. Note that the key advantage of the current approach is that we use homogeneous estimates for individual distances and reddening together with a

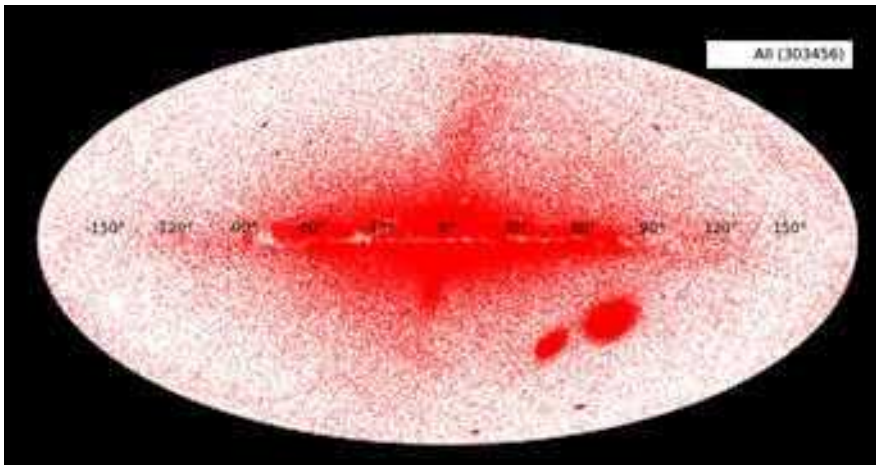

Figure 1. Aitoff projection in Galactic coordinates of the RRLs in the PR3C. Isolated overdensities are associated either with the Magellanic Clouds, or to nearby stellar systems or to stellar streams.

homogeneous metallicity scale for both LR (iron) and HR (iron, α elements) spectra.

2.1. Photometric Datasets

Long–term photometric surveys provided a wealth of new information concerning the identification and the characterization of variable stars in the Galaxy and in nearby dwarf galaxies.

In the last 10 yr, we have assembled a large photometric catalog of field, cluster, and dwarf galaxy RRLs (G. Fiorentino et al. 2015a, 2015b; V. F. Braga et al. 2016, 2021; M. Fabrizio et al. 2019, 2021), called the PR3C catalog. It includes more than 300,000 sources. The astrometric reference frame and the foundation of PR3C are based on Gaia DR3 (Gaia Collaboration et al. 2023b) and its comprehensive RRL catalog (G. Clementini et al. 2023), but it includes RRLs from almost all the known photometric surveys. They can be listed according to the wavelength range (see list below). Note that PR3C will be made available to the community in a forthcoming investigation (V. F. Braga et al. 2025, in preparation) together with a more detailed discussion concerning the cross-match procedure adopted to build-up the catalog (M. Fabrizio et al. 2019).

Optical. The main optical catalogs we took into account are: Catalina Sky Survey (CSS; A. J. Drake et al. 2009, 2017), All Sky Automated Survey (ASAS; G. Pojmański 1997, 2002, 2014), ASAS for SuperNovae (ASAS-SN; T. Jayasinghe et al. 2019) and the General Catalogue of Variable Stars (N. N. Samus' et al. 2017). In this context, large extragalactic surveys have also played a crucial role, since they released detailed catalogs of nearby variable stars as ancillary results, i.e., SDSS (Ž. Ivezić et al. 2000) and the Panoramic Survey Telescope and Rapid Response System (M. Abbas et al. 2014) survey. The same outcome applies to field variables provided by large photometric surveys interested in the identification either of nearby moving objects—Lincoln Near-Earth Asteroid Research (LINEAR; G. H. Stokes et al. 2000; B. Sesar et al. 2011b) and Lowell Observatory Near-Earth-Object Search (A. Miceli et al. 2008)—or in transient sources—Robotic Optical Transient Search Experiment-I (C. Akerlof et al. 2000; K. Kinemuchi et al. 2006), LINEAR+CSS+PTF (B. Sesar et al. 2013), and Zwicky Transient Facility (E. C. Bellm et al. 2019b, 2019a)—, or in the identification of stellar streams in the Galactic halo—La Silla QUEST RRL Star Survey (A. K. Vivas et al. 2006; R. Zinn et al. 2014). Moreover, we also took into account RRLs from the Optical Gravitational Lensing Experiment IV for the bulge, the TND (I. Soszyński et al. 2019b) and for the Magellanic Clouds (I. Soszyński et al. 2019a). As a whole, the apparent optical magnitude ranges from $G \sim 7.62$ to $G \sim 21.19$ mag. The reader interested in more details is referred to M. Fabrizio et al. (2019), V. F. Braga et al. (2021), and to F21.

Near-infrared. Similar datasets have also been collected in the NIR bands by the Two Micron All Sky Survey (2MASS; M. F. Skrutskie et al. 2006; A. C. Layden et al. 2019), the NIR surveys of the Galactic plane (UKIRT Deep Sky Survey, S. J. Warren et al. 2007; P. W. Lucas et al. 2008; UKIRT Hemisphere Survey, S. Dye et al. 2018), and the VISTA Hemisphere Survey (R. G. McMahon et al. 2013, 2021). The apparent NIR magnitudes of the current dataset range from $K \sim 4.35$ to $K \sim 19.31$ mag.

Mid-Infrared. We also collected datasets in the mid-infrared (MIR) from Wide-field Infrared Survey Explorer (WISE; E. L. Wright et al. 2010), NEOWISE (A. Mainzer et al. 2011), AllWISE (R. M. Cutri et al. 2013), and SPITZER (M. W. Werner et al. 2004). The apparent MIR magnitudes of the current dataset range from $W1 \sim 5.94$ to $W1 \sim 19$ mag.

Ultraviolet. Finally, we also took into account datasets in the UV bands from the Galaxy Evolution Explorer (B. Y. Welsh et al. 2005; T. D. Kinman & W. R. Brown 2014). The apparent NUV magnitudes of the current dataset range from NUV ~ 12.5 to NUV ~ 23.2 mag.

All in all, the PR3C catalog includes more than 302,000 field and cluster RRLs. Figure 1 shows the distribution in Galactic coordinates of the entire photometric catalog. The overdensities are associated either with nearby dwarf galaxies (Magellanic Clouds, dwarf spheroidals), galactic globular clusters (GGCs), or to stellar streams. To characterize the pulsation properties of the PR3C catalog, Figure 2 shows the period distribution for RRLs pulsating in the fundamental (FU, RRab; red) mode, in the first overtone (FO, RRc; blue), and simultaneously in the first two radial modes (mixed mode, RRd; green). Typically, the mode identification is based on the same approach suggested by G. Clementini et al. (2019), but we double checked the location of individual RRLs in the Bailey diagram and some outliers were fixed according to visual inspection of their light curves. Figure 3 displays from top to bottom the magnitude distribution of RRLs in the PR3C

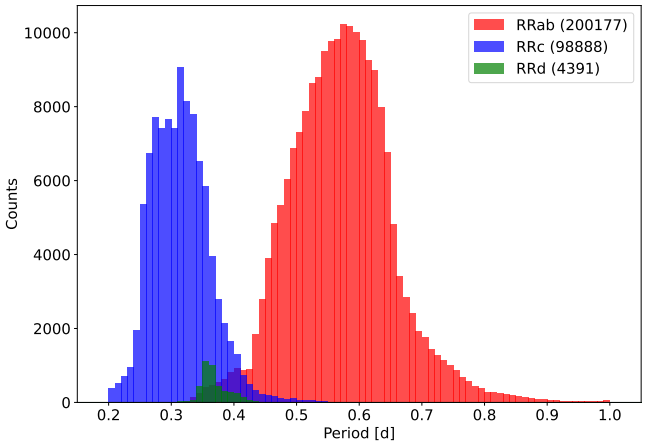

Figure 2. Period distribution of the RRLs in the PR3C. FU (RRab), FO (RRc), and mixed mode (RRd) RRLs are plotted with different colors (see labels).

catalog in the MIR (W_1, top), in the NIR (K_s, middle), and in the optical (R_p, bottom). Although RRLs are, on average, half a magnitude brighter in NIR/MIR bands where they are also significantly less affected by reddening, the optical bands allow us to reach the outskirts of the Galactic halo ($R_G \approx 100$ kpc, $R_P \sim 20$ mag).

2.2. Spectroscopic Datasets

Our group secured a large sample of HR, MR, and LR spectra for field and cluster RRLs. Moreover, RRLs in PR3C were cross-matched with spectroscopic catalogs available in the literature. The subsample of field RRLs for which we do have spectroscopic information is the SR3C catalog.

Figure 4 shows the distribution in Galactic coordinates of the RRL in SR3C for which we do have a spectroscopic measurement of either the iron abundance or the RV. As a whole, we are dealing with more than 16,000 field RRLs for which either LR/MR/HR spectra are available.

To characterize the spectroscopic catalog, Figure 5 shows from top to bottom the Bailey diagram, the period distribution, and the R_P-band magnitude distribution of the RRLs in SR3C. Data plotted in this figure display that RRLs in SR3C cover the typical range in period and in amplitudes for FU (RRab, purple), FO (RRc, red), and mixed mode (RRd, dark green) variables.

This sample was complemented with a sample of field BHB stars for which either LR or HR spectra are also available (see Table 1). Blue HB stars are, together with RRLs, solid tracers of old stellar populations and they can be safely identified in the field, since their colors are typically bluer than F-, G-type, and M-type field stars. In the literature, there are several investigations concerning red HB stars, but the selection criteria (photometry, kinematics) adopted for their identification are not very solid yet. We only adopted a few red HB stars for which a spectroscopic characterization is available (C21b, and references therein).

2.2.1. Individual Radial Velocities

In this investigation we deal with RV measurements coming from a wide range of HR, MR, and LR spectra.

RV curve. The RV measurements based on HR spectra were performed using synthetic spectra with a spectral resolution and wavelength range similar to the observed ones. The reader interested in a more detailed discussion is referred

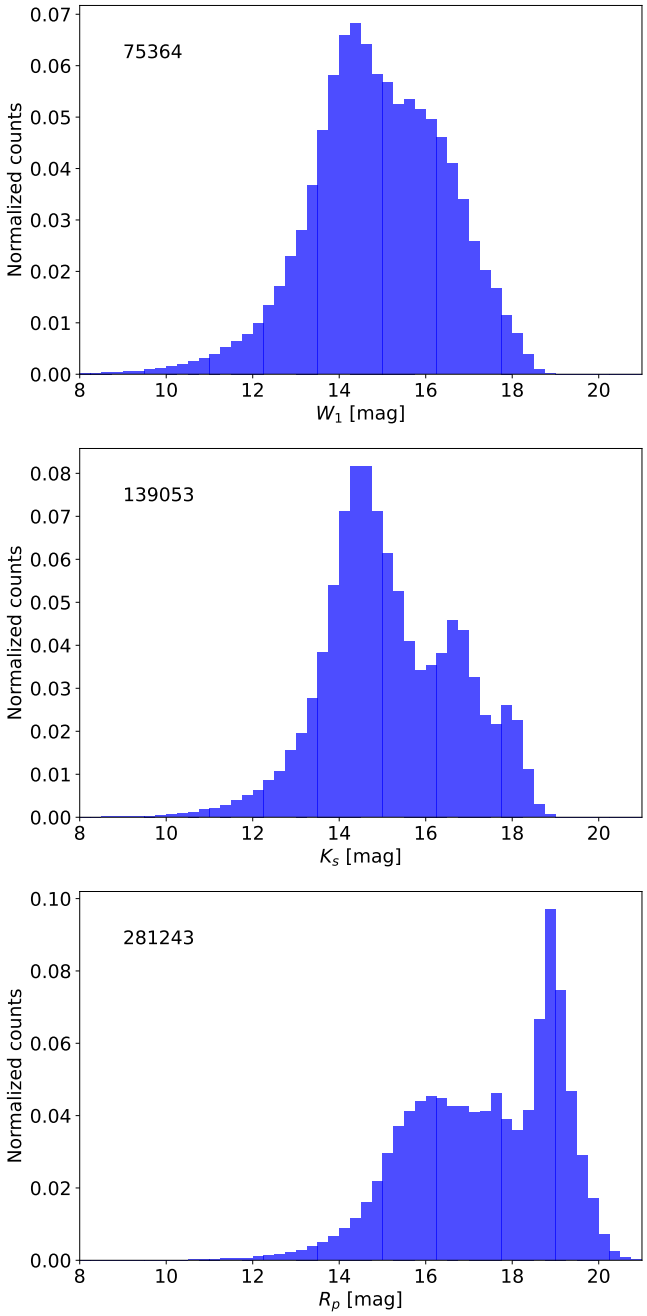

Figure 3. Selected magnitude distributions for RRLs in the PR3C. From top to bottom, the histograms display the MIR $W1$-band, the NIR K-band, and the Gaia optical R_P-band magnitudes.

to C21a, C21b, and F21. A handful of field RRLs have a full coverage of the pulsation cycle (G. Bono et al. 2020) based on HR spectra and their γ velocity was estimated with an analytical fit of the RV curve based on weak metallic lines. The RV error associated with these measurements is the standard deviation of the analytical fit. Note that this sample also includes two relevant literature contributions.

Gaia–Gaia performed accurate estimates of the γ velocity for 1096 RRLs by performing an analytical fit of the RV curves. The reader interested in more details is referred to G. Clementini et al. (2023).

Baade–Wesselink. For roughly three dozen of field Baade–Wesselink RRLs accurate optical-NIR light curves and also

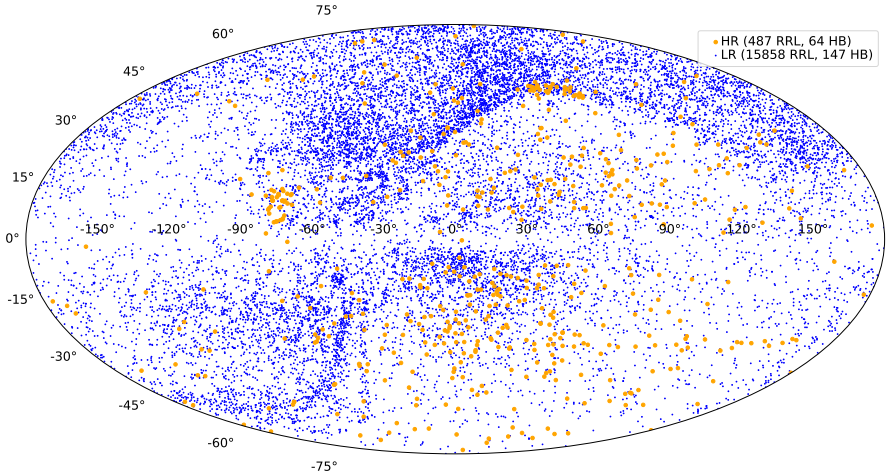

Figure 4. Aitoff projection in Galactic coordinates of the RRLs in the SR3C. Yellow and blue dots mark RRLs and HB stars for which either HR or LR spectra are available, respectively. The number of RRLs and HBs with HR and LR spectra is labeled.

very well-sampled RV curves, based on weak metallic lines (G. Bono et al. 1994; C. Cacciari & G. Clementini 2003, and references therein), are available.

HR spectra. This sample mainly includes the spectra we collected to measure individual elemental abundances. They are mainly a single spectrum per object, with a small fraction with two/three spectra. Thanks to the high spectral resolution, the error on the RV for the RRLs with single spectra is the standard deviation among the different metallic lines. The error on the RV for RRLs with a few HR spectra is the standard deviation of the mean. Note that this sample also includes the BHB stars observed by B.-Q. For & C. Sneden (2010) and by T. D. Kinman et al. (2012, and references therein).

MR spectra. This sample mainly includes 5895 RRLs that have been observed by Gaia, but for which the RV values are the mean of the measurements and their error is the standard deviation of the measurements.

This sample also includes a few (3) RRLs observed by the Radial Velocity Experiment survey (RAVE; M. Steinmetz et al. 2006; A. Kunder et al. 2014, 2017; M. Steinmetz et al. 2020a). They are only based on MR spectra and they are quite limited (see Table 1). They were downloaded from the RAVE survey website.[39] The RVs and the associated errors were measured following the same approach for the HR spectra.

LR spectra. This is the largest sample of RVs and they mainly come from public spectroscopic surveys and the γ velocity is either the mean or the median of the measurements. The following criteria were adopted for defining the priority list:

(a) *Number of measurements*. The highest priority among the LR spectra is given to the datasets for which multiple individual measurements are available. For these objects, the mean RV was estimated as the mean of the individual measurements and the associated error is the standard deviation of the measurements. In case the multiple measurements have been coadded either to a single reference spectrum or measured on coadded intra-night spectra, they have lower priorities.

(b) *Wavelength coverage*. Spectra covering a broader range in wavelength have higher priorities.

(c) *Sample size*. Higher priority is given to datasets including larger samples of field RRLs.

Note that the LR sample also includes a sizable sample of spectra collected with du Pont coming from the RRL Carnegie dataset. They are HR spectra, but their individual signal-to-noise ratio (SNR) is modest and they do not allow us to perform accurate elemental abundances. Therefore, their original spectral resolution was decreased by roughly a factor of 10 and used as LR spectra (C21a; C21b) to estimate both RVs and iron abundances (ΔS method).

A large sample (see Table 1) of HR spectra collected by the Galactic Archaeology with HERMES (GALAH) survey was also used to estimate RVs because their individual SNR is modest/poor. These spectra were not used to estimate the iron abundances with the ΔS method because they do not cover the Ca H&K lines.

Literature. This sample is a mixed bag, since it includes RV measurements available in the literature based on spectra covering a broad range of spectral resolutions and number of measurements.

According to these selection criteria, the priority list is as follows: (a) RV curve fit from our HR spectra, (b) RV curve fit from Gaia measurements, (c) R. Zinn et al. (2020), (d) averaged RVs from DESI, (e) averaged RVs from Gaia, (f) averaged RVs from our HR spectra, (g) averaged RVs from LAMOST MR spectra, (h) averaged RVs from LAMOST LR spectra, (i) averaged RVs from SDSS spectra, (j) S. Duffau et al. (2014), (k) D24, (l) averaged RVs based on Gaia, LAMOST, and SDSS (when less than 2 data points are available from the different datasets), (m) G. E. Medina et al. (2023), (n) RV from stacked GALAH spectra, (o) C. J. Hansen et al. (2011), (p) J. M. Nemec et al. (2013), and (q) averaged H_α, H_β, H_γ RVs from our HR spectra, when metallic lines are not available.

The top panel of Figure 6 shows the RV distribution of both HR (dark yellow) and LR (blue) sample. As expected, the RV distribution of field RRLs is quite symmetric around zero with two well extended tails approaching $\pm 400\,\mathrm{km\,s^{-1}}$. The black solid line shows the smoothed distribution estimated by using a Gaussian kernel with unitary weight and σ equal to the Poisson error of the individual bins. Although the LR sample is more than one order of magnitude larger than the HR sample, the standard deviations of the two RV distributions have quite similar values (see labeled values). This indicates that the RV

[39] https://www.rave-survey.org/

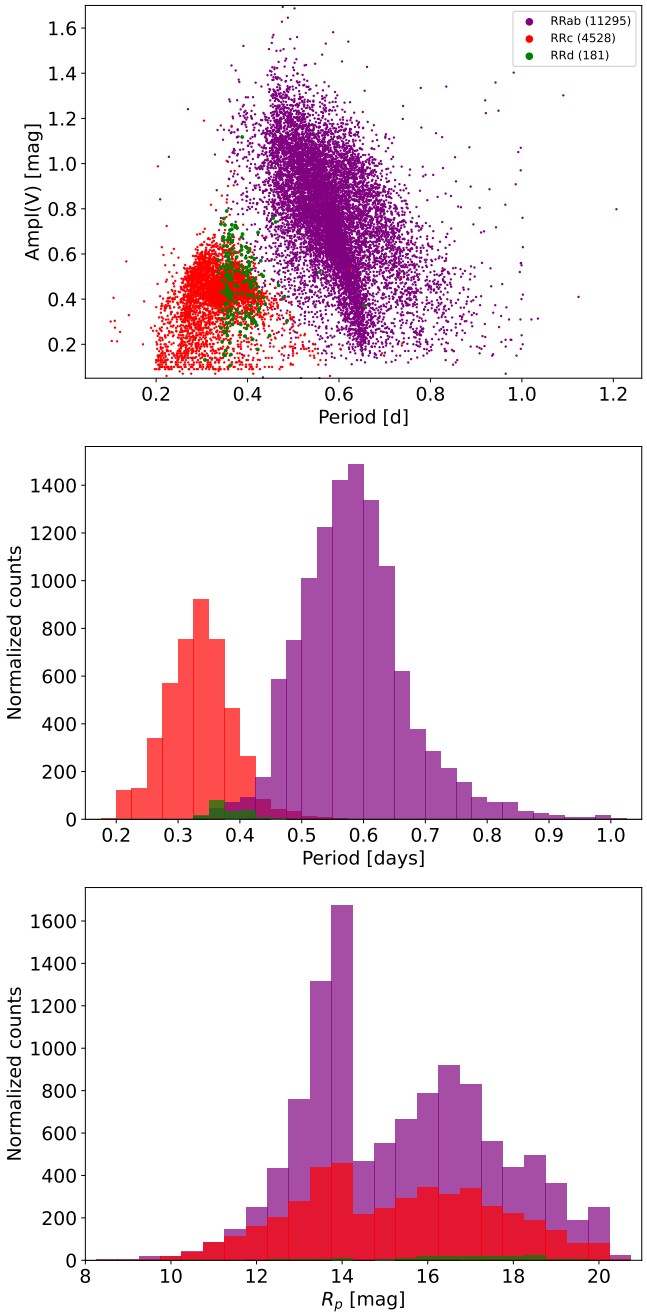

Figure 5. Top: *V*-band luminosity amplitude versus period (Bailey diagram) for RRLs in SR3C. RRLs that are pulsating in the FU mode (RRab) are highlighted in purple, those pulsating in the FO (RRc) in red, and the RRLs that are simultaneously pulsating in the first two radial modes (RRd, mixed mode) in dark green. The numbers close to the acronyms show the sample size. Middle: Same as the top, but for the period distribution. Bottom: same as the top, but for the mean R_P-band magnitude distribution.

distributions are dominated by RRLs located across the solar circle.

2.2.2. Individual Iron Abundances

The selection criteria and the datasets adopted for estimating individual iron abundances are very similar to those adopted for the RVs. The iron abundances of the HR sample were estimated using individual FeI and FeII lines. The reader interested in a more detailed discussion is referred to C21a, C21b, G21, D24 and to D25. The priority list for

Table 1
Spectroscopic Datasets Included in SR3C

Dataset	RV		[Fe/H]		[α/Fe]
	LR	HR	LR	HR	HR
—RRL—					
Crestani	…	576[a]	8117[b]	159+78[c]	201[d]
D24	…	…	…	78	60
D25	…	…	…	3	…
B. Sesar et al. (2013)	…	…	21	…	…
G. C. Liu et al. (2020)	…	…	303	…	…
LAMOST	5436	…	…	…	…
SDSS	1688	…	…	…	…
Gaia	5895	…	…	…	…
GALAH	…	2307	…	119	51
R. Zinn et al. (2020)	104	…	195	…	…
T. D. Kinman et al. (2012)	…	…	51	…	…
A. K. Dambis et al. (2013, 2014)	…	…	9	…	…
RAVE	…	…	3	…	…
S. Duffau et al. (2014)	…	39	…	36	…
C. J. Hansen et al. (2011)	…	2	…	…	…
J. M. Nemec et al. (2013)	…	11	…	…	…
DESI	1227	…	…	…	…
G21	…	…	…	14	…
G. E. Medina et al. (2021)	…	15	…	…	…
—HB—					
B.-Q. For & C. Sneden (2010)	…	45	…	46	39
Kinman[e]	123	18	…	9	7

Notes. Listed from left to right are: the name of each dataset, the number of RRLs and HB stars with available RV measurements from either LR or HR spectra, the number of RRLs and HB stars with iron abundance measurements based on LR (ΔS method) or HR spectroscopy, and the number of RRLs and HB stars with [α/Fe] abundance measurements derived from HR spectra. The numbers listed in this table do refer to the number of objects of each dataset that contributes to SR3C according to the priority list for RVs and chemical abundances discussed in Section 2.2.1 and in Section 2.2.2, respectively.
[a] G. Bono et al. (2020); V. F. Braga et al. (2021); D24.
[b] C21a; F21.
[c] C21a.
[d] C21b.
[e] T. D. Kinman et al. (1994); T. Kinman et al. (2000); T. D. Kinman et al. (2007, 2012).

the metallicity estimates is as follows: (a) D24; D25, (b) C21b, (c) G21, (d) S. Duffau et al. (2014), (e) GALAH DR3, (f) C21a, (g) R. Zinn et al. (2020), (h) G. C. Liu et al. (2020), (i) A. K. Dambis et al. (2013), (j) B. Sesar et al. (2013), (k) RAVE DR6, (l) T. D. Kinman et al. (2012).

In passing we note that the metallicity scale adopted in the quoted investigations is the same adopted by D. Magurno et al. (2018, 2019) in dealing with cluster RRL variables. The reader interested in a more detailed discussion concerning field and cluster RRLs is referred to the quoted papers.

The bulk of the current iron abundances is based on a new version of the ΔS method provided by C21a; C21b and originally suggested by G. W. Preston (1959). This spectroscopic diagnostic was applied to all the LR spectra we collected for the RV measurements. The individual spectra with a SNR smaller than 15 were neglected. This is the reason why the number of RRLs with iron abundances is smaller than the RRLs with RV measurements. The error associated with the iron abundances of RRLs with multiple spectra is the

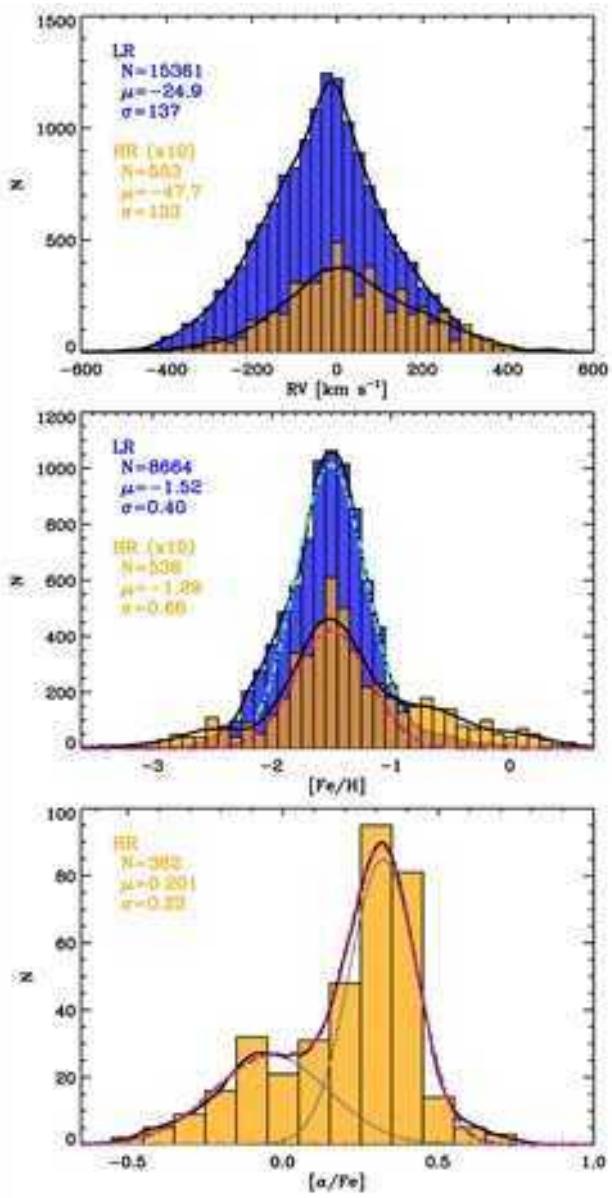

Figure 6. Top: mean RVs for spectroscopic RRLs based either on LR (blue) or on HR (orange) spectra. The RV distribution of the latter sample was amplified by a factor of 10 to improve the visibility. The black solid lines display the smoothed distributions based on a Gaussian kernel. The number of RRLs in the two different samples are labeled together with the mean and the standard deviation of the two different samples. Middle: Same as the top, but for the iron distribution based either on LR or on HR spectra. The black solid lines display the smoothed distributions, while the dashed–dotted lines show the fit with a Gaussian function. Bottom: same as the top, but for the [α/Fe] distribution only based on HR spectra. The black solid lines show the smoothed distribution, the dashed–dotted line the fit with two Gaussian functions, and the thin gray lines the individual Gaussian functions.

standard deviation. The error associated with RRLs for which we do have a single spectrum was estimated as the mean error of the spectroscopic dataset. The reader interested in a more detailed discussion is referred to F21.

Note that SR3C includes 181 mixed-mode variables (RRd) and they were treated as FO variables because the dominant mode is typically the FO (F21). The application of the ΔS method to a field mixed-mode variable (ASAS J183952-3200.9) for which we collected a dozen of HR spectra along the pulsation cycle (C21a, see their Section 7.2) supports this assumption.

The spectroscopic iron abundances available in the literature were estimated using a broad variety of ΔS methods or similar diagnostics based either on LR or on MR spectra. The different sets of iron abundances were included in the current catalog only if we had a sizable sample of objects in common, which we defined as local calibrators. We performed a linear analytical fit of the difference in iron abundance between our estimates and those available in the literature, and these relations were used to move the iron abundances of the entire sample into our metallicity scale (see Table 1 in F21).

The current spectroscopic dataset, compared to F21, includes the following new datasets: T. D. Kinman et al. (2012), G21, G. E. Medina et al. (2023), GALAH DR3 (S. Buder et al. 2021), D24, and D25. Note that we could not rescale the G. E. Medina et al. (2023) sample because we found no match with any of our RRLs. Also, G21, D24, and D25 are already in our metallicity scale. The linear analytical relations used to convert the metallicities of T. D. Kinman et al. (2012) and GALAH DR3 into our metallicity scale are the following linear relations (1) and (2):

$$[\mathrm{Fe/H}]_{\mathrm{our}} = -0.497 \pm 0.047 + 0.770 \pm 0.049 \cdot [\mathrm{Fe/H}]_{\mathrm{GALAH}}\ (0.172) \quad (1)$$

$$[\mathrm{Fe/H}]_{\mathrm{our}} = -0.37 \pm 0.22 + 0.75 \pm 0.14 \cdot [\mathrm{Fe/H}]_{K12}\ (0.30) \quad (2)$$

where the symbols have their usual meaning and the numbers in parentheses are the standard deviations. As a whole, the HR sample compared with F21 was increased by more than a factor of two (550 versus 246), while the LR sample was minimally changed (8800 versus 8769).

Note that in the current analysis we are not taking account the iron estimates of field RRL stars based either on Fourier parameters of optical (J. M. Nemec et al. 2011; A. Garofalo et al. 2013; P. Pietrukowicz et al. 2015; G. Torrealba et al. 2015; I. Dékány et al. 2018) and NIR/MIR (J. P. Mullen et al. 2021, 2023; M. Zoccali et al. 2024) light curves, on the inversion of the PLZ relations (C. E. Martínez-Vázquez et al. 2016; V. F. Braga et al. 2016), on the K_{15} parameter based on luminosity amplitudes (G. Bono et al. 2007), or on the `REDIME` algorithm based on optical and NIR mean magnitudes (G. Bono et al. 2019). They will be addressed in a forthcoming paper.

The middle panel of Figure 6 displays the IDF based either on LR (blue) or on HR spectra (dark yellow). The black solid lines show the smoothed distributions estimated by using a Gaussian kernel. We associated with each RRL in the current sample a Gaussian function with unitary weight and σ equal to the error of the individual estimates. The black lines are the cumulative distribution of the individual Gaussian functions. The two IDFs agree within the errors; we fit the two smoothed distributions with a Gaussian function and we found that the peak and the σ are: -1.51 ± 0.01, $\sigma = 0.30 \pm 0.01$ (LR) and -1.50 ± 0.03, $\sigma = 0.31 \pm 0.04$ (HR), respectively. The two IDFs display a symmetrical distribution marginally skewed in the metal-poor regime and a well-defined peak. The difference in the metal-rich and in the metal-poor tails between the two distributions is mainly due to the difference in sample size. In passing, we note that the current findings fully support earlier results based on smaller spectroscopic samples from C21a, C21b, and F21.

2.2.3. Individual α-element Abundances

The bottom panel of Figure 6 shows the [α/Fe] abundance ratio for field RRL and BHB stars based on HR spectra. The mean α-element abundance includes three different elements (Ca, Mg, and Ti), since these are the three elements measured by C21b. The black line shows the smoothed distribution computed using a Gaussian kernel, the histogram shows quite clearly that the [α/Fe] distribution is bimodal. We fit the distribution with two Gaussian functions and we found that the main peak is located at [α/Fe] $\sim 0.32 \pm 0.01$, $\sigma = 0.11 \pm 0.01$; while the secondary peak is located at [α/Fe] $\sim -0.04 \pm 0.01$, $\sigma = 0.19 \pm 0.01$. According to previous results obtained by B.-Q. For et al. (2011), M. Chadid et al. (2017), C. Sneden et al. (2017), C21a, C21b, D24, and D25, we can safely associate the main peak with metal-poor RRLs, showing a well-defined α-enhancement, while the secondary peak is mainly associated with metal-rich RRLs that are either α poor or even α depleted.

3. Kinematic Selection

The RRL kinematics, and in particular their orbital integration, was investigated by using the MWPotential2014 (J. Bovy 2015) implemented in the code `galpy`. Moreover, we adopted a solar distance from the Galaxy center of 8.122 kpc (GRAVITY Collaboration et al. 2018), a height of the Sun above the Galactic plane of $z_{\odot} = 20.8$ pc (M. Bennett & J. Bovy 2019), the solar peculiar motion by R. Schönrich et al. (2011), and the orbital velocity at the solar distance suggested by R. Drimmel & E. Poggio (2018) that is $(U_{\odot}, V_{\odot}, W_{\odot}) = (12.9, 245.6, 7.78)$ km s^{-1}. Among the input parameters adopted to estimate individual orbits, Galactocentric distances and RVs have been discussed in Appendix A and in Section 2.2.1, while the sky coordinates and the proper motions come from Gaia DR3.

Special attention was paid to estimate the uncertainties associated with the orbital parameters. To constrain on a quantitative basis the errors associated with the orbital properties, we performed a bootstrap analysis in which the initial conditions for the six input parameters (position, proper motion, RV, distance) were extracted one thousand times, with a Monte Carlo, by using Gaussian distributions with means equal to the adopted values and σ equal to their intrinsic errors. Moreover, to properly trace possible orbital variations on individual RRL, we integrated the initial conditions forward for 10 Gyr with steps of 1 Myr. Note that these simulations were performed by taking into account the correlation between the components of the proper motion. Moreover, and even more importantly, the kinematic properties of the individual RRLs were estimated as the median of the 1000 realizations and their associated errors are the 16th and the 84th percentile of their distributions.

We found that the error budget in the kinematic properties of the current RRL sample is dominated by uncertainties in proper motion. This evidence was somehow expected, since our sample covers a wide range in Galactocentric distances. To overcome thorny problems in the analysis of the kinematic properties, we decide to be conservative and to include in the "solid sample" the RRLs up to 98th percentile in the proper motion errors distribution. This means a cut at $\epsilon PM_{RA} = 0.57$ mas yr^{-1} and $\epsilon PM_{DEC} = 0.50$ mas yr^{-1}. The "solid sample" includes 15,550 RRLs and the subsequent chemo-dynamical analysis is only based on these objects.

3.1. Identification of the Main Galactic Components

To provide a robust selection of the main Galactic components, halo, TND, and TCD, we adopted the same selection criteria, based on relative probability ratios, suggested by T. Bensby et al. (2014). It is worth noticing that stars that share a common origin according to the adopted selection criteria will be discussed in Section 3.2.

The left panels of Figure 7 display from top to bottom the RRLs belonging to the halo, the TCD, the TND, and in retrograde orbits. The symbols are color coded according to the iron abundance and they show quite clearly the systematic drift from the more metal-poor RRLs of the halo to the more metal-rich component of the TND. The RRLs associated with the TCD trace quite well the transition between the more metal-poor and the more metal-rich regime. There is solid evidence that the TCD sample includes a sizable sample of RRLs with solar iron abundance.

In our previous investigation (D24), we adopted the circularity of the orbits, defined as the angular momentum J_z along the vertical z-axis normalized by the angular momentum of a circular orbit with the same binding energy E ($\lambda_z = J_z/J_{\max}(E)$), as a function of the Galactocentric distance to identify the different Galactic components. Following L. Zhu et al. (2018) and G. Santucci et al. (2023), the stellar orbits were divided into four different stellar components: a cold component with near circular orbits and strong rotation, a warm component with weak rotation, a hot component with radial orbits and random motions, and a counter-rotating component with a strong-to-weak rotation in between the warm and the cold component.

To validate the current selection criteria, the right panels of Figure 7 show from top to bottom the same RRLs, but in the circularity of the orbits versus the Galactocentric distance (λ_z versus R_G). Data plotted in this plane display that there is a fair agreement between the two different approaches. Indeed, more than 73% of halo RRLs have hot orbits ($-0.25 < \lambda_z \leqslant 0.25$), and R_G ranging from a few kpc to almost 100 kpc; 59% of TCD RRLs have warm orbits ($0.25 \leqslant \lambda_z \leqslant 0.8$), and R_G on average smaller than 40 kpc; and 92% of TND RRLs have cold orbits ($0.80 \leqslant \lambda_z$) and R_G at most of 10/20 kpc. According to this selection criteria, RRLs in retrograde orbits have a circularity smaller than $\lambda_z \leqslant -0.25$. Data plotted in the bottom panels of Figure 7 show that RRL in retrograde orbits are roughly 7% of the entire sample; moreover, they attain R_G distances very similar to halo RRLs and similar metal-poor iron abundances.

To investigate on a more quantitative basis the metallicity distribution functions, the left panels of Figure 8 display from top to bottom the IDFs of the different Galactic components. It should be noted that the peak of the IDF steadily shifts toward more metal-rich chemical compositions when moving from the halo to the TND. Moreover, the IDF becomes broader and broader; indeed, the standard deviation of the distributions increases by 50% when moving from the halo to the TND (0.37 versus 0.57). It is worth mentioning that TCD RRLs also show a broad IDF with a well-defined metal-rich tail, while the IDF of RRLs in retrograde orbits is very similar to the halo IDF.

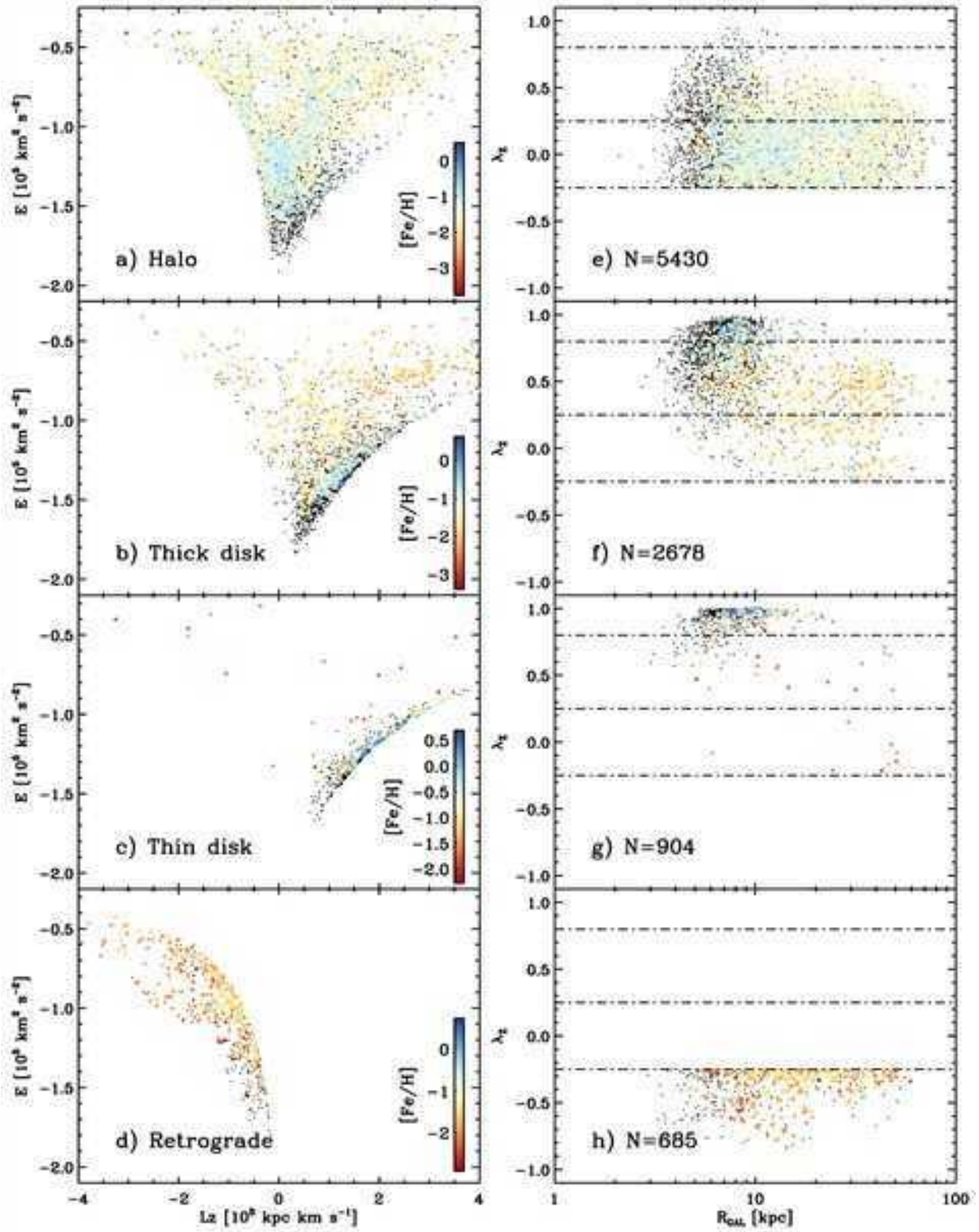

Figure 7. Left: panels (a), (b), and (c) show the Lindblad diagram for the three Galactic components (halo, TCD, and TND) selected according to the probabilistic criteria suggested by T. Bensby et al. (2014). Panel (d) shows the RRLs in retrograde orbits. The symbols are color coded according to the iron abundance (see color bar in the inset). Right: same as the left, but the circularity of the orbits (λ_Z) as a function of the Galactocentric distance. The number of RRLs in the different Galactic components are labeled. See text for more details.

The α-element distributions plotted in the right panels of Figure 8 are only based on HR spectra and they fully support the variations in the IDFs. Indeed, halo RRLs are α enhanced since their mean α-element abundance ratio is $[\alpha/\mathrm{Fe}] = 0.27$ ($\sigma = 0.18$), and they only include a few outliers that are α poor. The TCD RRLs include RRLs that are either α enhanced for $[\mathrm{Fe/H}] \leqslant -1.0$ or α poor/α depleted in the more iron-rich regime. The reader interested in a more quantitative discussion

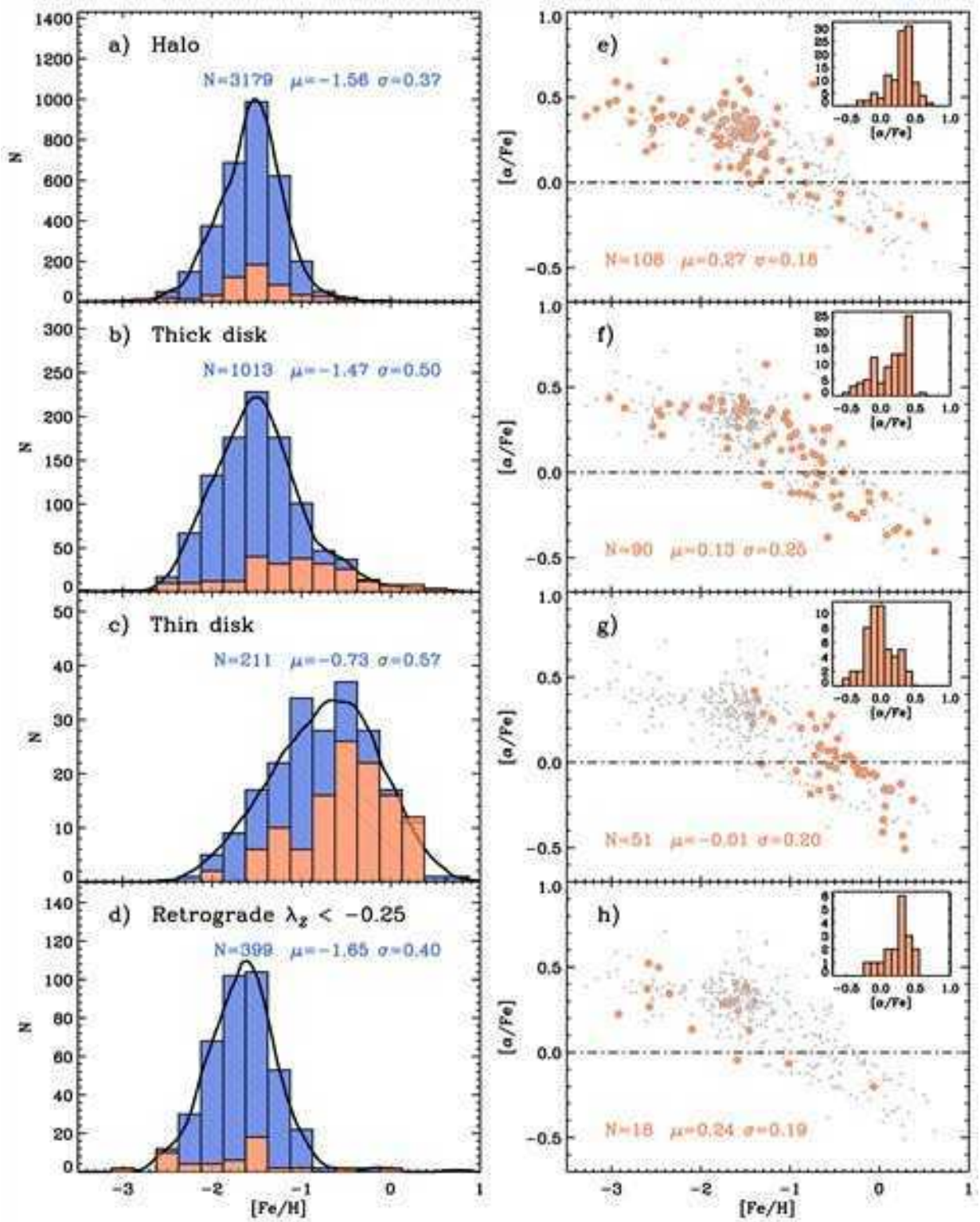

Figure 8. Left: IDF, based on LR (blue) and on HR (orange) spectra, for the four Galactic components (see labeled values) identified in Figure 7. The black lines show the running average over the entire subsample. The number of RRLs, and the mean and standard deviations are also labeled. Right: same as the left, but for individual [α/Fe] abundance ratios as a function of the iron abundance. The gray dots display the entire sample, while the orange circles individual abundances in the four Galactic components. The inset shows the [α/Fe] distribution function. The mean and the standard deviations are also labeled.

concerning the impact that radial migrations have on the decrease in the [α/Fe] abundance ratio of the TCD is referred to M. Aumer & J. Binney (2017) and M. Aumer et al. (2017). Interestingly enough, TND RRLs are mainly α poor/α depleted, and, indeed, their mean α-element abundance ratio is [α/Fe] = 0 ($\sigma = 0.20$). However, there is a small group ($\sim$10 out of 50) that are either moderately α enhanced ([Fe/H] = ~-1) or α enhanced ([Fe/H] ~ -1.5). The sample

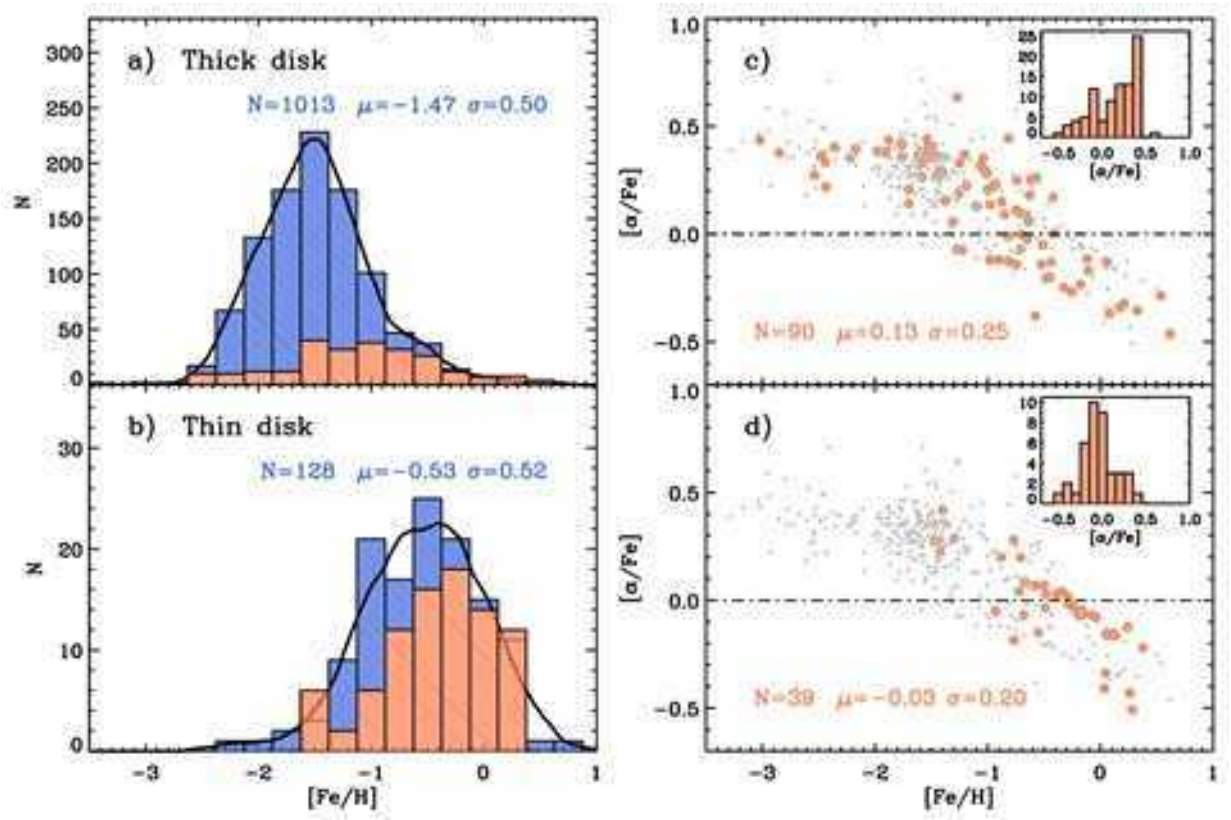

Figure 9. Left: IDF for TND and TCD RRLs (see labeled values) identified following the criteria provided by T. Bensby et al. (2014) joined with the criteria suggested by E. Fernández-Alvar et al. (2024) [$J_\phi/J_{\rm tot} > 0.95$, $|(J_Z - J_R)/J_{\rm tot}| < 0.05$, and $|Z_{\rm MAX}| < 1.5$ kpc]. The black lines show the running average over the entire subsample. The number of RRLs, the mean, and the standard deviations are also labeled. Right: Same as the left, but for the [α/Fe] distribution function.

of α measurements for RRLs in retrograde orbits is limited (18), but they show, within the errors, an α-element distribution similar to halo RRLs.

To provide a more stringent selection for TND RRLs, we decided to use the selection criteria recently suggested by E. Fernández-Alvar et al. (2024). They adopted two different selections for TND stars. They should be located in the right cusp of the action diamond (i.e., those with circular orbits on the Galactic plane) with $L_z/L_{\rm tot} > 0.95$ and $|(J_z - J_r)/J_{\rm tot}| < 0.05$. Moreover, they only selected stars with small distances from the Galactic plane $|Z_{\rm max}| < 1.5$ kpc. The bottom left panel of Figure 9 displays TND stars once we applied the quoted selection criteria. The number of RRLs with TND kinematics decreased, as expected, from 211 to 128, while the mean iron abundance moves from [Fe/H] = −0.73 to [Fe/H] = −0.53, but the standard deviations are quite similar (0.57 versus 0.52). Concerning the α-element distribution (bottom right panel), the number of RRLs that are either moderately α enhanced ([Fe/H] = ∼−1) or α enhanced ([Fe/H] ∼ −1.5) decreased, but the relative fraction is roughly the same (7 out of 39). It is clear that TND stars, that are either moderately or α enhanced, are peculiar from the chemical point of view. They might be a limitation of the adopted kinematic selection criteria. It goes without saying that they are in a high-priority watch list and they are going to be further investigated for a more detailed analysis of their elemental abundances. The impact of the new selection on the metallicity distribution functions of TCD stars is, within the errors, negligible (see top panels of Figure 9).

The main result of the current analysis concerning the chemical enrichment of the different Galactic components is a steady variation from the iron-poor regime of the halo to the metal-rich regime of the TND. This continuous variation is further supported by the variation in the α-element abundance ratio; indeed, it moves from α enhanced in the halo to α poor in the TND, with the TCD hosting both α-enhanced and α-poor/α-depleted RRLs.

In this context, it is worth discussing the variation in the metallicity distribution function when moving from halo to TND RRLs. The occurrence of a metal-rich tail in the metallicity distribution function of field RRLs dates back to W. Baade (1958) in his seminal paper on bulge/disk RRLs. The very first solid spectroscopic identification of metal-rich RRLs was provided by G. W. Preston (1959, 1961), and later supported by D. Butler et al. (1976) and by A. Saha & J. B. Oke (1984) using metallicity estimates based on the ΔS method and by J. Lub (1977) on the basis of the Walraven photometry. Subsequent spectroscopic investigations for bulge (A. R. Walker & D. M. Terndrup 1991) and field (A. C. Layden 1994, 1995) RRLs fully supported this preliminary evidence. Measurements of RRLs with either solar or supersolar iron abundance were provided by M. Chadid et al. (2017), C. Sneden et al. (2017), and D. Magurno et al. (2018, 2019), more recently by C21a and C21b, and by D24. These investigations and the current findings indicate that the enhancement in α-element abundances steadily decreases when moving from metal-intermediate to metal-rich RRLs. In passing, we also note that the decrease in α-enhancement does not imply a steady decrease in age. This circumstantial evidence is supported not only by Galactic

chemical evolution models (A. Micali et al. 2013; E. Spitoni et al. 2019, see their Figure 8) but also on the detailed chemo-dynamical analysis of TND and TCD stars recently provided by L. Borbolato et al. (2025).

The literature concerning the evolutionary channel producing metal-rich RRLs is wide and dates back to R. E. Taam et al. (1976). On the basis of pioneering evolutionary calculations of horizontal branch models at solar iron abundance and plain physical arguments concerning the efficiency of the mass loss along the red giant branch (RGB), they found that the probability to form metal-rich RRLs is significantly lower when compared with typical metal-poor and metal-intermediate RRLs. Subsequent evolutionary and pulsation prescriptions based on a wide range of chemical compositions ranging from the very metal-poor to supersolar iron abundances (G. Bono et al. 1997b, 1997c, 1997a) suggested that metal-rich RRLs can be formed according to canonical assumptions concerning old progenitors and the efficiency of mass loss along the RGB. To take account for the recent discovery of a large fraction of metal-rich RRLs it was also suggested that they are significantly younger than canonical RRLs and they are the aftermath of binary evolution (A. Bobrick et al. 2024). Spectroscopic investigations based on HR spectra suggest that three metal-poor/metal-intermediate RRLs out of ≈480 that have been investigated so far display evidence of an enrichment in neutron capture elements (V. D'Orazi et al. 2025b). This evidence indicates that they evolved in an interacting binary system and the fraction is similar to nonvariable stars. However, the identification of binary RRLs via RV variations is quite difficult due to their intrinsic RV displacements. The approach suggested by P. Kervella et al. (2019a, 2019b) appears very solid and very promising, since it is based on the signature of the presence of a companion on the RRL proper motion. In their seminal investigations they identified seven spatially resolved, probably bound, systems out of the 789 RRLs that have been investigated. This fraction should be considered as an upper limit, since only a minor fraction is in interacting binaries. The role played by the iron content in metal-rich RRLs deserves more detailed spectroscopic investigations.

To properly identify RRLs with common origin, we adopted the same dynamical planes suggested by J. M. M. Lane et al. (2022). The first two diagrams are based on velocity information; in particular, panel (a) of Figure 10 shows the Toomre diagram: the RRL transversal velocity as a function of the perpendicular velocity, i.e., the sum in quadrature of radial and vertical velocity components ($\sqrt{V_R^2 + V_Z^2}$) in Galactocentric cylindrical coordinates; panel (b) shows the RRL in the V_R versus V_T plane. Three panels are based on the vertical component of the angular momentum (L_Z), namely panel (c) shows the Lindblad diagram, i.e., the RRL orbital energy—E—versus L_Z, panel (d) the RRL eccentricity versus L_Z, and panel (e) the square root of the radial action ($\sqrt{J_R}$) versus $J_\phi = L_Z$. Moreover, panel (f) shows the "action diamond," i.e., $(J_Z - J_R)/J_{\rm tot}$ versus $J_\phi/J_{\rm tot}$, where $J_{tot} = |J_\phi| + J_R + J_Z$. Together with these classical kinematic planes, we also took advantage of three additional planes based on the circularity of the orbits. Panel (g) shows the RRL circularity—λ_Z—as a function of the eccentricity, panel (h) shows the circularity—λ_Z—as a function of $Z_{\rm max}$, and panel (i) displays the circularity—λ_Z—as a function of the Galactocentric distance. We added these three planes because RRL cover a very broad range in Galactocentric distances; indeed, they have been identified from the very center of the Galaxy (D. Minniti et al. 2016) to the outskirts of the Galactic halo (B. Sesar et al. 2012; G. E. Medina et al. 2025a). Moreover, they are ubiquitous across the Galactic spheroid and the three adopted parameters significantly change when moving from TND and TCD to halo RRLs.

To validate the criteria adopted to select RRLs in the main Galactic components, they have been plotted in the above kinematic planes. In particular, the shaded gray area shows the distribution of halo RRLs and RRLs with retrograde orbits. TND and TCD RRLs are marked with orange and green dots. Candidate TND and TCD RRLs can be easily identified in the Toomre diagram (panel (a)), since due to their relatively cold vertical velocity they cluster in the bottom right corner with $V_T \simeq 250\,{\rm km\,s^{-1}}$ and $V_T \simeq 150\,{\rm km\,s^{-1}}$, respectively. The same outcome applies for the candidate halo RRLs and to RRLs in retrograde orbits, since they cover a very wide range in perpendicular velocities and they also show either vanishing or negative transversal velocities. The separation between TND/TCD and halo RRLs is also quite clear in the V_R versus V_T plane, since the three different components display a well-defined ranking in V_T and a steady increase in RV.

In this context it is worth addressing on a more quantitative basis the RRLs with hot orbits. Indeed, according to the adopted selection criteria, RRLs with hot orbits might belong either to the halo or to the bulge. To quantify the fraction of RRLs that are confined to the bulge, we identified the RRLs that along their orbits have an apocentric radius smaller than $r_{\rm apo} \leqslant 3.5$ kpc. Note that this search was performed on the one thousand realizations we computed to investigate their kinematic properties. We found that only five RRLs in our sample are candidate bulge RRLs, since their apocentric radius in the median value of one thousand orbits is smaller than 3.5 kpc. They are plotted as magenta diamonds in the dynamical planes of Figure 10. In particular, they can be easily identified in the Lindblad diagram (panel (c)), since they are characterized by very low orbital energies and vanishing vertical angular momentum and in the $\sqrt{J_R}$) versus J_ϕ plane (panel (e)), since they also attain very low values in the square root of the radial action.

TND RRLs cluster (green dots), as expected, in the right corner of the action diamond (panel (f)), since their action budget is mainly dominated by L_Z. Moreover, they are also distributed on a very tiny and compact slice in the Lindblad diagram with (panel (c)) very high L_Z values and intermediate orbital energies. At the same time, TND RRLs display large circularities, small eccentricities (panel (g)), and small $Z_{\rm max}$ (panel (h)) while in the eccentricity versus L_Z plane (panel (d)), and in the $\sqrt{J_R}$) versus J_ϕ plane (panel (e)) they cluster in the bottom right corner.

Candidate TCD RRLs (orange dots) share similar kinematic features, and they can also be easily identified, since they display a smooth transition between TND and halo RRLs in the different kinematic planes.

It is worth mentioning that the distribution of halo RRLs in the circularity versus $Z_{\rm max}$ plane (panel h) is far from being homogeneous. They show four distinct stellar arcs that move from circularities typical of TCD ($\lambda_Z > 0.25$) stars into circularities typical of RRLs with retrograde orbits ($\lambda_Z < -0.25$). Moving from the outskirts to smaller $Z_{\rm max}$

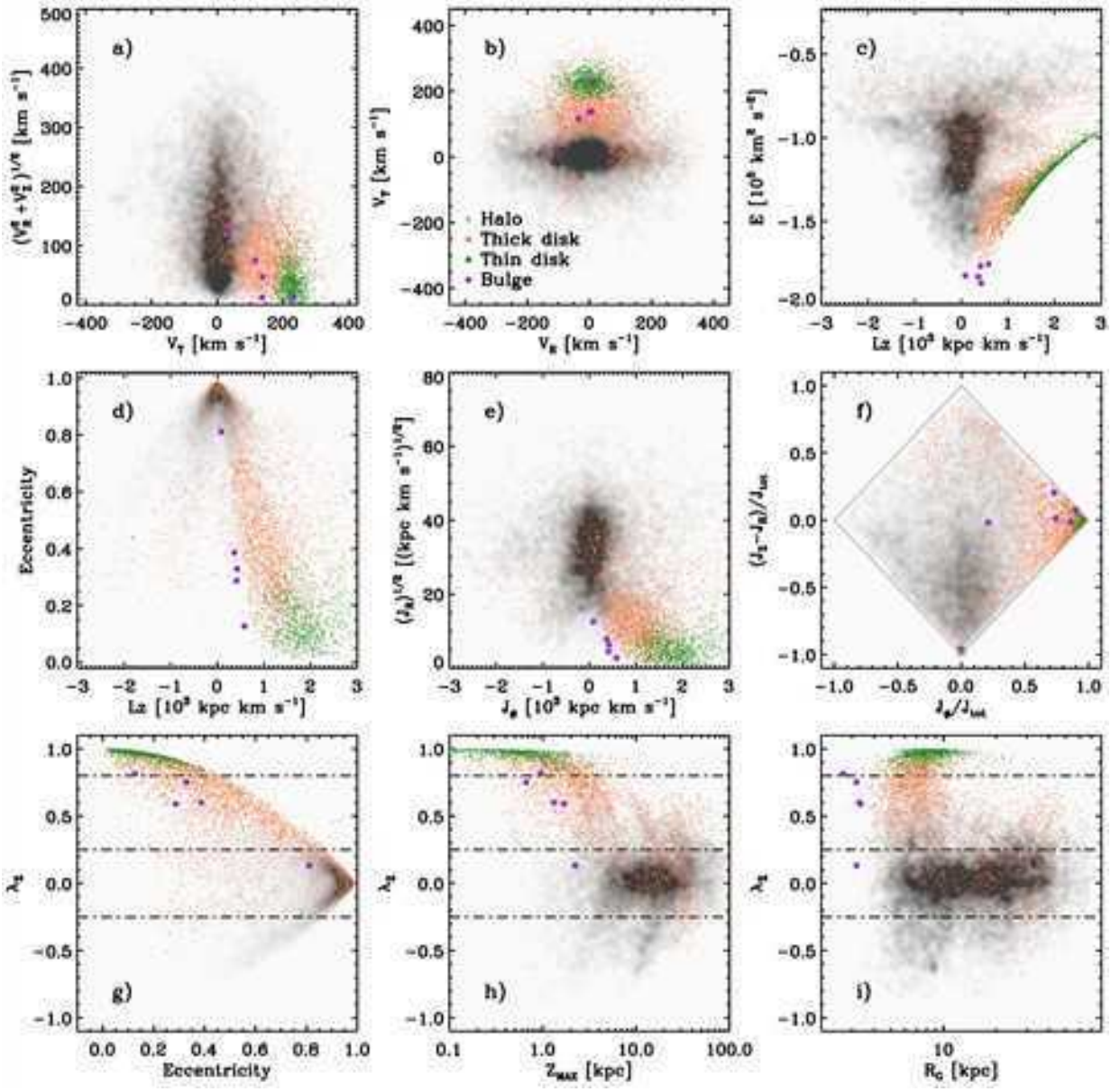

Figure 10. Kinematic planes for RRLs in the main Galactic components. Panel (a) [Toomre diagram]: RRL transversal velocity as a function of the sum in quadrature of radial and vertical velocity components ($\sqrt{V_R^2 + V_Z^2}$). TND and TCD RRLs are marked with green and orange dots, while bulge RRLs are marked with magenta dots. The shaded gray area shows the distribution of halo RRLs and RRLs in retrograde orbits. RRLs in the different Galactic components were selected according to T. Bensby et al. (2014), to circularity (retrograde), and to apocentric radius (bulge). See text for more details. Panel (b): RRL transversal velocity as a function of the RV (V_T versus V_R). Panel (c) [Lindblad diagram]: RRL orbital energy as a function of the vertical component of the angular momentum (E versus L_Z). Panel (d): Eccentricity versus L_Z. Panel (e): The square root of the radial action ($\sqrt{J_R}$) versus $J_\phi = L_Z$. Panel (f) [Action-diamond diagram]: $(J_Z - J_R)/J_{\rm tot}$ versus $J_\phi/J_{\rm tot}$, where $J_{\rm tot} = |J_\phi| + J_R + J_Z$). Panel (g): RRL circularity as a function of eccentricity. Panel (h): RRL circularity as a function of the maximum height above the Galactic plane (logarithmic axis). Panel (i): RRL circularity as a function of the Galactocentric distance (logarithmic axis).

distances they are located at $Z_{\rm max}$∼30–40 kpc, 10–20 kpc, 7–9 kpc, and 4–5 kpc. This appears as new evidence suggesting that RRL radial distribution might be affected either by early merging events (see next section) or by peculiar radial motions. Note that the lack of these features in the circularity versus Galactocentric distance plane indicates that they are mainly associated with variations perpendicular to the Galactic plane.

To investigate on a more quantitative basis the possible difference in kinematic properties introduced by the adopted MW potential, we also performed an independent selection of the four Galactic components by using the MW potential of P. J. McMillan (2017) as implemented in AGAMA (E. Vasiliev 2019). Data plotted in Figure 26 (Appendix B) show that the mean values and the standard deviations of both iron and α-element distribution functions for the four Galactic components are very similar. The similarity also applies to the different kinematic planes; indeed, Figure 27 (Appendix B) shows that the distribution of the RRLs associated with the four Galactic components are, within the errors, very similar (Figure 10). Note that there is, as expected, a difference in the energy adopted in the Lindblad plane (panel (c)) due to the mass differences between the MWPotential2014 and the McMillan17 potential.

3.2. Identification of Stellar Streams

The advent of homogeneous kinematical measurements for sizable sample of field stars together with accurate and homogeneous abundance measurements from ground-based spectroscopic surveys gave the impetus to a wide literature concerning the chemo-dynamical criteria to identify stars with a common origin (A. Helmi 2020; T. Antoja et al. 2020; D. K. Feuillet et al. 2021; D. Massari 2025, and references therein). In the following, we decided to use selection criteria that have already been suggested in the literature and the reason is twofold.

(i) We are planning to use the integrals of motion to identify cluster of RRLs in the different dynamical planes in order to have an objective and quantitative insight into the different identifications. However, a detailed clustering analysis is beyond the aim of the current investigation.

(ii) This is the very first time that the chemo-dynamics of a large sample of field RRLs is investigated on a quantitative basis and we are interested in the comparison with previous MW investigations based on different stellar tracers.

For the identification of the main stellar streams, such as Gaia–Sausage–Enceladus (GSE) and Sequoia, we adopted the same selection criteria adopted by D. K. Feuillet et al. (2021). A similar approach was also undertaken by P. Bonifacio et al. (2024) in their analysis of high-speed stars. Moreover, we also followed the identification of the Sagittarius (SGR) stream recently provided by T. Antoja et al. (2020), using over-densities in proper motion distributions provided by Gaia DR2. Note that for this stream we did not apply kinematic selections, we only performed a cross correlation between the SR3C catalog and their catalog of SGR candidates. Concerning the identification of RRLs in the Helmi stream, we adopted the kinematic criteria recently suggested by H. H. Koppelman et al. (2019) and D. Horta et al. (2023).

Figure 11 shows the identification of the different stellar streams in the same kinematic planes adopted to identify the Galactic components. RRLs that according to the kinematic criteria belong to GSE have been marked with green dots, while RRLs associated with the different Galactic components (see Figure 10) are shown as a shaded gray area. Candidate GSE RRLs can be easily identified, since they display a well-defined overdensity not only in the Toomre (panel (a)) and in the Lindblad (panel (c)) diagram but also in the action diamond (panel (f)). The compact distribution that GSE RRLs show in panel (h) further supports the evidence that they originated from a single merger event and their clustering in the bottom corner of the action diamond is probably tracing the actions of the progenitor. Candidate GSE RRLs also show a compact distribution in the square root of the radial action versus the vertical angular momentum (panel (e)) as originally suggested by D. K. Feuillet et al. (2021). Indeed, the GSE peaks at radial action values that are systematically larger than halo RRLs. Moreover, they also differ when compared with RRLs with retrograde orbits and with TND/TCD RRLs. Similar peaks for GSE RRLs can be easily identified in the eccentricity versus L_Z plane (panel (d)) and in the circularity versus eccentricity plane (panel (g)).

The identification of the Sequoia stream is more complex. Candidate Seq RRLs, marked with orange dots, cluster in the left corner of the action diamond, since this is the plane originally adopted by D. K. Feuillet et al. (2021). However, the Sequoia sample clearly splits into two different groups in the Lindblad diagram (at energy $E \simeq -1.1\ 10^5\ \mathrm{km^2\ s^{-2}}$): in the eccentricity versus L_Z plane, and in the $\sqrt{J_R}$ versus L_Z plane. It is worth mentioning that Sequoia RRLs display a well-defined minimum for $R_G \sim 12$ kpc in the circularity versus Galactocentric plane (panel (i)). We adopted this criterion to split the Sequoia candidate into Seq. 1 ($R_G \leqslant 12$ kpc) and Seq. 2 ($R_G > 12$ kpc) RRLs. In passing, we note that according to the separation in the Lindblad diagram there are solid reasons to believe that Section 1 RRLs might be associated with Thamnos RRLs (D24).

Candidate SGR RRLs (red dots) do not show clear overdensities in the kinematic planes. There are only two exceptions. They are relatively concentrated in the circularity versus Z_{max} plane and in the circularity versus R_G plane. Indeed, they cover a narrow range in Galactocentric distances ($R_G = 30$–40 kpc) and in maximum height above the Galactic plane ($Z_{max} = 20$–30 kpc). Moreover, there is also evidence for clustering in the top corner of the action diamond, but in the other kinematic planes they overlap with canonical outer halo RRLs. The compact distribution in Galactocentric distance and in Z_{max} further supports the evidence that SGR candidates in the current catalog mainly trace the SGR stream, with a minimal, if any, contribution from the SGR core.

Candidate Helmi RRLs (turquoise dots) display mixed behavior in the different kinematic planes. They show a smooth distribution in the Toomre diagram (panel (a)) and in the transversal velocity plane (panel (b)), but they show a well-defined concentration in the Lindblad plane across $E \sim -1.0\ 10^5\ \mathrm{km^2\ s^{-2}}$, $L_Z \sim 1.0\ 10^3\ \mathrm{kpc\ km\ s^{-1}}$ and a high-energy tail extending from $E \sim -0.9\ 10^5\ \mathrm{km^2\ s^{-2}}$. The distribution is relatively compact in the action-diamond plane (panel (f)) and in the circularity versus Z_{max} plane (panel (h)) and in the circularity versus R_G plane (panel i). Data plotted in the λ_Z versus Z_{max} plane indicate that candidate Helmi RRLs are mainly located in the TCD, since Z_{max} ranges from a few kpc to $\sim$20 kpc and λ_Z between 0.7 and 0.2. Further improvements in the kinematics selection of this stellar stream are highly recommended, since it is distributed between the TCD and the halo.

The circularity versus Z_{max} plane is a very interesting diagnostic to investigate the spatial distribution of stellar streams. Indeed, Sections 1 and 2 RRLs have retrograde orbits and display in this plane a well-defined separation also in Z_{max}. In particular, the Section 2 RRLs attain maximum heights above the Galactic plane that are larger than 9–10 kpc, while Section 1 RRls are located closer to the Galactic plane. It is worth mentioning, that in this plane Sequoia, and SGR RRLs appear to be associated with the stellar arcs discussed in the identification of the main Galactic component. SGR RRLs are associated with the stellar arc located at larger Galactocentric distances ($Z_{max} \sim$ 30–40 kpc) while Helmi and Section 2 RRL are associated with the stellar arc located at $Z_{max} \sim$ 10–20 kpc, and Section 1 to the stellar arcs located at 7–9 kpc, and 4–5 kpc. The main difference is that candidate Sequoia RRLs are in retrograde motion, while Helmi RRLs have prograde motion. A detailed discussion of these kinematic features is beyond the aim of the current investigation.

To investigate the global properties of the selected streams, Figure 12 shows the candidate RRLs in the Lindblad diagram (left panels) and in the circularity versus Galactocentric distance (right panels). In analogy with the analysis we performed to characterize the different Galactic components

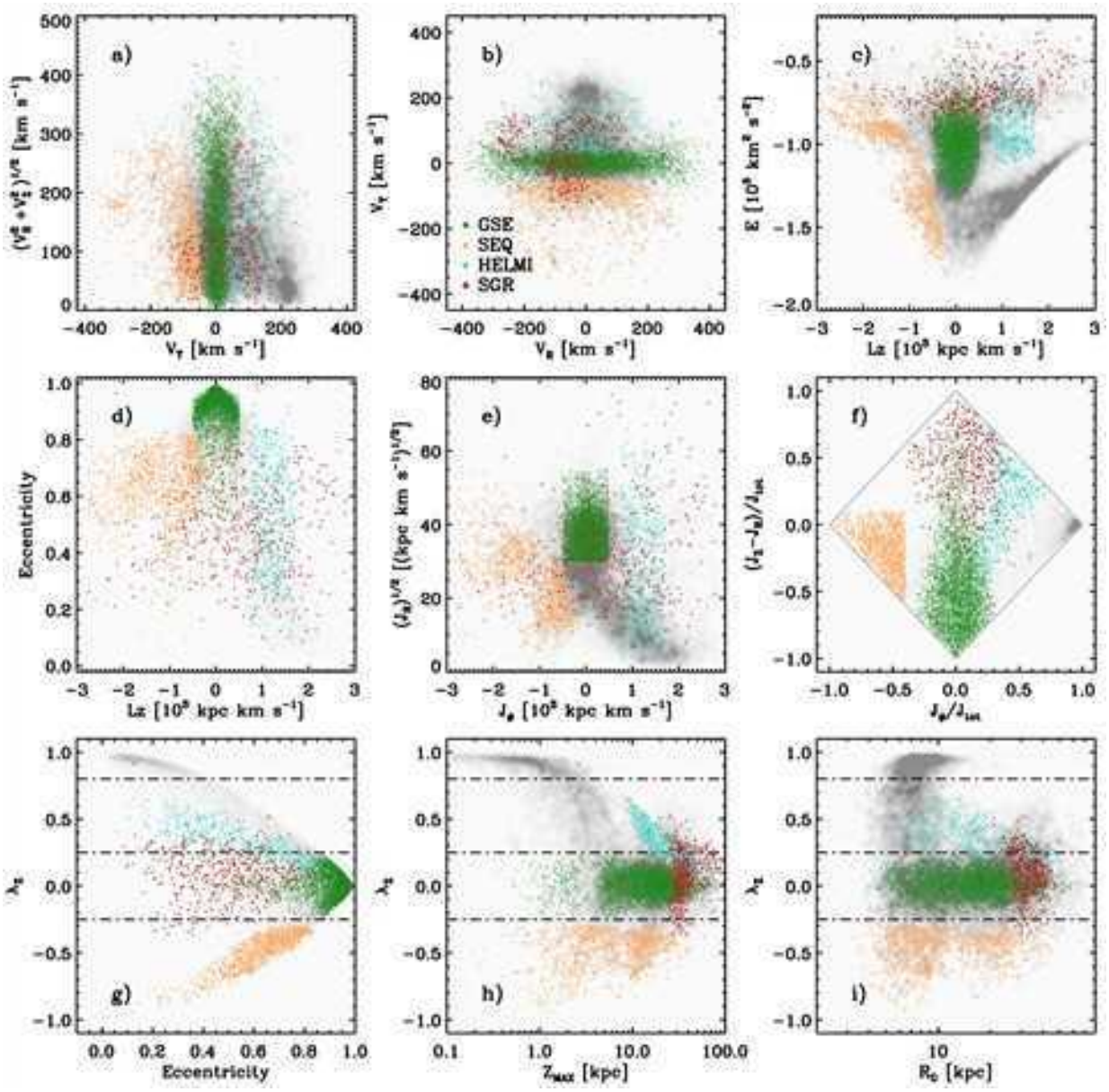

Figure 11. Kinematic planes for RRLs in the four selected stellar streams. The green dots mark candidate GSE RRLs, while orange dots display candidate SEQ1 and SEQ2 RRLS according to D. K. Feuillet et al. (2021). The turquoise dots mark Helmi RRLs, according to H. H. Koppelman et al. (2019) and D. Horta et al. (2023). The red dots show candidate SGR RRLs according to T. Antoja et al. (2020). The gray shaded area shows the same RRLs belonging to the main Galactic components plotted in Figure 10

(see Figure 7), the symbols were color coded according to the iron abundance (color bar in the inset). Data plotted in panels (a) and (e) display that GSE RRLs are quite homogeneous in iron abundance, indeed they are metal intermediate and show a homogeneous chemical enrichment not only in the range of energies covered in the Lindblad diagram but also in the wide range of Galactocentric distances they are covering (from $\sim$5 to $\sim$50 kpc).

Sequoia RRLs display a more complex distribution, since the Section 1 candidates located at modest Galactocentric distances display a broader iron distribution when compared with Section 2 candidates. This trend becomes even more clear for candidate Helmi RRLs, indeed RRLs either with TND kinematics or approaching TND kinematics are systematically more metal rich than RRLs with TCD kinematics located at larger Galactocentric distances. The candidate SGR RRLs display a homogeneous spatial distribution with a well-defined mix between metal-poor and metal-intermediate RRLs.

To further constrain the accuracy of the kinematic selections for the stellar streams, we decide to follow the same approach we adopted for the Galactic components. The left panels of Figure 13 show from top to bottom the IDFs for the selected stellar streams. GSE RRLs show an IDF that is, within the errors, quite similar to halo RRLs. The similarity also applies to the standard deviation (0.31 versus 0.37). Note that this comparison is quite robust, since we are comparing two samples with a similar number of RRLs (2754 versus 3179) and with a similar range in Galactocentric distances. However, GSE RRLs lack the metal-poor/metal-rich tails and their α-element distribution (top right panel of Figure 13) is quite compact.

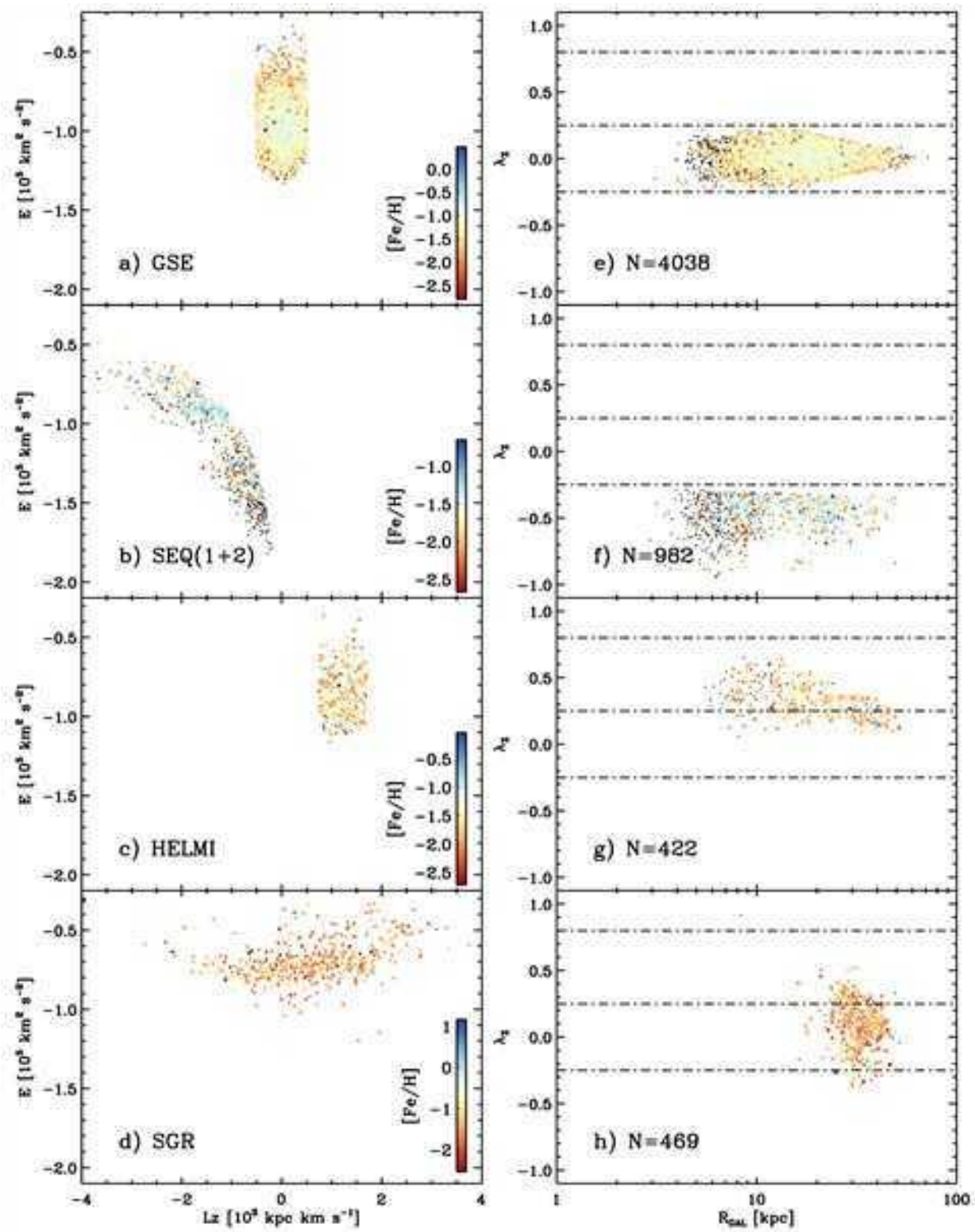

Figure 12. Left: Lindblad diagram for the four streams identified in Figure 11. The symbols are color coded according to the iron abundance (see color bar in the inset). Right: Same as the left, but the circularity of the orbits (λ_Z) is plotted as a function of the Galactocentric distance. The numbers of RRLs in the different streams are labeled. See text for more details.

The Section 1 and Section 2 RRLs are also quite similar to halo RRLs, indeed their IDFs peak at [Fe/H] = −1.68 and −1.60. However, Section 2 RRLs have a more symmetrical IDF and, in particular, a smaller standard deviation (0.28 versus 0.38). Section 2 RRLs also lack the metal-poor/metal-rich tails and show a compact distribution in α elements. The chemical evidence for Section 1 RRLs is less clear; however, the evidence that Section 1 and Section 2 RRLs have retrograde orbits and cover limited ranges in Galactocentric distances further supports the solid identification of this stellar stream.

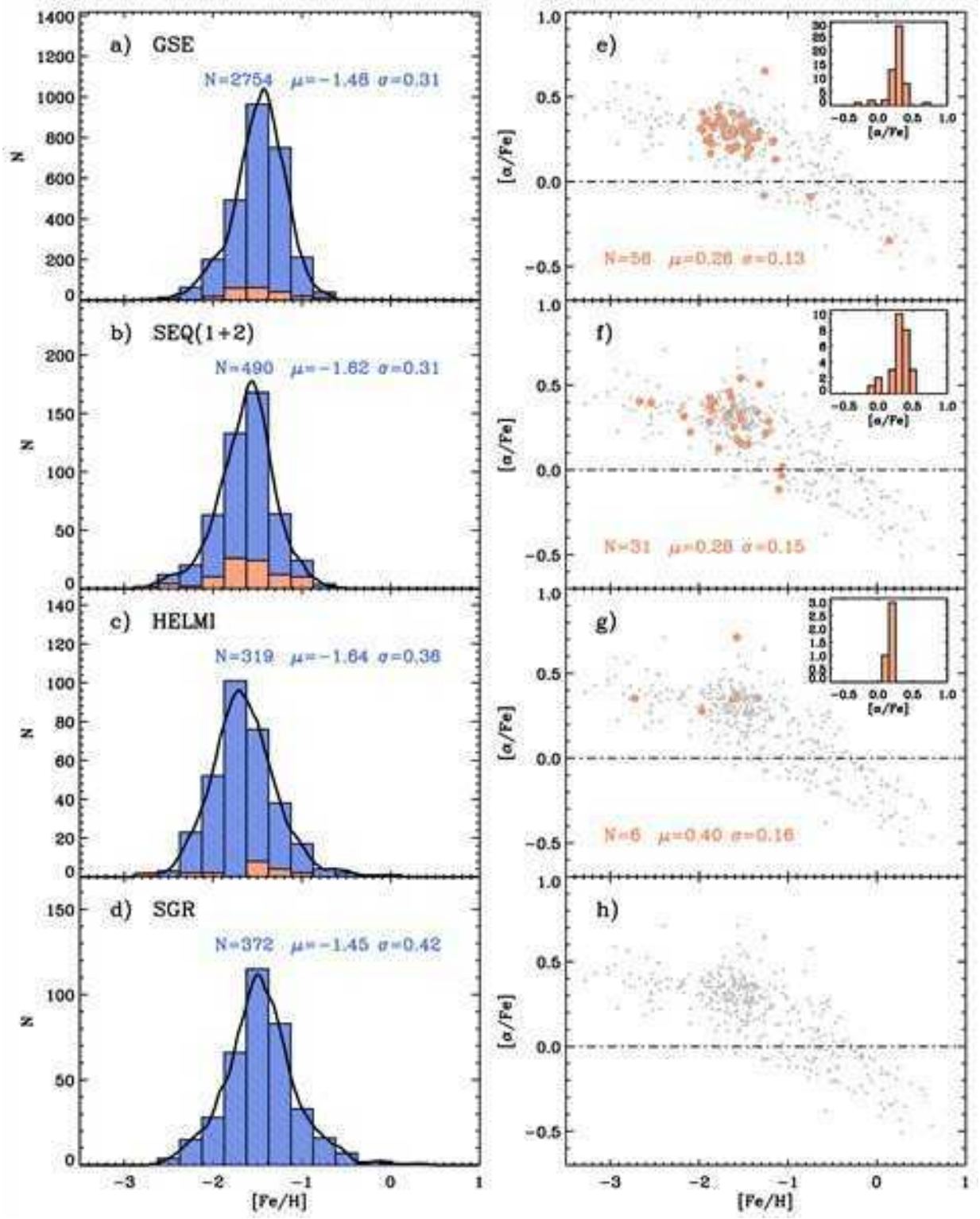

Figure 13. Left: IDF for the four stellar streams (see labeled names) identified in Figure 11. The black lines show the running average over the entire subsample. The number of RRLs, the mean, and the standard deviations are also labeled. Right: same as the left, but for the [α/Fe] abundance ratios as a function of the iron abundance. The gray dots display the entire Galactic sample, while the orange circles individual abundances in the four stellar streams. The inset shows the [α/Fe] distribution function.

The Helmi RRLs display an IDF function very similar to halo RRLs, indeed their IDF peaks at [Fe/H] $= -1.64$ (versus -1.56) and their standard deviation is $\sim$0.36 (versus 0.37).

The SGR RRLs also have very similar IDF and standard deviation (0.42 versus 0.37) to the halo RRLs, with marginal evidence for a metal-poor/metal-rich tail. Moreover, they are located at large Galactocentric distances and we still lack measurements of their α-element abundances.

Finally, to further constrain possible systematics in the kinematic properties of candidate RRLs associated with the

four stellar streams we also performed an independent orbital integration by using the MW potential of P. J. McMillan (2017). Data plotted in Figure 28 (Appendix B) shows that four stellar streams display in the different kinematic planes distributions that are, within the errors, quite similar to the distributions based on the MW potential of J. Bovy (2015) (see Figure 11).

4. Comparison with Different Stellar Tracers

To validate the current metallicity scale we compare the chemo-dynamical properties of old stellar tracer like RRLs with similar properties for GGCs that are popular tracers of old stellar populations. The kinematic properties of GGCs were estimated by using proper motions and distances provided by H. Baumgardt et al. (2019) together with the same Galactic potential adopted for field RRLs. The association with the different Galactic components was performed by using the same criteria adopted for field RRLs (see Section 3.1). Concerning the association of GGCs to the different stellar streams, we took advantage of the recent detailed chemo-dynamical investigation provided by D. Massari (2025).

Several investigations in the literature have recently provided identification of GC likely sharing common origins by using either different chemical and dynamical criteria or different input parameters (distances, kinematics, metallicity distribution functions), or different theoretical frameworks. Typically, they reach different conclusions concerning the conatal GC associated with the different stellar streams. Moreover, and even more importantly, there is mounting theoretical evidence that accreted GCs do not show dynamical coherence, since they do not cluster in typical kinematic spaces (G. Pagnini et al. 2023).

In the following, we perform a preliminary comparison between field RRLs and GGCs in the canonical kinematic planes and in the radial gradients for a consistency check between old stellar tracers.

For this purpose, we put together a catalog of GGCs by collecting data from the literature, more specifically 165 from D. Massari (2025) and 19 from W. E. Harris (1996, 2010). The metallicities and $[\alpha/Fe]$ values were adopted from E. Carretta et al. (2009, plus Carretta private communication, 27 GCs) and from M. Zoccali et al. (2004, plus Zoccali private communication, four bulge GCs).

Figure 14 shows the comparison in the same kinematic planes between the four stellar streams and the GGCs that according to kinematic selections have been associated with the same stellar streams. Data plotted in this figure bring forward a few empirical circumstances:

(a) *GSE*. Field RRLs and GGCs associated with GSE show a very similar distribution, not only in the classical six dynamical planes but also in the planes based on the circularity versus eccentricity, $Z_{\rm max}$ and Galactocentric distance (panels (g), (h), (i)). There is evidence of two outliers (Djorgovski 1, NGC 6333 [M9]) in the Toomre diagram (panel (a)) and in the radial versus vertical velocity (panel (b)), since they attain transversal velocities that are systematically larger than the bulk of the stream. A few outliers are also present in the action-diamond plane (panel (f)), indeed a few GGCs associated with GSE attain $J_\phi/J_{\rm tot}$ values that are either systematically smaller (NGC 288, NGC 6205 [M13], NGC 7099 [M30]) or larger (Djorgovski 1) than the bulk of the stream. Moreover, Ter 10, Djorgovski 1, and NGC 6333 appear to be outliers in the eccentricity versus Galactocentric distance, since their distances are systematically smaller than the bulk of the GSE stream.

(b) *Sequoia*. There are nine GGCs that have been associated with the Sequoia stellar stream and their distribution in the kinematic planes marginally follows the RRLs associated with the same stream. Several outliers are present not only in the Toomre diagram (panel (c)), in the Lindblad diagram (panel (c)), but also in the action plane (panel (f)) in which they attain $J_\phi/J_{\rm tot}$ values that are systematically larger than the bulk of the stream (AM4, IC 4499, Pal 13, NGC 2298, NGC 5466, NGC 7006 [C42]). Data plotted in the circularity versus Galactocentric distance plane (panel (i)) suggest that three GGCs NGC 5139, NGC 6101, and NGC 3201 might be associated with Section 1, while the data plotted in the circularity versus $Z_{\rm max}$ (panel (h)) suggest that NGC 3201 and NGC 6101 are associated with Section 2 and NGC 5139 to Section 1. Moreover, at least five (AM4, Pal 13, NGC 2298, NGC 5466, NGC 7006) out of the nine GGCs associated to this stream are located, according to the current classification, at the transition between prograde and retrograde orbits. In order to constrain this issue on a quantitative basis, we estimated the kinematic properties of both field RRLs and GGCs by using the Galactic potential suggested by P. J. McMillan (2017) and we found that the quoted clusters are located once again at the transition between prograde and retrograde orbits.

(c) *Helmi*. The comparison in the kinematic planes indicates that field RRLs and GGCs associated with the Helmi stream share similar distributions. There are a few outliers that show up not only in the Toomre (panel (a)) and in the Lindblad (panel (c)) diagram (NGC 4590 [M68], E 3) but also in the eccentricity versus L_Z and in the action-diamond plane (NGC 6426, NGC 7078 [M15]). The comparison is hampered by the fact that RRLs associated with the Helmi stream cover a very wide range in Galactocentric distances.

(d) *Sagittarius*. There are seven GGCs that have been associated with the SGR stream. The globular Pal 12 seems to be an outlier in the Toomre diagram (panel (a)) and in the radial versus vertical velocity (panel (b)), but it follows the bulk of the SGR stream in the other dynamical planes. Note that the association between NGC 6715 (M54) and SGR is supported not only by the Lindblad diagram and by the action-diamond plane but also by the plane showing the circularity of the orbit as a function of $Z_{\rm max}$. They typically display a compact spatial distribution (bottom panels). However, the distribution in the circularity versus $R_{\rm G}$ (panel (i)) suggests that five GGCs (Pal 12, NGC 6715, Ter 7, Ter 8, Arp 2) are associated with the core of the SGR stellar stream ($R_{\rm G} \leqslant 25$ kpc) while the other two (Laevens 3, NGC 2419), located at larger Galactocentric distances, are associated with the stream of this disrupting galaxy.

The same comparison was also performed using the chemical planes [α/Fe] versus [Fe/H]. Panel (a) of Figure 15 shows that candidate TCD RRLs cover a broad range in metallicity, but they are systematically more α enhanced than nearby dwarf galaxies. Interestingly enough, GGCs that have been associated with the TCD (red circles, T. M. Callingham et al. 2022) only cover the metal-intermediate regime and they are, at fixed iron abundance, more α enhanced than TCD RRLs.

The comparison with halo RRLs (panel (c)) is more homogeneous, indeed halo RRLs and RRLs with retrograde orbits (panel (e)) show as expected a similar trend in [α/Fe]

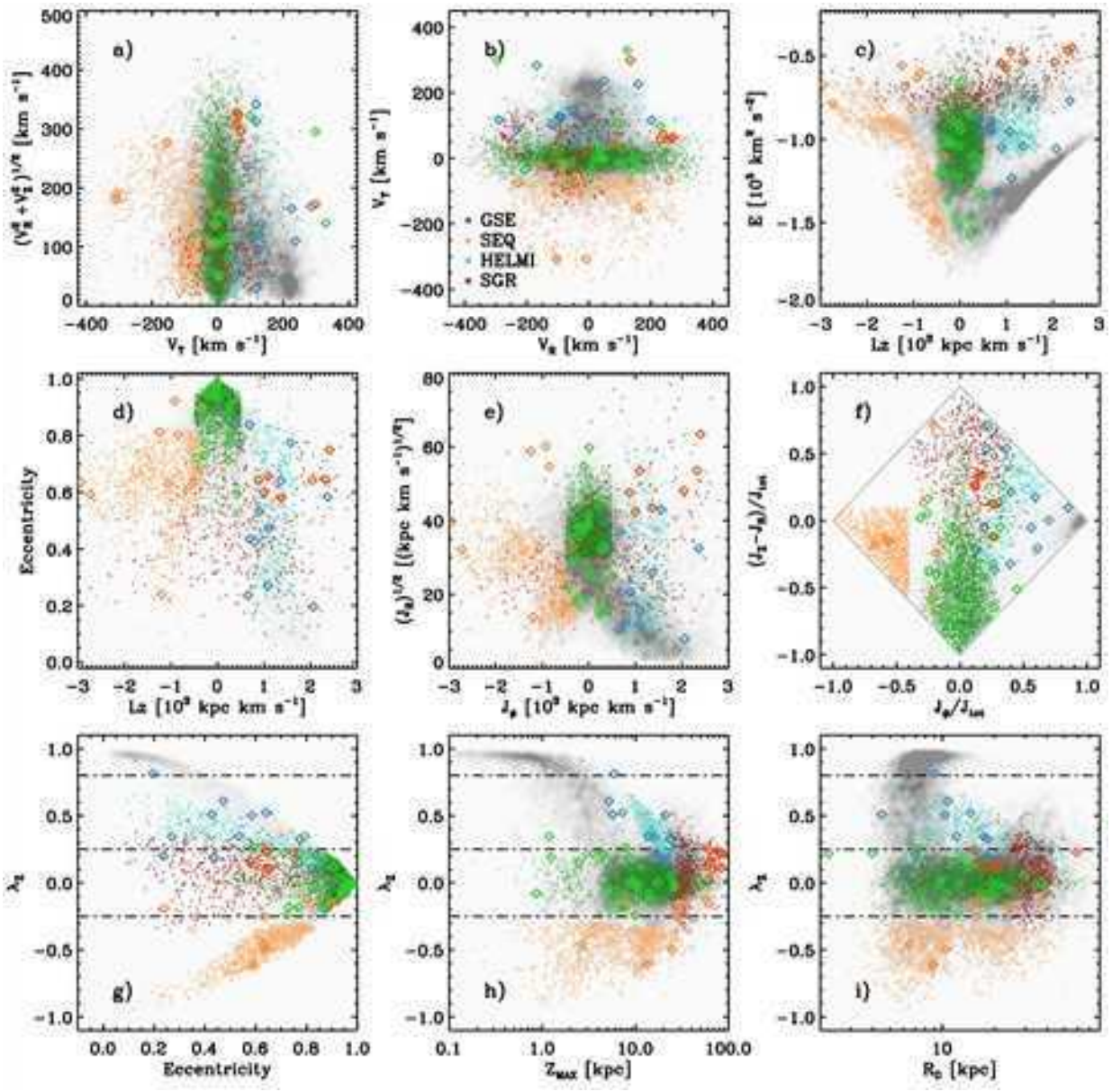

Figure 14. Comparison in the kinematic planes between field RRLs in the selected stellar streams and GGCs that have been associated with the same stellar streams (D. Massari 2025). The symbols and the colors for field RRLs are the same as in Figure 11. The GCs are marked with green (GSE), orange (Sequoia), cyan (Helmi), and red (SGR) diamonds.

versus [Fe/H] and agree quite well with GGCs. Moreover, in the metal-poor tail ([Fe/H] $\leqslant -2$) they also agree with nearby dwarf galaxies, while in the metal-intermediate regime field RRLs and GGCs are systematically more α enhanced (see for more details M. Fabrizio et al. 2015).

The comparison of RRLs associated with the three stellar streams and nearby stellar systems (right panels of Figure 15) shows quite clearly that RRLs associated with GSE and Sequoia attain, at fixed iron abundance, α-element abundances similar to the GGCs associated with these streams. Thus, supporting the current associations. The dwarf galaxies are once again systematically more α poor in the metal-poor/metal-intermediate regime. The comparison with nearby stellar systems is partially hampered either by the lack or by the limited number of dwarf galaxies and GGCs more metal rich than [Fe/H] $\geqslant -1$.

To overcome this limitation, panel (a) of Figure 16 shows a similar comparison as in Figure 15, but with field stars observed either by APOGEE (B. Abolfathi et al. 2018) or by P. E. Nissen and W. J. Schuster (2010; NS10) in the solar neighborhood. The former sample is plotted as a gray shaded area, while the latter is plotted with different symbols: red crosses show stars with a high-α abundance, light blue crosses stars with low-α abundance, and green crosses candidate TCD stars.

The TCD RRLs (panel a) display a trend quite similar to the low-α subsample collected by NS10. The main difference is that TCD RRLs move into the metal-rich regime and display, at fixed iron content, a larger spread in α abundance. The similarity is also quite good with APOGEE. Indeed, they attain similar α values in the metal-intermediate and in the metal-rich regimes. Field RRLs display a plume of field RRLs across solar iron abundance that is systematically more α poor when compared with APOGEE RRLs.

Panel (c) and panel (e) of the same figure show that halo and retrograde RRLs are, as expected, systematically more

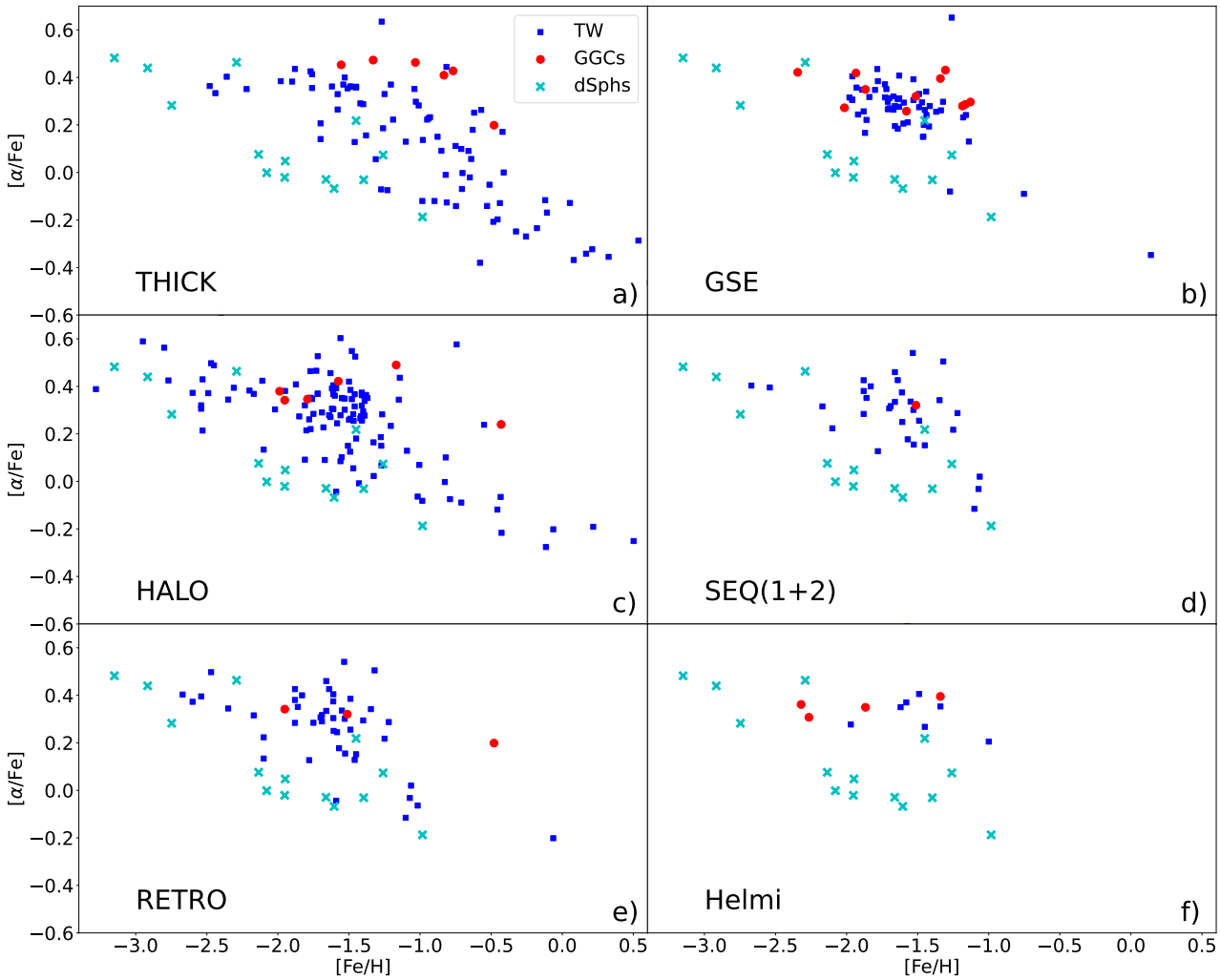

Figure 15. Comparison in the chemical plane ([α/Fe] versus [Fe/H]) among field RRLs (blue squares) in different Galactic components (left panels) and in three stellar streams (right panels) with GGCs (red circles) and nearby dwarf galaxies (light blue crosses). RRLs with retrograde orbits are plotted in the bottom left panel as orange squares.

metal poor when compared with APOGEE and SN subsamples. Moreover, in the metal-intermediate regime ($-1.5 \leqslant$ [Fe/H] $\leqslant -1.0$) halo RRLs display a continuous transition between the α-rich and the α-poor regimes. Data plotted in the left panels indicate that field RRLs show a steady decrease in α abundances when moving from the metal-poor to the metal-rich regime, while field stars display a well-defined dichotomy in α abundance. Note that this evidence applies to TCD, halo, and retro RRLs.

The right panels show that RRLs in the three stellar streams minimally overlap with literature samples. Indeed, GSE RRLs (panel (b)) are mainly located in the metal-intermediate regime and they are systematically more α enhanced than both APOGEE and SN samples. The same outcome applies to Sequoia RRLs (panel (d)). The Helmi RRLs only marginally overlap with field stars in the metal-intermediate regime, but their trend is similar to Halo+Retro RRLs (panel (f)).

5. Radial Metallicity Gradient

5.1. RRLs in Galactic Components

Key information concerning the mass assembly history of the different Galactic components is implanted in radial metallicity gradients. Figure 17 shows from top to bottom the iron radial gradient for the four different Galactic components as a function of Galactocentric distance (panels (a), (d), (g)), distance projected onto the Galactic plane (panels (b), (e), (h)), and as a function of the maximum height above the Galactic plane (panels (c), (f), (i)). Data plotted in this figure bring forward several interesting features that are discussed in more detail in the following.

(i) *TCD*. The TCD (middle panels (d), (e), (f)] of Figure 17) shows well-defined radial gradients as a function of R_G, ω, and Z_{max}. It is worth mentioning that TCD RRLs display a significant increase in the dispersion of iron abundances for Galactocentric distances smaller than the solar circle ($R_G \sim 8$–10 kpc). A similar increase in the spread of the iron abundance is also present in ω and in Z_{max}, but at slightly different radial distances. The standard deviations in iron abundance plotted in the insets show that the increase in these regions is a factor of two larger when compared with larger distances.

The TCD RRLs were ranked as a function of the Galactocentric distance (R_G) to avoid spurious fluctuations in the mean iron abundance and we estimated the running average by using the first 80 RRLs in the list. The mean

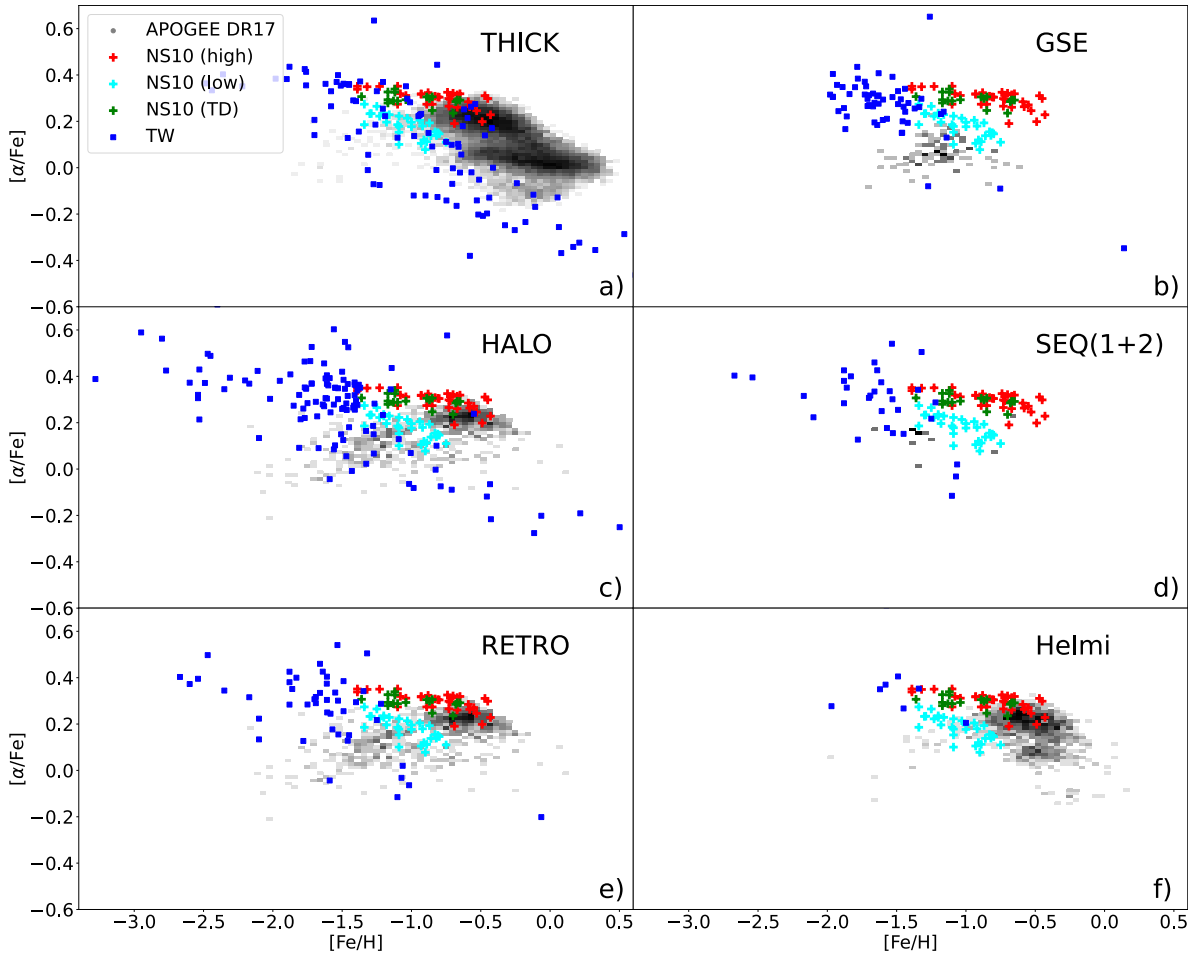

Figure 16. Same as Figure 15, but the comparison is between field RRLs in the current catalog (blue squares) and field stars observed by APOGEE (gray shaded area, B. Abolfathi et al. 2018) and by NS10. The latter sample is plotted with different symbols: red crosses show stars with a high-α abundance, light blue crosses stars with low-α abundance, and green crosses are candidate TCD stars.

distance and the mean iron abundance ($<$ [Fe/H] $>$) inside the box were estimated as the mean over the individual distances and iron abundances of the same 80 RRLs. Subsequently, we estimated the same quantities by moving outward the box by one object in the ranked list until we took account for the last 80 RRLs in the TCD sample with the largest distance. The same approach and the same number of objects in the running box were used to estimate the averages as a function of ω, and $Z_{\rm max}$ and they are plotted as blue lines, while their standard deviations are plotted as orange lines in the middle panels of Figure 17. We performed a number of simulations by changing the number of RRLs included in the running box and the number of RRLs adopted to move outwards the box and we found that both the current running average and standard deviations are quite solid.

In order to provide a more quantitative analysis of the radial gradients, we performed a linear fit over the three different distances and they are plotted as dashed–dotted lines in the middle panels. The iron gradient is as expected negative and the slope is steeper in $R_{\rm G}$ and in ω than in $Z_{\rm max}$ (see Table 2). Interestingly enough, the iron gradient is changing from metal intermediate ([Fe/H] ~ -1) in the innermost TCD regions to metal poor ([Fe/H] ~ -2) in the outermost TCD regions.

The transition across the solar circle is even more clear in Galactocentric distance and in cylindrical coordinates, and indeed the RRL iron gradient becomes steeper for $R_{\rm G}$ and $\omega \leqslant 10$ kpc (panels (d), (e)). Note that the lack of objects with $R_{\rm G}$ smaller than $\sim$5 kpc indicates that our sample includes a large number of RRLs that are located in the innermost Galactic regions, but above/below the Galactic bulge ($R_{\rm G}$[Bulge] $\lesssim 3.5$ kpc, M. Zoccali et al. 2024).

(ii) *TND*. There is evidence that RRLs associated with the TND (top panels (a), (b), (c) of Figure 17) also show well-defined radial gradients as a function of $R_{\rm G}$, ω, and in particular as a function of $Z_{\rm max}$. The sample in the outer disk is limited, but the decrease toward more metal-poor abundances is quite clear. This circumstantial evidence supports the working hypothesis that the inside-out scenario for the chemical enrichment of TND was already in place in the early phase of MW formation. The dashed–dotted lines display the linear fit across TND RRLs. The change in the slope across the solar circle was neglected, since it is mainly caused by the significant increase in metallicity dispersion. Note that the iron gradients associated with TND RRLs typically cover a narrower range in distances, but they are a factor of two/three steeper when compared with the iron gradients of TCD RRLs.

(iii) *Halo+Retro*. Global halo RRLs display a very mild radial gradient when moving from the innermost to the outermost regions (panels (g), (h), (i) of Figure 17). The spread in iron abundance plotted in the insets is large not only across the solar circle, but also for $R_{\rm G} \sim$ 40 kpc. The linear fits (dashed–dotted lines) to the iron gradients give slopes that are,

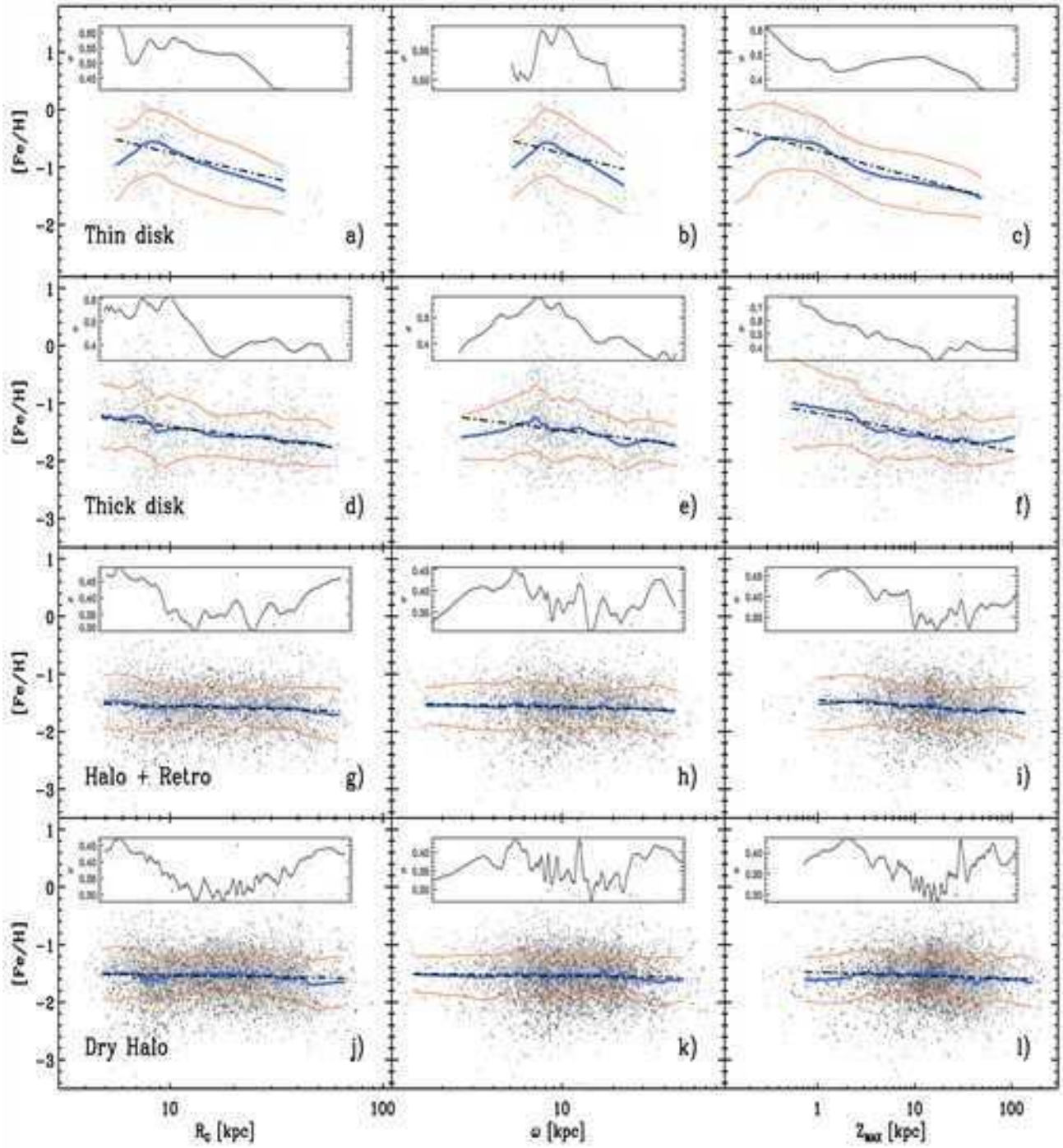

Figure 17. Panels (a), (b), (c): iron abundance for TND RRLs as a function of Galactocentric distance (panel (a)), distance projected onto the Galactic plane (panel (b)), and maximum height above the Galactic plane (panel (c)). The X-axes are in logarithmic scale. The blue lines display the running average, while the orange lines the standard deviation of the running average. The dashed–dotted lines show the linear fit over the different subsamples. The insets display the standard deviation of the spectroscopic sample as a function of distance. Panels (d), (e), (f): same as the top, but for TCD RRLs. Panels (g), (h), (i): same as the top, but for Halo+Retro RRLs. Panels (j), (k), (l): same as the top, but for dry Halo+Retro RRLs. See text for more details.

on average, more than one order of magnitude shallower than TND RRLs, and at least a factor of five shallower than TCD RRLs. The iron abundances of the RRLs with retrograde orbits (black dots) display similar radial trends.

The Halo+Retro RRLs show a steady increase in iron content across the solar circle. The mean iron abundance increases by more than 0.3 dex when moving from $R_G \sim 10$ kpc to $R_G \sim 7$ kpc. This evidence supports previous findings by A. C. Layden (1994), N. B. Suntzeff et al. (1994) and more recently by T. D. Kinman et al. (2012). The change across the solar circle is also supported by the gradient projected onto the Galactic plane (panel (h)).

(iv) *Dry halo*. The above discussion concerning the iron radial gradients is based on the global halo sample, i.e., the RRLs that according to our selection criteria have halo kinematics (see Section 3.1). However, this sample also includes RRLs that have been associated with four different stellar streams (see Section 3.2). We call dry halo the sample

Table 2

Radial Iron Gradients for TND, TCD, and Halo RRLs by Using Either Logarithmic ([Fe/H] = $\alpha + \beta \times \log(dis)$) or Linear ([Fe/H] = $\alpha + \beta \times$ dis) Distances (kpc), Where the Distance is Either the Galactocentric Distance (R_G), or the Distance Projected onto the Galactic Plane (ω), or Z_{max} or the Height Above the Galactic Plane (Z) in Absolute Value

Dis.	TND		Thick Disk		Global Halo		Dry Halo	
Logarithmic								
R_G	0.158 ± 0.206	−0.907 ± 0.206(0.55)[a]	−0.922 ± 0.060	−0.479 ± 0.050(0.49)	−1.450 ± 0.029	−0.104 ± 0.024(0.38)	−1.474 ± 0.022	−0.057 ± 0.017(0.36)
ω	−0.006 ± 0.245	−0.754 ± 0.250(0.56)	−1.096 ± 0.060	−0.369 ± 0.056(0.50)	−1.503 ± 0.024	−0.071 ± 0.022(0.38)	−1.501 ± 0.018	−0.041 ± 0.016(0.36)
Z_{max}	−0.715 ± 0.035	−0.461 ± 0.062(0.51)	−1.172 ± 0.029	−0.328 ± 0.026(0.47)	−1.451 ± 0.019	−0.106 ± 0.015(0.37)	−1.478 ± 0.014	−0.055 ± 0.011(0.36)
$\|Z\|$	−0.787 ± 0.038	−0.335 ± 0.058(0.54)	−1.272 ± 0.023	−0.286 ± 0.025(0.48)	−1.540 ± 0.015	−0.039 ± 0.014(0.38)	−1.539 ± 0.010	−0.005 ± 0.009(0.36)
Linear								
R_G	−0.456 ± 0.066	−0.026 ± 0.005(0.54)	−1.294 ± 0.026	−0.010 ± 0.001(0.49)	−1.531 ± 0.012	−0.002 ± 0.001(0.38)	−1.505 ± 0.008	−0.002 ± 0.001(0.36)
ω	−0.392 ± 0.094	−0.034 ± 0.009(0.56)	−1.328 ± 0.027	−0.011 ± 0.002(0.50)	−1.545 ± 0.012	−0.002 ± 0.001(0.38)	−1.518 ± 0.008	−0.002 ± 0.001(0.36)
Z_{max}	−0.674 ± 0.039	−0.013 ± 0.002(0.54)	−1.381 ± 0.020	−0.005 ± 0.001(0.49)	−1.543 ± 0.009	−0.001 ± 0.001(0.37)	−1.516 ± 0.006	−0.001 ± 0.001(0.35)
$\|Z\|$	−0.658 ± 0.039	−0.031 ± 0.005(0.53)	−1.345 ± 0.021	−0.012 ± 0.001(0.49)	−1.544 ± 0.010	−0.002 ± 0.001(0.38)	−1.520 ± 0.007	−0.002 ± 0.001(0.36)

Note.

[a] The numbers in parentheses are the standard deviations (dex).

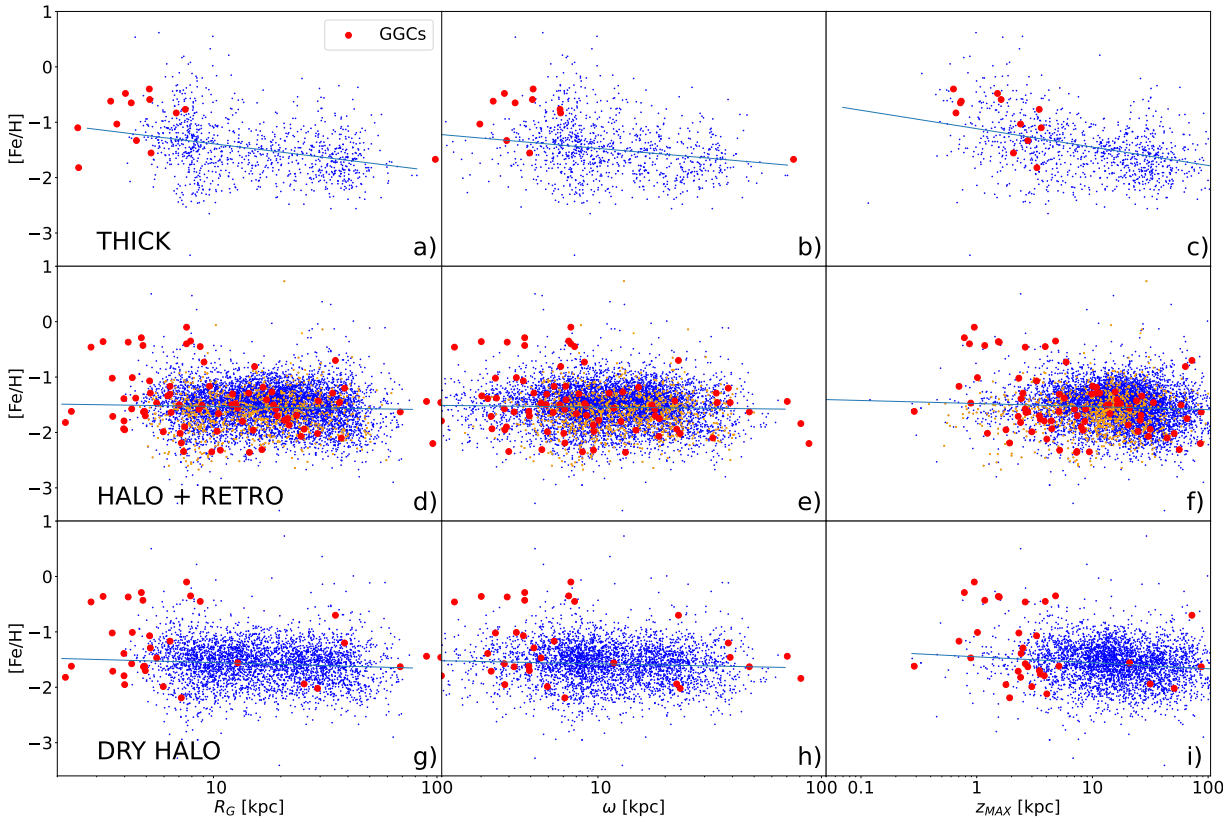

Figure 18. Comparison between the iron radial gradients of field RRLs and GGCs. From top to bottom, the different panels display the Galactic components identified and discussed in Section 3.1. The red circles mark GGCs associated, according to the current kinematic criteria, with the different Galactic components.

of pure halo RRLs, i.e., those that have not been associated with any of the quoted stellar streams. We performed once again the linear fits to the iron radial gradients and, interestingly enough, we found that iron gradients are similar when compared with the global halo (see Table 2). This suggests that the inclusion of RRLs belonging to stellar streams does not change the slope. The standard deviations of the linear relations of the dry halo are slightly smaller (0.36 versus 0.38).

Furthermore, we performed, as a consistency check, the comparison between the iron radial gradient of field RRLs (see, e.g., Figure 17) with GGCs associated with the Galactic components. The data plotted in Figure 18 display a global agreement in R_G, ω, and in particular in Z_{max}. There is only a limited sample of GGCs associated with the TCD, but the radial trends are quite similar for the different Galactic components and for the dry halo.

The variation of the radial metallicity gradients as a function of stellar age has been investigated in a number of empirical and theoretical investigations (R. Roškar et al. 2008). They are mainly focused on the Galactic TND and they typically indicate an overall flattening and an increase in spread of the radial gradients with time due to stellar radial heating and stellar migration (S. Daflon & K. Cunha 2004; B. Ratcliffe et al. 2023). However, the possible presence of a break at intermediate ages (F. Anders et al. 2017; E. Willett et al. 2023) is still debated.

In the current investigation we are only using old stellar tracers, and the comparison with theoretical predictions is beyond the aim of the current investigation. However, it is worth mentioning that P. B. Tissera et al. (2014) investigated the metallicity profiles of six simulated MW-like galaxies from the Aquarius Project and their predicted slopes are consistent with the current halo estimates. In particular, they found that flat slopes are often found in haloes made up by a mixture of satellites with different masses, i.e., a more balance contribution of small and massive satellites.

In closing this section, it is worth mentioning that the main reason why we adopted a logarithmic fit is based on plain physical arguments. Radial abundance gradients mainly trace the density gradient across the Galactic spheroid. The density typically follows a power-law distribution and a linear fit in a log–log plane is supporting this global trend. Moreover, the residuals display an increase in dispersion at small and large distances. We performed a number of numerical simulations using several analytical functions, and we found that the use of a logarithmic distance improves the fit at small and large distances. The current evidence indicates that in these regions the density profile might be more complex than predicted by a simple power law. However, for the sake of comparison with similar estimates available in the literature, we also performed a fit of the radial gradient by using linear distances (see Figure 29 in the Appendix C). The global standard deviations of logarithmic and linear fits are, as expected, quite similar, indeed the number of RRLs located at small and large distances are a modest subsample. The coefficients and the standard deviations of the logarithmic and linear fits are listed in Table 2.

5.2. RRLs in Stellar Streams

In this section we deal with the radial iron gradient in the stellar streams discussed in Section 3.2. Data plotted in the top

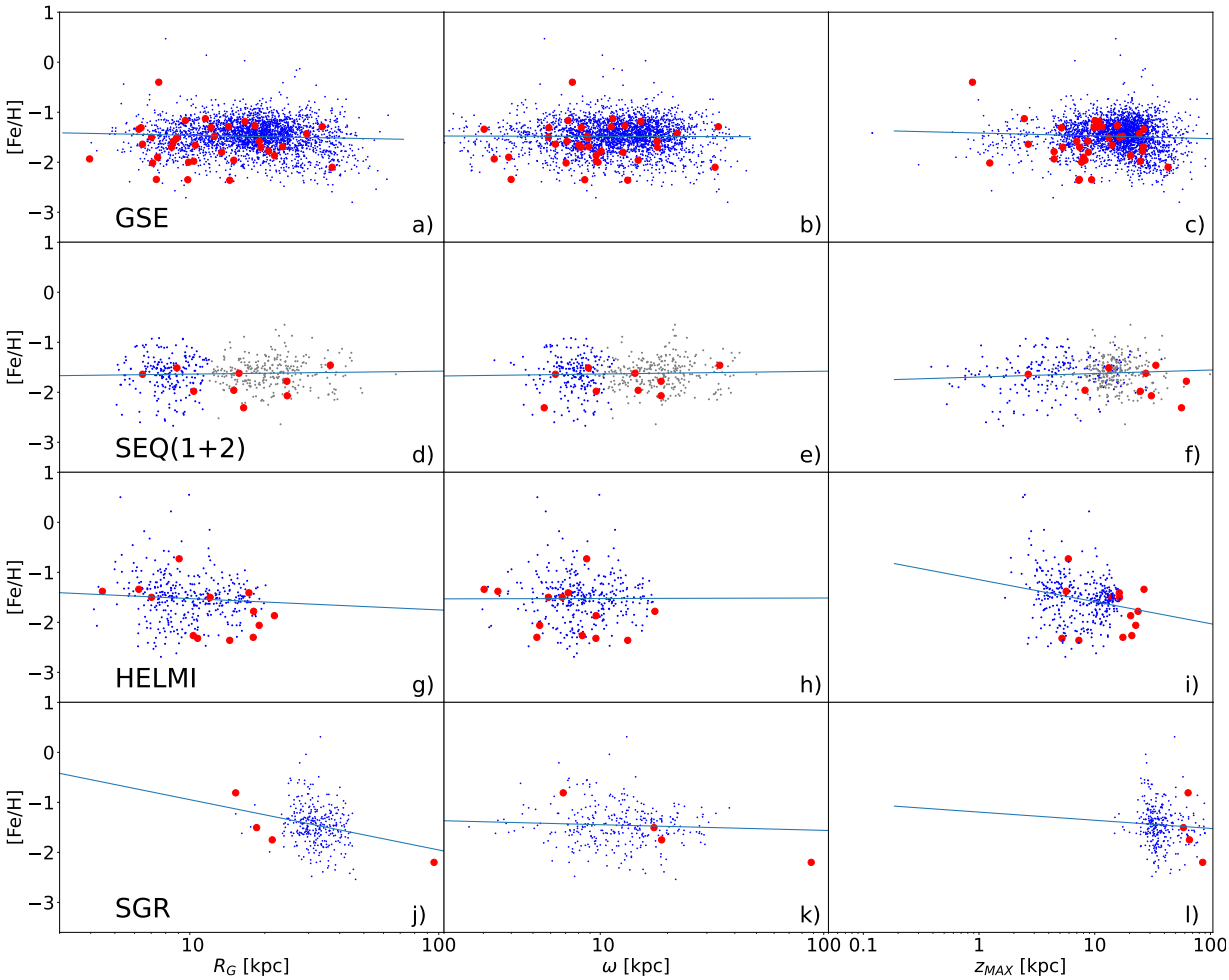

Figure 19. Same as Figure 18, but for the four different stellar streams discussed in Section 3.2.

panels of Figure 19 show that GSE RRLs do not display any radial gradient and its spread is quite constant over the entire range in distance covered by the sample. However, the distribution of RRLs as a function of Z_{max} (panel (c)) suggests two well-defined gaps. The former one located between $Z_{max} \sim 1$ and 8 kpc and the latter between $Z_{max} \sim 10$ and 12 kpc. There are reasons to believe that the occurrence of these gaps is mainly a consequence of the accuracy of individual RRL distances, and they suggest that the current identification of GSE might include different substreams. The comparison between GGCs associated with GSE and candidate GSE RRLs is quite good, since they overlap with each other. Interestingly enough, the GC associated with GSE displays a spread in iron abundance similar to GSE RRLs.

On the other hand, Section 1 RRLs (panels (d), (e), (f) of Figure 19) display a very compact spatial distribution, while Section 2 RRLs display a broader radial distribution, thus further supporting the separation suggested on the basis of the kinematic planes. It is worth mentioning that there is mild evidence either for a well-defined minimum or a gap for $R_G \sim 12$ kpc and $\omega \sim 10$ kpc, but a solid identification awaits for larger samples. The comparison between Sequoia RRLs and GGCs indicates that they cover a very similar spatial distribution and iron abundances, and they possibly have a positive radial gradient ($\beta = 0.001$).

The candidate Helmi RRLs and GGCs (panels (g), (h), (i)) display, once again, very similar spatial distributions and iron abundances. The main difference is that GGCs associated with the Helmi stream cover a range in Z_{max} larger than field RRLs. They show a mild evidence of a positive radial gradient ($\beta = 0.001$) and the difference might be due to incompleteness in the current RRL sample.

Finally, Sgr RRLs (panels (j), (k), (l)) display, as expected, a very compact spatial distributions in R_G and in Z_{max}, while in ω they cover a wide range. This further supports the high level of collimation of this stellar streams.

The coefficients and the standard deviations of the performed logarithmic and linear fits for the four substructures are listed in Table 3.

6. Comparison with MW Metallicity Gradients

The occurrence of a halo metallicity gradient has been a controversial issue for several decades. Some pioneering works using GCs as tracers of the stellar halo have claimed both the existence of a metallicity gradient (W. E. Harris & R. Canterna 1979) as well as the lack of it (see e.g., L. Searle & R. Zinn 1978; T. E. Armandroff et al. 1992; E. J. Alfaro et al. 1993, and references therein). The possible occurrence of an iron gradient was also investigated by D. Butler et al. (1982), A. Saha & J. B. Oke (1984), and A. Saha (1985), by using samples of field RRLs covering $R_G = 10$–40 kpc. In these pioneering investigations they did not find evidence of a gradient with the Galactocentric distance and the distance from

Table 3

Radial Iron Gradients for Substructures by Using Either Logarithmic ([Fe/H] = α +) or Linear ([Fe/H] = $\alpha + \beta \times$ dis) Distances (kpc), where the Distance is Either the Galactocentric Distance (R_G), or the Distance Projected onto the Galactic Plane (ω), or Z_{max} or the Height Above the Galactic Plane (Z) in Absolute Value

Dis.	GSE		Sequoia		SGR		Helmi	
Logarithmic								
R_G	-1.374 ± 0.038	$-0.087 \pm 0.030(0.31)$[a]	-1.705 ± 0.071	$0.066 \pm 0.060(0.32)$	0.055 ± 0.408	$-1.002 \pm 0.270(0.42)$	-1.775 ± 0.124	$0.097 \pm 0.093(0.37)$
ω	-1.476 ± 0.028	$-0.006 \pm 0.026(0.31)$	-1.700 ± 0.070	$0.064 \pm 0.062(0.32)$	-1.334 ± 0.120	$-0.112 \pm 0.110(0.42)$	-1.662 ± 0.105	$0.013 \pm 0.092(0.37)$
Z_{max}	-1.418 ± 0.023	$-0.054 \pm 0.019(0.31)$	-1.697 ± 0.037	$0.072 \pm 0.036(0.32)$	-1.199 ± 0.168	$-0.161 \pm 0.105(0.42)$	-1.625 ± 0.134	$-0.016 \pm 0.097(0.37)$
$\|Z\|$	-1.474 ± 0.014	$-0.009 \pm 0.014(0.31)$	-1.669 ± 0.026	$0.060 \pm 0.032(0.32)$	-0.556 ± 0.287	$-0.619 \pm 0.197(0.42)$	-1.712 ± 0.059	$0.059 \pm 0.050(0.37)$
Linear								
R_G	-1.413 ± 0.014	$-0.004 \pm 0.001(0.31)$	-1.651 ± 0.029	$0.001 \pm 0.001(0.32)$	-0.981 ± 0.123	$-0.015 \pm 0.004(0.42)$	-1.680 ± 0.048	$0.001 \pm 0.002(0.37)$
ω	-1.457 ± 0.014	$-0.002 \pm 0.001(0.31)$	-1.657 ± 0.029	$0.002 \pm 0.002(0.32)$	-1.413 ± 0.053	$-0.003 \pm 0.004(0.42)$	-1.637 ± 0.043	$-0.001 \pm 0.003(0.37)$
Z_{max}	-1.419 ± 0.011	$-0.003 \pm 0.001(0.31)$	-1.639 ± 0.022	$0.001 \pm 0.001(0.32)$	-1.453 ± 0.022	$-0.000 \pm 0.001(0.42)$	-1.645 ± 0.041	$-0.000 \pm 0.001(0.37)$
$\|Z\|$	-1.443 ± 0.010	$-0.003 \pm 0.001(0.31)$	-1.635 ± 0.023	$0.001 \pm 0.002(0.32)$	-1.133 ± 0.096	$-0.011 \pm 0.003(0.42)$	-1.692 ± 0.041	$0.003 \pm 0.002(0.37)$

Note.

[a] The numbers in parentheses are the standard deviations (dex).

the Galactic plane, but a very large spread in iron abundance ranging from [Fe/H] = −1.0 to [Fe/H] = −2.2. In particular A. Saha & J. B. Oke (1984) and A. Saha (1985) brought forward, for the first time, the possible occurrence of moderately metal-rich ([Fe/H] ∼ −0.5) RRLs in the halo. Indeed, the estimate and the comparison of different radial gradients are typically affected by three main drawbacks: the spatial distribution, the accuracy of individual distances, and the homogeneity of the adopted stellar tracer.

D. Carollo et al. (2007) and D. Carollo et al. (2010) used orbital properties of local halo stars from SDSS data to measure the metallicity and inferred from this sample the metallicity of the outer halo. They claimed that the MW halo has a strong negative metallicity gradient, with the median metallicity changing from ∼−1.6 in the Solar neighborhood to −2.2 for Galactocentric distances larger than 15 kpc. However, these results suffer from important biases. Their magnitude limited sample includes only luminous low metallicity stars at large distances, imposing an artificial metallicity gradient (R. Schönrich et al. 2011). This emphasizes the need for more representative samples of distant halo stars, a requirement that only recently has been met. The duality of the Galactic halo was also supported by J. T. A. de Jong et al. (2010) by using metallicity distribution function based on photometric indices. They found evidence of a radial metallicity gradient in the MW stellar halo with a mean metallicity of [Fe/H] ∼ −1.6 for $R \lesssim 15$ kpc and a mean metallicity of [Fe/H] ∼ −2.2 at larger distances. B. Sesar et al. (2011a) used near-turnoff main sequence stars out to 35 kpc from CFHT and SDSS photometry together with photometric metallicities based on the u band (Ž. Ivezić et al. 2008) and they did not find a metallicity gradient. Subsequently, X.-X. Xue et al. (2015) used a sample of SEGUE K-giants halo stars covering a range in Galactocentric distances between 10 to 50 kpc together with LR spectra collected by SDSS and they found a weak metallicity gradient between the more metal-poor and the more metal-rich subsamples.

Data plotted in the top panel of Figure 20 show that there is a global agreement between the current RRL sample and the estimates provided by both B. Sesar et al. (2011a) and X.-X. Xue et al. (2015). A more quantitative comparison is hampered by the lack of accurate individual distances of their targets.

The halo gradient has also been investigated by the Gaia collaboration (Gaia Collaboration et al. 2023a) using nearby stars with accurate estimates of kinematic properties, distances, and iron abundances based on MR spectra. They found well-defined metallicity gradients that changed from a positive to a negative slope when moving from small to large above the Galactic plane. The solid black lines plotted in the top panel of Figure 20 show that these gradients mainly trace the increase in the spread in iron abundance across the solar circle.

E. Fernández-Alvar et al. (2017) performed a detailed analysis of chemical trends in the Galactic halo using field RGs and abundances based on HR H-band spectra provided by APOGEE. They found a dichotomic distribution in iron abundance peaking at [M/H] ∼ −1.5 and ∼−2.1. However, they did not find evidence of a radial gradient. Furthermore, C. Conroy et al. (2019a) used HR optical spectra (H3 survey) for a very large sample of field RG stars (∼4200) to constrain the metallicity distribution function of the halo. They found that the MW stellar halo is relatively metal rich ([Fe/H] = −1.2) and at the same time they did not find evidence of a metallicity gradient for Galactocentric distances ranging from ∼6 up to ∼80 kpc. Data plotted in the top panel of Figure 20, shows that their estimates cover the upper envelope of the iron gradient based on RRLs. However, they found evidence of a complex metallicity distribution with well-defined metal-rich and metal-poor components located at Galactocentric distances smaller than 10 kpc and larger than 30 kpc. The former preliminary evidence is fully supported by the current RRL sample. Moreover, they found, in fair agreement with the current analysis, that the very metal-poor ([Fe/H] ⩽ −2) halo component is a minority fraction.

Even more recently, G. E. Medina et al. (2025a, 2025b) using a large and homogeneous spectroscopic dataset based on LR spectra collected by DESI found that the inner halo ($R_G \lesssim 50$ kpc) is mainly dominated by RRLs with [Fe/H] = −1.5 associated with the GSE merger event. Moreover, they also found that, once the GSE RRLs are removed, the dry halo displays a well-defined radial gradient that appears to be slightly steeper than the current one.

The bottom panel of Figure 20 shows the [α/Fe] radial gradient. The range in Galactocentric distances covered by this sample is significantly smaller when compared with the iron radial gradient, since the measurement of α-element abundances requires HR spectra. Data plotted in this panel display that [α/Fe] abundances cover almost 0.8 dex across the solar circle, since they range from very α enhanced ([α/Fe] ∼ 0.4) to very α depleted ([α/Fe] ∼ −0.2/−0.3). The [α/Fe] abundances attain an almost constant value for Galactocentric distances ranging from ∼10 to ∼25 kpc, thus suggesting a steady decrease in the α-enhancement when moving toward larger radial distances. This negative trend is soundly supported by the radial gradient in α elements provided by E. Fernández-Alvar et al. (2017) by using APOGEE spectra. The main difference is that dry halo RRLs indicate, in the same range of Galactocentric distances, a shallower slope. The current sample is too limited to have more quantitative constraints on α-element abundances in the outer halo.

7. Comparison with Metallicity Gradients in M31

M31 is the external galaxy with the most detailed abundance analysis of its different components. Dating back to more than half century ago, the metallicity distribution of both the halo and the disks in M31 has been investigated by using photometric indices and spectroscopy for a wide range of stellar tracers. The opportunity to use wide-field imagers and multiobject spectrographs at the 4–8 m class telescopes and space facilities gave new impetus to these investigations. In the following, we perform a detailed comparison between radial metallicity gradients in MW and M31 Galactic components and in their stellar streams.

The top left panel of Figure 21 shows the comparison between the iron radial gradient of dry Halo+Retro RRLs with similar estimates for the global M31 halo available in the literature. Data plotted in this panel show that M31 iron radial gradients based on photometric indices (dashed lines) appear to be systematically more metal rich than suggested by RRLs. The difference is mainly caused by a difference in the zero-point of the gradient. However, M31 iron gradients based on spectroscopic measurements (solid lines) agree quite well with the current global sample of RRLs. In particular, the iron gradient provided by J. L. Wojno et al. (2023) covers the upper

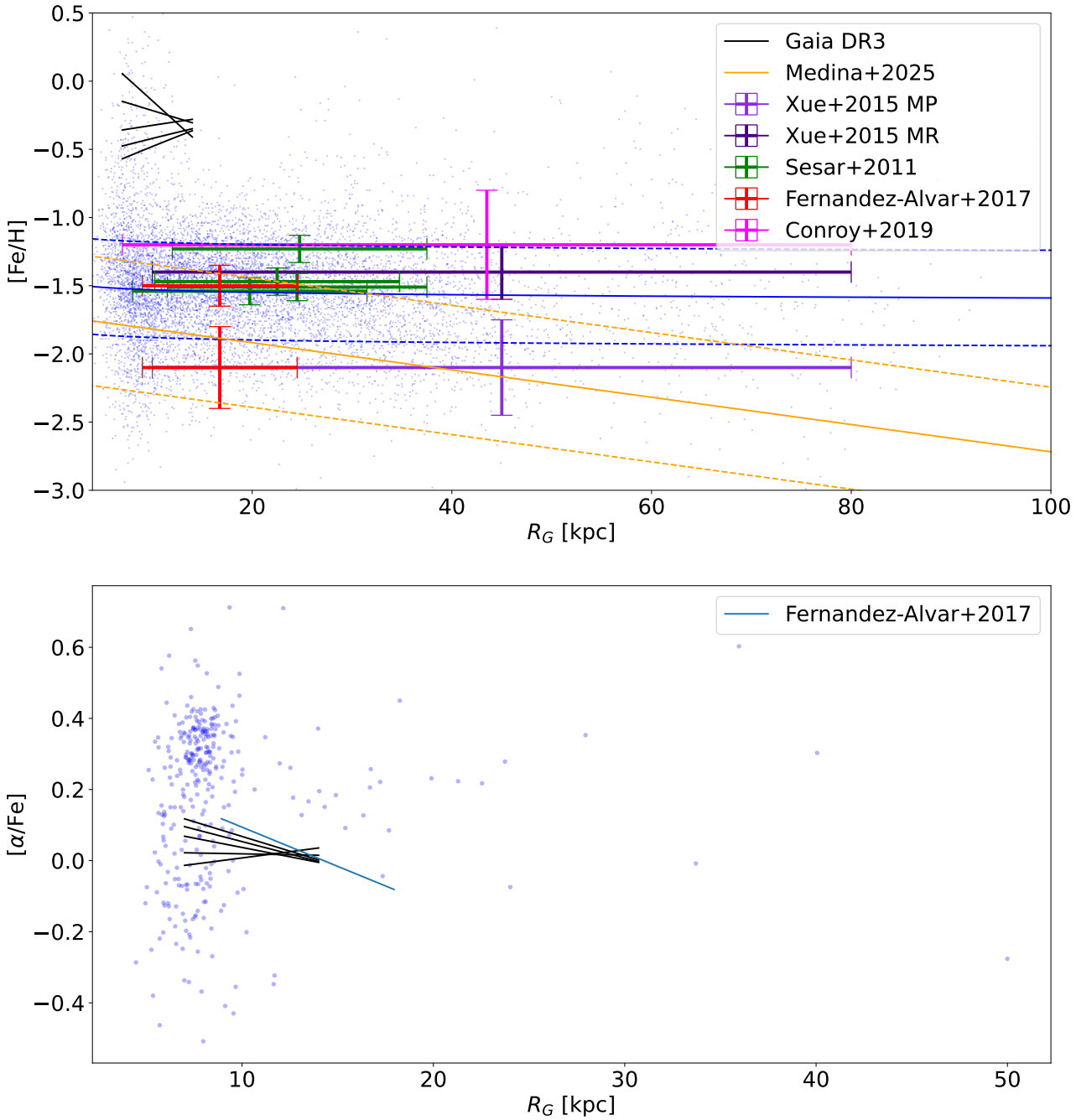

Figure 20. Top: comparison between radial iron gradients available in the literature and current Halo+Retro RRLs. The horizontal bars display the range in Galactocentric distances covered by the different estimates. The vertical bars show either the standard deviations or the mean error on iron abundance. The blue solid line shows our iron radial gradient based on linear distances, while the dashed lines display its standard deviation. The solid black lines display the iron abundance gradients at different distances (Z) above the Galactic plane provided by Gaia Collaboration et al. (2023a). Bottom: same as the top, but for the [α/Fe] radial gradient.

envelope of the distribution, but the slope is quite similar within 1σ (-0.008 versus -0.002 dex kpc^{-1}), while the spectroscopic iron gradient provided by I. Escala et al. (2020b) is even closer to metallicity distribution of the inner halo traced by RRLs.

The top right panel of Figure 21 shows the same comparison, but for the global Halo+Retro RRLs. Data plotted in this panel further support the shift in the zero-point of iron radial gradients based on photometric indexes (dashed line). The agreement with M31 spectroscopic iron gradient provided by J. L. Wojno et al. (2023) is even better since they overlap, within the errors, on a wide range of galactocentric distances. The same agreement applies to the iron abundances measured by L. C. Vargas et al. (2014) for four field RGs in the M31 halo by using LR Keck/DEIMOS spectra.

The bottom panels of the same figure display the comparison between M31 and MW halos for the [α/Fe] radial gradients. Data plotted in these panels show that there is evidence of a difference in the zero-point of 0.2 dex with the radial gradient provided by I. Escala et al. (2020a). There is also a reasonable agreement between the [α/Fe] radial gradient provided by J. L. Wojno et al. (2023) and current

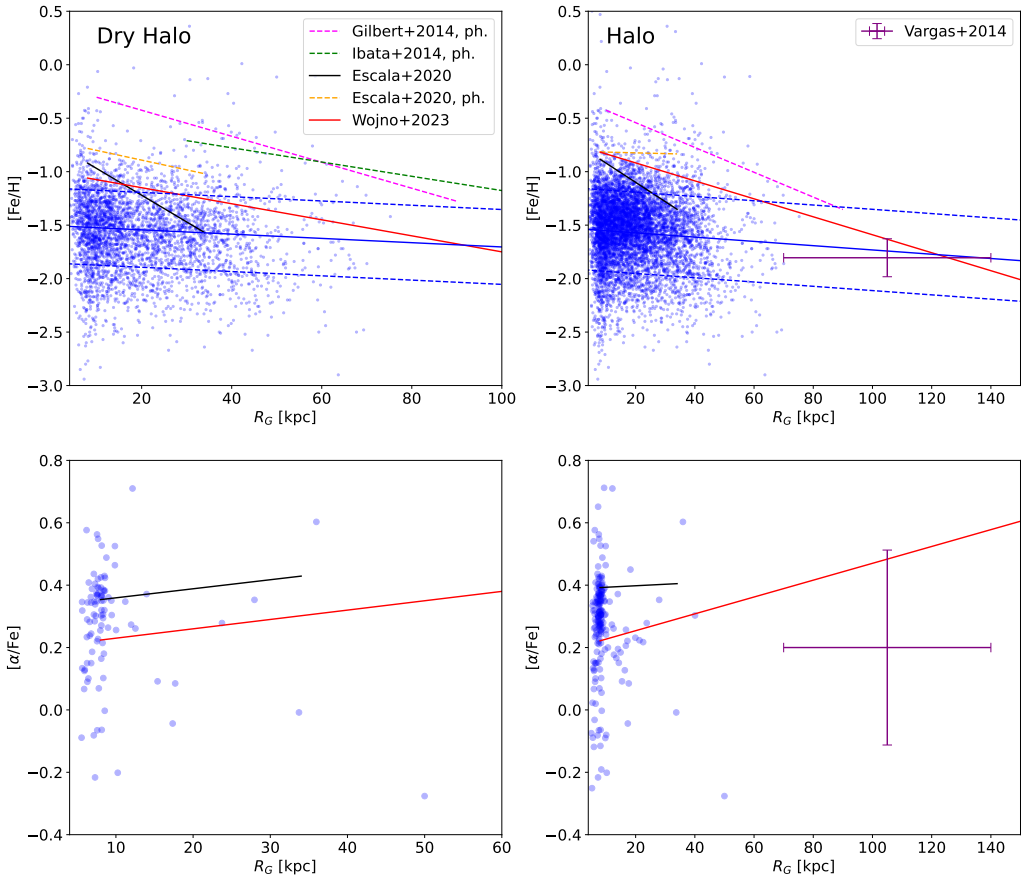

Figure 21. Top: iron abundance as a function of the galactocentric distance (linear scale). The blue dots display the distribution of MW RRLs associated with the dry halo (left) and to the global halo (right). The blue solid lines show the linear gradient for the same samples and the blue dotted lines their standard deviations (see Section 5.1). Iron gradients for M31 based either on photometric indexes (dashed) or on spectroscopic (solid) measurements are plotted with different colors (see labels). Bottom: same as the top but for the [α/Fe] gradients. See text for more details.

[α/Fe] abundances. The M31 radial gradient measured by J. L. Wojno et al. (2023) is positive and suggests a steady increase in α enhancement in the outer halo. On the other hand, the mean [α/Fe] abundance for the four RGs provided by L. C. Vargas et al. (2014) indicates, within the errors, a modest α-enhancement in the outer halo. For the sake of clearness, in Table 4 we have summarized the metallicity radial gradients for M31 and its substructures, from both spectroscopic and photometric investigations, available in the literature.

This global agreement between M31 and MW halos comes as a surprise, since current empirical and theoretical investigations indicate that M31 is significantly more massive than the MW. Moreover, there is evidence that the assembly history of M31 has been mainly driven by several events of major mergings, while for the MW it has been suggested that there was a single event of major merging plus a number of minor mergings (G. Fiorentino et al. 2017). Finally, it is worth mentioning that spectroscopic abundances for M31 halo are based on field RGs. These stars cover a broad range in stellar ages, but the agreement in the radial iron gradients further supports the evidence that M31 and MW halos are dominated by old stellar populations that experienced similar chemical enrichment.

To further constrain the similarity between the iron radial gradients of MW and M31 halos we took advantage of the sample of M31 GCs, for which both accurate spectroscopic abundances of iron and α elements (N. Caldwell et al. 2011; J. E. Colucci et al. 2014; C. M. Sakari et al. 2015, 2021; C. M. Sakari & G. Wallerstein 2022), based on HR integrated-light spectra, and homogeneous individual projected distances (J. E. Colucci et al. 2014; N. Caldwell & A. J. Romanowsky 2016; A. D. Mackey et al. 2019; C. M. Sakari et al. 2021) are available. The quoted parameters of the entire sample are listed in Table 5.

To make a more quantitative comparison with halo RRLs, we performed an analytical fit by using both linear and logarithmic distances on M31 GCs. The coefficients of the fits are listed in Table 6. The top panel of Figure 22 shows a remarkable agreement between the iron gradient traced by M31 GCs and halo RRLs. Moreover, and even more importantly, the good agreement applies not only to the innermost regions in which the two samples display a similar spread in iron abundance but also over the entire range of galactocentric distances covered by the two samples. The agreement is fully supported by the [α/Fe] radial gradient plotted in the bottom panel of the same figure in which the two samples attain, within the errors, very similar values.

The identification and characterization of substructures in M31 have been lively discussed in several empirical (T. M. Brown et al. 2006, 2009, and references therein) and theoretical (J. S. Bullock & K. V. Johnston 2005; P. B. Tissera et al. 2014; A. Monachesi et al. 2019, and references therein) papers. Here, we took advantage of the long-term project SPLASH to compare on a more quantitative basis the abundance gradients in the two largest stellar streams

Table 4
Metallicity Gradients and Metallicity Estimates for M31 and Its Substructures

Gal. Comp.	Range[a]	α	β	α	β	Tracer	References[b]
		[Fe/H]		[α/Fe]			
Spectroscopy: Halo							
Dry halo[c]	17	−0.94 ± 0.43	…	…	…	RGs	1
Dry halo	12	−1.30 ± 0.11	…	0.45 ± 0.13	…	RGs	2
Dry halo	17	−1.04 ± 0.09	…	0.53 ± 0.07	…	RGs	3
Dry halo	18	−1.00 ± 0.06	…	0.40 ± 0.04	…	RGs	3
Dry halo	22	−0.66 ± 0.18	…	0.49 ± 0.06	…	RGs	2
Dry halo	26	−1.00 ± 0.19	…	0.55 ± 0.13	…	RGs	2
Dry halo	33	−1.48 ± 0.13	…	0.41 ± 0.07	…	RGs	3
Dry halo	8–34	−0.72 ± 0.03	−0.025 ± 0.002	…	0.0029 ± 0.0027[d]	RGs	3
Dry halo	8–177	*−1.00 ± 0.05* [e]	−0.0075 ± 0.0012	*0.2*	0.0030 ± 0.0009	RGs	7
Halo	9	−0.93 ± 0.09	…	0.32 ± 0.08	…	RGs	3
Halo	23	−1.54 ± 0.14	…	0.43 ± 0.12	…	RGs	2
Halo	23	−1.64 ± 0.11	…	0.39 ± 0.10	…	RGs	3
Halo	31	−1.35 ± 0.10	…	0.40 ± 0.10	…	RGs	3
Halo	8–34	−0.74 ± 0.03[f]	−0.018 ± 0.001	…	0.00048 ± 0.00261	RGs	3
Halo	8–177	*−0.75 ± 0.05*	−0.0084 ± 0.0008	*0.2*	0.0027 ± 0.0005	RGs	7
Spectroscopy: Disks							
Outer disk	26	−0.82 ± 0.09	…	0.60 ± 0.10	…	RGs	2
Disk (phot)	4-20	…	−0.020 ± 0.004		…	RGs	12
Spectroscopy: Substructures							
GSS[g]	17	−0.75 ± 0.37		[h]		RGs	1
GSS	17	−0.87 ± 0.10	…	0.44 ± 0.05	…	RGs	3
GSS	22	−1.02 ± 0.15	…	0.38 ± 0.19	…	RGs	2,3
GSS	33	−1.11 ± 0.13	…	0.34 ± 0.09	…	RGs	3
KCC[i]	17	−0.61 ± 0.40	…	…	…	RGs	1
KCC	17	−0.79 ± 0.07	…	0.54 ± 0.06	…	RGs	3
KCC	22	−0.71 ± 0.11	…	0.35 ± 0.09	…	RGs	2,3
GSS+KCC	17-33	−0.52 ± 0.08	−0.018 ± 0.003	0.57 ± 0.17	−0.007 ± 0.007	RGs	5
GSS	17-33	−0.61 ± 0.09	−0.016 ± 0.004	0.52 ± 0.14	−0.006 ± 0.007	RGs	5
GSS+KCC	17-58	−0.96 ± 0.06	…	0.40 ± 0.05	…	RGs	5
GSS	17-58	−1.03 ± 0.07	…	0.39 ± 0.06	…	RGs	5
SES[j]	12	−1.30 ± 0.13	…	0.53 ± 0.10	…	RGs	2,3
SES	18	−0.71 ± 0.07	…	0.41 ± 0.05	…	RGs	3
SES	17-58	−0.89 ± 0.08	…	0.45 ± 0.05	…	RGs	5
Substructures	8-90	…	−0.0086 ± 0.0023	…	0.0011 ± 0.0021	RGs	7
Photometry: Halo							
Dry halo	8-34	−0.81 ± 0.03	−0.00070 ± 0.0016	…	…	RGs	3
Dry halo	10-90	−0.75 ± 0.03	−0.0105 ± 0.0013	…	…	RGs	4
Halo	8-34	−0.71 ± 0.04	−0.0091 ± 0.0019	…	…	RGs	3
Halo	10-90	−0.31	−0.0110 ± 0.0007	…	…	RGs	4
Photometry: Substructures							
NES[k]	15-29	−0.53 ± 0.02	…	…	…	RGs	6
GSS	17-69	−0.56 ± 0.02	…	…	…	RGs	9,6
WS[l]	10-30	−0.67 ± 0.03	…	…	…	RGs	10,6
SES	9-30	−0.50 ± 0.02	…	…	…	RGs	11,6

Notes. They have been estimated through a linear analytical fit [Fe/H] = $\alpha + \beta \times$ dis, where the dis (kpc) is the projected distance.
[a] Range in projected distance (kpc).
[b] References: (1) K. M. Gilbert et al. (2019), (2) I. Escala et al. (2020a), (3) I. Escala et al. (2020b), (4) K. M. Gilbert et al. (2014), (5) I. Escala et al. (2021), (6) I. Escala et al. (2022), (7) J. L. Wojno et al. (2023), (8) C. M. Sakari & G. Wallerstein (2022), (9) K. M. Gilbert et al. (2009), (10) M. A. Fardal et al. (2012), (11) K. M. Gilbert et al. (2007), (12) D. Gregersen et al. (2015).
[c] Halo neglecting substructures.
[d] Not statistically significant.
[e] The values highlighted in italics were calculated by using the slope, the [Fe/H] and/or the [α/Fe] at other distances from the reference.
[f] Intercept at $r_{proj} = 0$ kpc.
[g] Giant Stellar Stream.
[h] α enhanced for [Fe/H] $\leqslant -0.9$, decreasing α enhancement with increasing iron.
[i] Kinematically cold component.
[j] Southeast shelf.
[k] Northeast shelf.
[l] West shelf.

Table 5
Iron, α Elements Abundances and Projected Distances of the M31 GCs[a]

Name	R.A. (J2000)	Decl.	R_{pro} (kpc)	[Fe/H]	[α/Fe][b]	Ref.[c]
			Inner halo GCs			
B006-G058	00:40:26.48	41:27:26.7	6.39	-0.73 ± 0.22	0.29 ± 0.03	1
B012-G064	00:40:32.46	41:21:44.2	5.74	-1.61 ± 0.21	0.27 ± 0.17	1
B029-G090	00:41:17.82	41:00:23.0	6.78	-0.43 ± 0.11	0.21 ± 0.13	1
B034-G096	00:41:28.12	40:53:49.6	6.02	-0.75 ± 0.14	0.24 ± 0.06	1
B045-G108	00:41:43.11	41:34:20.3	4.90	-0.94 ± 0.22	0.21 ± 0.11	1
			Outer halo GCs			
G001	00:32:46.50	39:34:40.6	34.70	-0.98 ± 0.05	0.34 ± 0.05	4
G002	00:33:33.80	39:31:18.5	33.62	-1.63 ± 0.16	-0.15 ± 0.19	1
B514-MCGC4	00:31:09.85	37:54:00.4	55.30	-1.74 ± 0.17	0.22 ± 0.23	1
MCGC5-H10	00:35:59.76	35:41:03.9	78.68	-1.45 ± 0.10	0.14 ± 0.13	1
MGC1	00:50:42.50	32:54:59.6	117.00	-1.56 ± 0.09	0.14 ± 0.04	1

Notes.
[a] Table 5 is published in its entirety in machine-readable format. A portion is shown here for guidance regarding its form and content.
[b] α-element abundances were derived by averaging (in logarithmic scale) the Ca, Mg, and TiII abundances found in the literature.
[c] References: (1) J. E. Colucci et al. (2014), (2) N. Caldwell et al. (2011), (3) N. Caldwell & A. J. Romanowsky (2016), (4) C. M. Sakari et al. (2021), (5) C. M. Sakari & G. Wallerstein (2022), (6) A. D. Mackey et al. (2019), (7) C. M. Sakari et al. (2015).
(This table is available in its entirety in machine-readable form in the online article.)

Table 6
Radial Iron and α-element Gradients in R_G for the GCs in M31 by Using Either A Logarithmic ([Fe/H] = $\alpha + \beta \times$ log(dis)) or a Linear ([Fe/H] = $\alpha + \beta \times$ dis) Fit

Gradient	Inner GCs		Outer GCs		Global	
			Logarithmic			
[Fe/H]	-0.742 ± 0.059	-0.446 ± 0.084 (0.57)[a]	-0.517 ± 0.154	-0.639 ± 0.108 (0.42)	-0.713 ± 0.050	-0.494 ± 0.057 (0.54)
Linear						
[Fe/H]	-0.788 ± 0.053	-0.040 ± 0.008 (0.57)	-1.090 ± 0.086	-0.008 ± 0.002 (0.46)	-0.952 ± 0.034	-0.011 ± 0.002 (0.56)
[α/Fe]	…	…	0.241 ± 0.021	-0.001 ± 0.001 (0.10)	…	…

Notes. They have been estimated by using iron and α elements abundances for M31 GCs listed in Table 5.
[a] The numbers in parentheses are the standard deviations (dex).

identified in M31 (Giant Stellar Stream, GSS) and in the MW (GSE).

Data plotted in the top panel of Figure 23 show the comparison between candidate GSE RRLs, selected according to the criteria discussed in Section 3.2, and the iron radial gradient in GSS (red line) and in GSS plus the kinematic cold component (KCC) (black line) provided by I. Escala et al. (2021) by using a large set of spectroscopic measurements. There is evidence of a difference in the zero-point of the order of 0.5 dex, but the slopes in the same range of Galactocentric distances are quite similar (-0.016 versus -0.004 dex kpc^{-1}). This global agreement also applies to the [α/Fe] radial gradient; indeed, if we account for the difference in the zero-point of the iron gradient, the radial gradients of the α elements are quite similar. In passing, we also note that the [α/Fe] radial gradients provided by I. Escala et al. (2021) indicate a decrease in the α-enhancement when moving toward the outer halo.

8. Summary and Conclusions

We introduce the largest and most homogeneous photometric catalog of RRLs (PR3C). PR3C includes more than 300,000 RRLs, among them roughly two thirds pulsate in the FU mode (RRab), one third in the FO (RRc), and $\approx$10% as mixed-mode RRL (RRd). PR3C includes both field RRLs and RRLs associated with stellar systems (GCs, dwarf galaxies). The catalog is mainly based on data available in public datasets. PR3C provides astrometric parameters, pulsation parameters (period, pulsation mode, luminosity amplitudes), mean apparent magnitudes, and heliocentric and Galactocentric distances and reddening, together with their errors.

We also present the largest and most homogeneous spectroscopic dataset of old stellar tracers (RRLs, BHB) ever collected (SR3C). SR3C includes more than 16,000 field RRLs and for all of them we provide an RV measurement. SR3C is mainly based on LR spectra collected by public spectroscopic surveys. For 8140 of them that cover the Ca II H&K lines, we provide an estimate of the iron abundance by using the ΔS method developed by C21a and F21. This sample was complemented with 547 iron abundance estimates available in the literature.

For a small fraction of field stars (487 RRLs, 64 BHB), HR spectra collected with 1 to 8 m class telescopes are also available. Our group obtained and analyzed a significant fraction of them (342). For these objects, SR3C includes individual elemental abundances for iron and α elements. They were also complemented with similar estimates available in the literature. Measurements from the literature were only included if the individual samples overlapped with our dataset and could have been moved to the same metallicity scale.

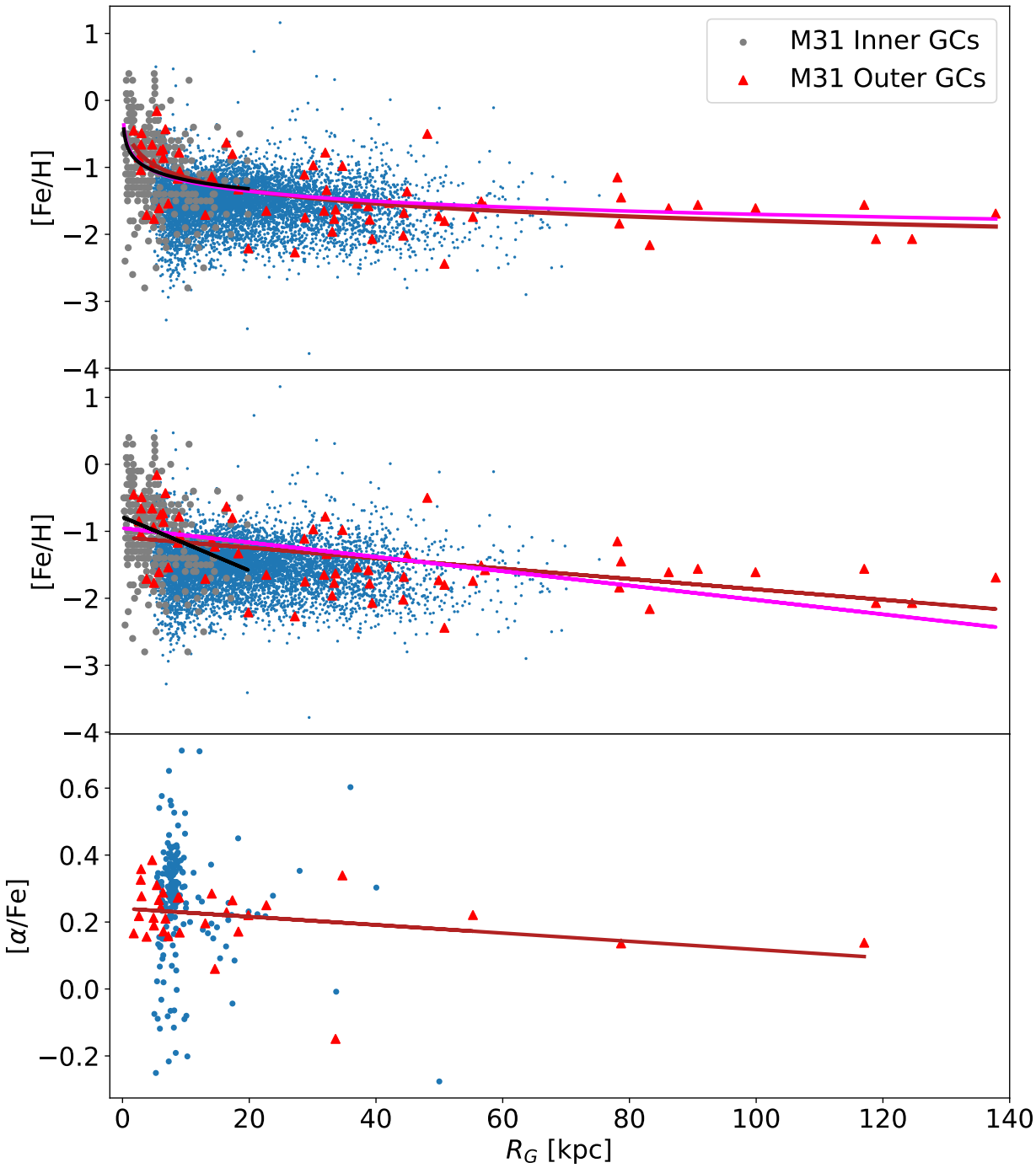

Figure 22. Top: Iron abundance versus galactocentric distances. Blue dots mark MW global Halo+Retro RRLs, while gray circles and red triangles inner and outer halo M31 GCs. (see Table 5). The black and the magenta lines display the fit of logarithmic gradients for inner and outer halo M31 GCs, while the brown line the fit for the global sample. Middle: Same as the top, but for the linear fits. Bottom: Same as the top, but for the [α/Fe] linear gradients. See text for more details.

SR3C also includes astrometric and kinematic parameters (position, proper motion) based on Gaia DR3.

The main results of the current investigation follow.

The probabilistic criteria suggested by T. Bensby et al. (2014) were adopted to select the RRLs associated either with the main Galactic components—halo, TND, and TCD—or in retrograde orbits. To validate the quoted selections, we also adopted the more stringent criteria suggested by E. Fernández-Alvar et al. (2024) for the identification of TND stars.

By using two different diagnostics—the Lindblad diagram and the circularity of the orbits as a function of the Galactocentric distance—we found that field RRLs display a systematic drift from the more metal-poor halo to the more metal-rich component of the TND. The RRLs associated with the TCD trace quite well the transition between the more metal-poor and the more metal-rich regimes, since several of them have solar iron abundance.

The peak in the IDF becomes systematically more metal rich when moving from the halo ([Fe/H] $= -1.56$) to the TCD ([Fe/H] $= -1.47$) and to the TND ([Fe/H] $= -0.73$). Moreover, the IDF becomes broader and the standard deviation increases by about 50% between the halo and the

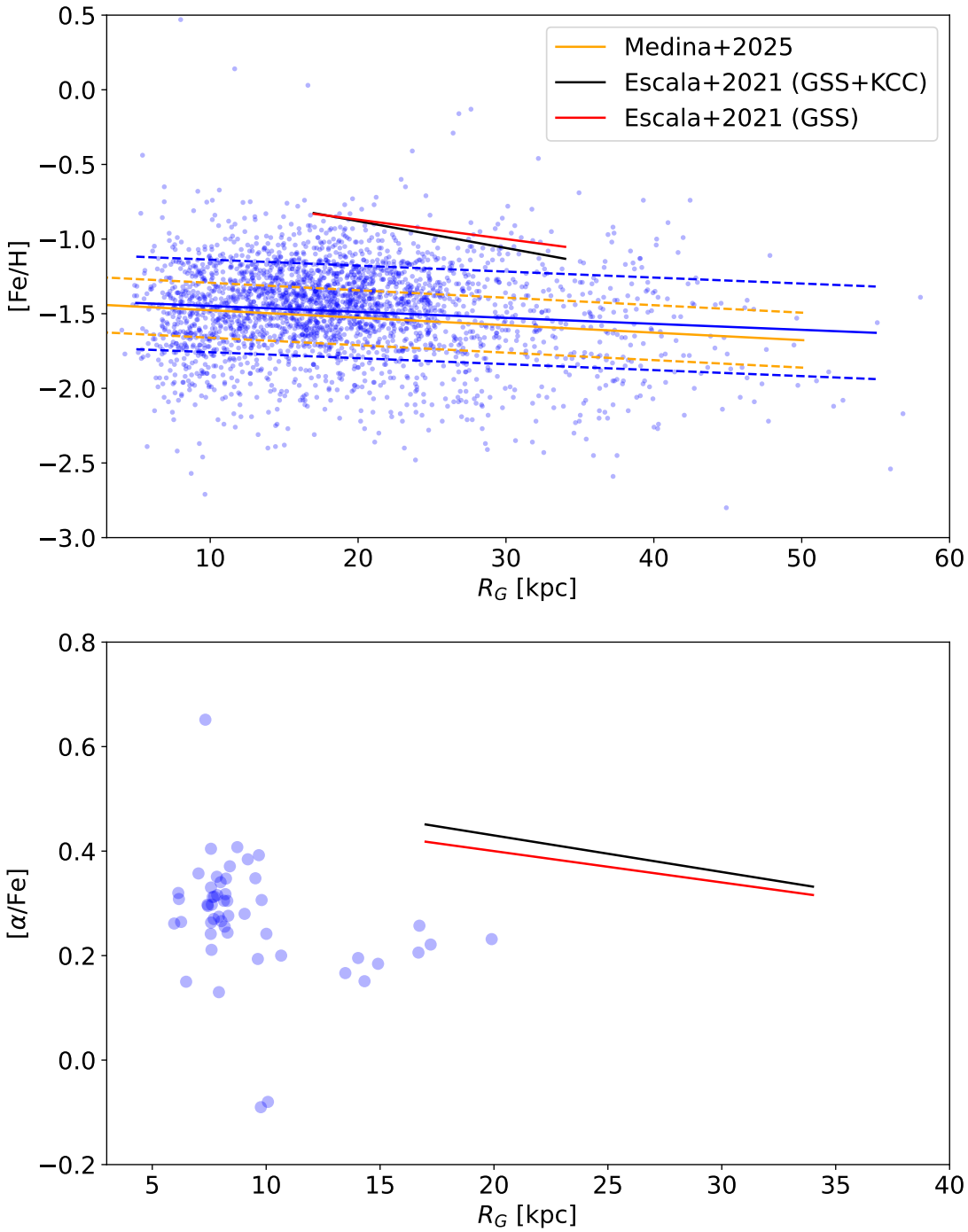

Figure 23. Top: iron versus galactocentric distance (linear scale). Blue dots display candidate GSE RRLs, while the blue solid line shows the linear fit of the iron radial gradient and the dashed lines its standard deviation. The red solid line shows the linear iron radial gradient for the GSS in M31, while the black line the same gradient but for stars in GSS plus the KCC provided by I. Escala et al. (2021). The yellow lines display the radial gradient (solid) for GSE RRLs provided by G. E. Medina et al. (2025a) together with its standard deviation (dashed lines). Bottom: same as the top, but for the [α/Fe] gradient.

TND (0.37 versus 0.57). RRLs in retrograde orbits are similar to halo RRLs, since they show similar Galactocentric distances, similar peaks in the IDF, and similar standard deviations.

The separation among the different Galactic components is also supported by [α/Fe] abundances. Halo RRLs are α enhanced, since their abundance ratio is [α/Fe] = 0.27 ($\sigma = 0.18$). The TCD RRLs are either α enhanced ([Fe/H] $\leqslant -1.0$) or α poor/α depleted in the more iron-rich regime, while TND RRLs are mainly α poor/α depleted with [α/Fe] = -0.01 ($\sigma = 0.20$). RRLs in retrograde orbits appear to be quite similar to halo RRLs, since they show similar α-element distributions.

To validate the selection criteria adopted to identify the different Galactic components we adopted the dynamical planes suggested by J. M. M. Lane et al. (2022) together with three additional kinematic planes showing the circularity of the orbits (λ_Z) as a function of eccentricity, the maximum height above the Galactic plane (Z_{max}), and the Galactocentric distance. Candidate TND and TCD RRLs can be easily identified in the

Toomre diagram, since they cluster around $V_T \approx 250\,\mathrm{km\,s^{-1}}$ and $V_T \approx 150\,\mathrm{km\,s^{-1}}$, respectively. The same outcome applies for candidate halo RRLs and RRLs in retrograde orbits, since they attain either vanishing or negative transversal velocities. The same outcome applies to the V_R versus V_T plane and to the Lindblad diagram. Special attention was paid to characterize RRLs with hot orbits (halo versus bulge). To identify bulge RRLs we selected RRLs that, along their orbits, have an apocentric radius smaller than $r_{\rm ap} \leqslant 3.5$ kpc. Bulge RRLs can easily be identified in the Lindblad diagram, since they are characterized by very low orbital energies and vanishing vertical angular momentum, and in the $\sqrt{J_R}$ versus L_Z plane due to their very low values of the square root of the radial action. We found, as expected, that only five RRLs in our sample are candidate bulge RRLs. Candidate TND RRLs can also be easily identified as they cluster in the right corner of the action diamond, since their action budget is dominated by L_Z. Moreover, they cover a very tiny and compact slice in the Lindblad diagram, together with large circularities, small eccentricities, and small $Z_{\rm max}$ values. Candidate TCD RRLs display a smooth transition between TND and halo RRLs in the different kinematic planes.

Interestingly enough, we also found evidence that the distribution of halo RRLs in the circularity of the orbits versus $Z_{\rm max}$ plane is far from being homogeneous. They display four distinct stellar arcs that move from TCD RRLs ($\lambda_Z > 0.25$) to RRLs with retrograde orbits ($\lambda_Z < -0.25$). Moving from larger to smaller $Z_{\rm max}$ distances, they are located at $Z_{\rm max}\sim$ 30–40 kpc, 10–20 kpc, 7–9 kpc, and 4–5 kpc. This is new evidence driven by the accuracy of the individual RRL distances, suggesting that RRL radial distribution might be affected either by early merging events or by peculiar radial motions. Moreover, the lack of these features in the circularity versus Galactocentric distance plane indicates that these stellar arcs appear to have radial distributions perpendicular to the Galactic plane.

We also performed a chemo-dynamical investigation of the substructures in the MW. To identify candidate GSE and Sequoia RRLs we adopted the same selection criteria suggested by D. K. Feuillet et al. (2021), while for RRLs in the SGR stream we followed the selections from T. Antoja et al. (2020) and for RRLs in the Helmi stream the kinematic criteria recently provided by H. H. Koppelman et al. (2019) and D. Horta et al. (2023).

Candidate GSE RRLs can be easily identified, since they cluster not only in the Toomre and in the Lindblad diagram but also in the action-diamond plane. Moreover, the compact distribution that GSE RRLs show in the circularity versus $Z_{\rm max}$ plane further supports the evidence that they originated from a single major merging event. Furthermore, GSE RRLs peak, in the square root of the radial action versus the vertical angular momentum, at radial action values that are systematically larger than halo RRLs. The chemical characterization, the IDF, and the standard deviations of GSE RRLs are, within the errors, quite similar to halo RRLs. However, GSE RRLs lack the metal-poor/metal-rich tails, and their α-element distribution is quite compact. They are metal intermediate and show a homogeneous chemical enrichment not only in the range of energies covered in the Lindblad diagram but also in the wide range of Galactocentric distances they are covering (5–50 kpc).

Candidate Seq RRLs cluster in the left corner of the action diamond. However, the Sequoia sample clearly splits into two different subgroups in the Lindblad diagram, in the eccentricity versus L_Z plane, and in the $\sqrt{J_R}$ versus L_Z plane. Sequoia RRLs display a well-defined minimum for $R_{\rm G} \sim 12$ kpc in the circularity versus Galactocentric. This evidence was adopted to split the Sequoia candidate into Section 1 and Section 2 RRLs. The IDFs of Section 1 and Section 2 RRLs peak at $[\mathrm{Fe/H}] = -1.68$ and -1.60, and they are also similar to halo RRLs, but their standard deviation is smaller (0.31 versus 0.37).

Candidate Helmi RRLs show a smooth distribution in the Toomre diagram and in the action diamond, but they show a well-defined concentration in the Lindblad plane across $E \sim -1.0 \cdot 10^5\,\mathrm{km^2\,s^{-2}}$, $L_Z \sim 1.0 \cdot 10^3\,\mathrm{kpc\,km\,s^{-1}}$ and a high-energy tail extending from $E \sim -0.9 \cdot 10^5\,\mathrm{km^2\,s^{-2}}$. Data plotted in the λ_Z versus $Z_{\rm max}$ plane indicate that candidate Helmi RRLs are mainly located in the TCD, since $Z_{\rm max}$ ranges from a few kpc to ∼20 kpc and λ_Z between 0.7 and 0.2. The IDF of Helmi RRLs peaks at $[\mathrm{Fe/H}] = -1.64$, and it is once again similar to halo RRLs (−1.56), with similar standard deviations (0.36 versus 0.37).

Candidate SGR RRLs typically have a sparse distribution in the classical kinematic planes, but they are relatively concentrated in the circularity versus $Z_{\rm max}$ plane and in the circularity versus $R_{\rm G}$ plane. In particular, they cover a narrow range in Galactocentric distances ($R_{\rm G} \sim$ 30–40 kpc) and in maximum height above the Galactic plane ($Z_{\rm max}\sim$ 20–30 kpc). This finding further supports the evidence that SGR candidates in the current catalog are mainly associated with the SGR stream, with a minimal contribution from the SGR core. The SGR RRLs display an IDF similar to halo RRLs, with marginal evidence for a metal-poor/metal-rich tail. They are located at large Galactocentric distances and we still lack measurements of their α-element abundances.

The circularity versus $Z_{\rm max}$ plane is a very interesting diagnostic to investigate the spatial distribution of stellar streams. Indeed, Section 1 and Section 2 RRLs have retrograde orbits and display in this plane and a well-defined separation also in $Z_{\rm max}$. In particular, the RRLs in Section 2 attain maximum heights above the Galactic plane that are larger than 9–10 kpc, while RRLs in Section 1 are located closer to the Galactic plane. Moreover, we found that in this plane candidate Sequoia, Helmi, and SGR RRLs appear to be associated with the stellar arcs previously identified in the different Galactic components. SGR RRLs are associated with the stellar arc located at larger Galactocentric distances ($Z_{\rm max}\sim$ 30–40 kpc), Helmi and RRLs in Section 2 are associated with the stellar arc located at $Z_{\rm max}\sim$ 10–20 kpc, while RRLs in Section 1 are associated with the stellar arcs located at 7–9 kpc, and 4–5 kpc. The main difference is that candidate Sequoia RRLs are in retrograde motion, while Helmi RRLs are in prograde motion.

Furthermore, we performed a detailed comparison between the chemo-dynamical properties of old stellar tracers such as RRLs with similar properties for GGCs. The GGC kinematics were estimated by using proper motions and distances provided by H. Baumgardt et al. (2019), together with the same Galactic potential adopted for field RRLs. The association with the different Galactic components was performed by using the same criteria adopted for field RRLs, while for the association of individual GGCs with the different stellar streams we took advantage of the chemo-dynamical investigation recently provided by D. Massari (2025). We found a

global agreement among the different stellar streams and the associated GGCs. However, there is mounting evidence of several outliers, i.e., GGCs that in different kinematic planes do not cluster with the bulk of the candidate RRLs. This preliminary finding supports predictions based on numerical simulations by G. Pagnini et al. (2023), suggesting the possible lack of dynamical coherence.

During the last few years, several theoretical and empirical investigations have been focused on the occurrence of radial metallicity gradients. The radial metallicity gradient is a solid diagnostic to constrain the mass assembly and the chemical enrichment histories of the different Galactic components. We found that TCD RRLs display a well-defined radial iron gradient. The iron gradient is as expected negative and the slope in R_G and in ω (-0.010) is steeper than in $Z_{\rm max}$. The iron abundance changes from metal intermediate ([Fe/H] ~ -1) in the innermost TCD regions to metal poor ([Fe/H] ~ -2) in the outermost TCD regions. There is evidence of a steepening in the iron gradient for $R_{\rm G}$ and $\omega \leqslant 10$ kpc, and this transition occurs across the solar circle.

TND RRLs also display a well-defined radial iron gradient; in particular, as a function of $Z_{\rm max}$. The change in the slope across the solar circle was neglected, since it is mainly driven by the increased dispersion in metallicity. This finding indicates that the inside-out scenario for the chemical enrichment of the TND was already in place in the early phase of the MW formation. Moreover, the iron gradients associated with TND RRLs typically cover a narrower range in distances, but they are steeper when compared with the iron gradients of TCD RRLs (-0.026 versus -0.010).

Global halo RRLs present a very mild radial gradient and a large spread in iron abundance over a significant fraction of Galactocentric distances. The slopes of the iron gradients are, on average, more than one order of magnitude shallower than TND RRLs (-0.002 versus -0.026 dex kpc^{-1}), and a factor of five shallower than TCD RRLs (-0.002 versus -0.010 dex kpc^{-1}). The iron abundances of the RRLs with retrograde orbits display similar radial trends. The mean iron abundance increases by more than 0.3 dex between $R_{\rm G} \sim 10$ kpc and $R_{\rm G} \sim 7$ kpc. This evidence supports previous findings by N. B. Suntzeff et al. (1994) and A. C. Layden (1995), and more recently by T. D. Kinman et al. (2012).

To constrain on a more quantitative basis the possible impact of the stellar streams on the radial iron gradient, we performed once again the linear fits by using dry halo RRLs, i.e., the field RRLs that do not belong to the four selected stellar streams. Interestingly enough, we found that the iron gradient is, within the errors, equal to the global halo. This suggests that the inclusion of RRLs belonging to stellar streams has a minimal impact on the slope, but the standard deviations of the linear relations of the dry halo are slightly smaller (0.36 versus 0.38). Furthermore, the comparison between the iron radial gradients of the main Galactic components and GGCs associated with the same components display a global agreement. Thus, suggesting that they are conatal and they have had a common chemical enrichment history.

The possible occurrence of iron radial gradients was also investigated among the selected stellar streams. We found that candidate GSE RRLs display a very mild negative radial gradient ($\beta = -0.004$) over the entire range of Galactocentric distances covered by the current sample. Preliminary evidence indicates the occurrence of two gaps in radial distance, suggesting the possible presence of different substructures among GSE RRLs.

Sequoia RRLs display a well-defined separation in RRLs in Section 1 and in Section 2. The iron abundance is quite constant with mild evidence of a possible positive radial gradient ($\beta = 0.001$). The Helmi RRLs cover a modest range in radial distances and show tentative evidence of a positive radial gradient ($\beta = 0.001$).

As a whole, we found mild evidence of iron radial gradients among the selected stellar streams, but the analysis is partially hampered by the range in Galactocentric distances covered by the current subsamples and by the limited number of stars with spectroscopic abundances.

The comparison between current metallicity gradients based on RRLs and similar estimates available in the literature is far from being an easy effort. The reason is twofold:

(i) Literature estimates are a mixed bag, since we move from the presence of a radial gradient to the lack of a gradient according to the adopted stellar tracer, the range in Galactocentric distances covered by the different samples, and the kinematic selection of the different Galactic components. More recently, estimates based on large spectroscopic samples of field stars brought forward evidence of duality in the halo metallicity distribution. The inner halo being at least half dex more metal rich than the outer halo (D. Carollo et al. 2007, 2010; J. T. A. de Jong et al. 2010; B. Sesar et al. 2011a; X.-X. Xue et al. 2015).

(ii) The homogeneity and the accuracy of individual iron abundances and distances affect the estimate of the radial gradients.

The comparison between the current and literature estimates shows, within the errors, a global agreement over the range in Galactocentric distances covered by the different estimates. The agreement with recent estimates based on APOGEE measurements (E. Fernández-Alvar et al. 2017) is quite good not only for the iron radial gradients but also for the [α/Fe] radial gradients. However, this sample only covers a modest range in Galactocentric distances. We also found a reasonable agreement with the radial gradient for the MW dry halo recently derived by G. E. Medina et al. (2025a, 2025b) using a large and homogeneous sample of LR spectra collected by DESI. However, their slope is steeper than the current one (-0.01 versus -0.002 dex kpc^{-1}).

The unique opportunity to deal with a large and homogeneous sample of old stellar tracers opens the path for a detailed comparison between the MW radial gradients and similar estimates for M31. In particular, M31 has been the crossroads of several investigations based either on photometric indices or on spectroscopic measurements. M31 is also the only nearby galaxy for which these measurements are available not only for the main galactic components but also for its substructures. We performed a detailed comparison and we found several interesting results.

(i) The iron radial gradients for M31 based on photometric indices (R. A. Ibata et al. 2014; K. M. Gilbert et al. 2014; I. Escala et al. 2020b) have slopes that, within 1σ, agree with the current estimates based on MW field RRLs (-0.011 versus -0.002 dex kpc^{-1}). However, the zero-points are systematically more metal rich. The iron radial gradients based on spectroscopic measurements (I. Escala et al. 2020b; J. L. Wojno et al. 2023) agree quite well, within 1σ, both in

slope and zero-points, with similar estimates based on RRLs (-0.008 versus -0.002 dex kpc^{-1}). This outcome applies not only to the global halo, but also to the dry halo (-0.007 versus -0.002 dex kpc^{-1}).

(ii) The comparison with the [α/Fe] gradient (I. Escala et al. 2020a; J. L. Wojno et al. 2023) discloses a global agreement between M31 and the MW. However, the range in Galactocentric distances covered by dry halo RRLs with α abundances is too limited to assess the possible presence of a gradient, but the global halos show a good similarity over the entire range of Galactocentric distances (see Figure 21).

(iii) We made a similar comparison between the iron gradient detected by I. Escala et al. (2021) for GSS in M31 and that of GSE in the MW and found a similar slope within 1σ (-0.016 versus -0.004) and a well-defined difference in the zero-point. GSS appears systematically more metal rich and more α poor at any galactocentric distance. Interestingly enough, the slope for GSE RRLs recently derived by G. E. Medina et al. (2025a) agrees quite well with the current estimate of the GSE radial gradient (-0.005 versus -0.004).

(iv) Furthermore, we performed a detailed comparison between iron and α radial gradients of M31 GCs and field RRLs. The abundances for M31 GCs are based on integrated-light spectroscopy, and the very good agreement over the entire range in galactocentric distances covered by the two samples came as a surprise. This outcome applies to both inner and outer halo GCs and to both the iron and α radial gradients. The slopes of the iron radial gradient of the M31 GCs and field MW RRLs are in global agreement, indeed the slope for outer halo GCs is $\beta = -0.008$ and for the global sample $\beta = -0.011$. The similarity is further reinforced, but there is evidence that MW RRLs minimally include objects associated with the Galactic bulge and poorly cover the outermost halo regions. Moreover, the α-element radial gradients in M31 and in the MW indicate that the outer halo shows a smaller dispersion and more α-poor abundances when compared with inner halo objects. There is no reason why old stellar tracers in M31 and in the MW should show similar radial trends. The current findings suggest similar early enrichment histories.

One the most attractive features of HB (RRL, BHB) stars is that they are old ($t > 10$ Gyr) stellar tracers. This means that their properties can provide firm constraints concerning the early formation and evolution of the Galactic spheroid.

Detailed predictions based on HR *N*-body simulations plus semianalytical models (G. De Lucia & A. Helmi 2008) indicate that the halo should show a dichotomic metallicity distribution with no clear evidence of a metallicity gradient and a well-defined dominance of metal-rich objects. However, they also mentioned that the metallicity distribution function is strongly correlated with the total mass of the satellites that have accreted.

More detailed simulations taking account of the nucleosynthesis yields and the transition between pop III and pop II also suggest a broad metallicity distribution approaching solar metal-abundances (see Figures 3 and 6 in S. Salvadori et al. 2007). More recently, *N*-body simulations by A. Zolotov et al. (2009), A. Zolotov et al. (2010), and by A. S. Font et al. (2011, Figures 5, 6) show evidence of a metallicity gradient in the Galactic halo.

The comparison with the simulations provided by the latter group is more complex since they do not separate bulge and halo components. We performed the same comparison, but we only took into account Galactocentric distances larger than 3.5 kpc to limit the contribution of the bulge. We found that the predicted gradient is systematically more metal rich over the entire distance range (see their Figure 5). The difference might be tightly connected with the fraction of SN type Ia they adopted in their simulations (see their Figure 6).

There is also a clear difference between the inner and the outer halo. The above simulations suggest that the inner halo formed in situ and their stellar populations are typically old ($t > 13$ Gyr). On the other hand, the ages of the outer halo are systematically younger (6–8 Gyr), since these are the typical ages of the accreted satellites. However, the current empirical evidence indicates the presence of large sample of field RRLs in the outer halo.

The current findings are in global agreement with the chemical evolution models of the Galactic halo provided by G. Brusadin et al. (2013). Indeed, they found that the two–infall model, developed by C. Chiappini et al. (1997) and D. Romano et al. (2010), plus the outflow predicts a broad metallicity distribution function for the halo. A more detailed comparison between theory and observations is planned in a forthcoming investigation.

In passing, we also note that the results concerning the negative iron radial gradients and the modest variation in [α/Fe] abundance ratio agree quite well with similar findings for late type galaxies found by T. Parikh et al. (2021, and references therein), which used a large sample of stacked spectra from the SDSS-IV/MaNGA survey of galaxies covering a broad range in stellar mass.

The analysis of stellar streams and Galactic components depends on the criteria adopted to identify the different substructures. They are all affected by limitations; the main objective of this investigation was to provide a global interpretation of the current empirical evidence. There is no doubt that the improved accuracy of astrometric parameters, RVs, and distances coming with the Gaia DR4 will allow us to perform a more detailed tomography of the Galactic spheroid.

Seventy-five years after the early evidence for a revision of the cosmic distance scale brought forward by W. Baade (1963, pg. 100), based on the nondetection of cluster type variables in the field of M31 in blue and red photographic plates collected with the Palomar telescope, Galactic RRLs and M31 appear to be once again crucial to improve our knowledge of evolutionary and pulsation properties of old stellar populations and galaxy formation.

Acknowledgments

We thank, with an unusual pleasure, the anonymous referee for their positive words and warm appreciation of the entire project, and, in particular, of the current content of the paper. Moreover, we are also very grateful to the anonymous referee for their constructive and pertinent suggestions that improved its content and readability. We also thank J. Bovy for many useful discussions and suggestions concerning physical and numerical assumptions adopted in his code and Luca Ciotti for many useful suggestions concerning the content of an early version of this manuscript. Several of us acknowledge support from Project PRIN MUR 2022 (code 2022ARWP9C) "Early Formation and Evolution of Bulge and HalO (EFEBHO)" (PI: M. Marconi), funded by the European Union—Next Generation EU, and from the large grant INAF 2023 MOVIE (PI: M. Marconi). G.F., A.N., and M.T. acknowledge support from

NextGenerationEU funds within the National Recovery and Resilience Plan (PNRR), Mission 4— Education and Research, Component 2—From Research to Business (M4C2), Investment Line 3.1—Strengthening and creation of Research Infrastructures, Project IR0000034—"STILES—Strengthening the Italian Leadership in ELT and SKA," CUP C33C22000640006. M.F. acknowledges financial support from the ASI-INAF agreement no. 2022-14-HH.0. M.Mo. acknowledges support from the Spanish Ministry of Science, Innovation, and Universities (MICIU) through the Spanish State Research Agency under the grants "RR Lyrae Stars, a Lighthouse to Distant Galaxies and Early Galaxy Evolution" and the European Regional Development Fund (ERDF) with reference PID2021-127042OB-I00 and from the Severo Ochoa Programe 2020-2023 (CEX2019-000920-S). M.Mo. and G.F. acknowledge the INAF projects "Participation in LSST—Large Synoptic Survey Telescope" (LSST inkind contribution ITA-INA-S22, PI: G. Fiorentino), OB.FU. 1.05.03.06 and "MINI-GRANTS (2023) DI RSN 2" (PI: G. Fiorentino), OB.FU. 1.05.23.04.02. P.B.T. acknowledges partial funding by Fondecyt-ANID 1240465/2024 and ANID Basal Project FB210003. F.A.G. acknowledges support from the ANID BASAL project FB210003, from the ANID FONDECYT Regular grants 1251493 and from the HORIZON-MSCA-2021-SE-01 Research and Innovation Programme under the Marie Sklodowska-Curie grant agreement number 101086388. A.M. acknowledges support from the ANID BASAL project FB210003, from the ANID FONDECYT Regular grant 1251882, and funding from the HORIZON-MSCA-2021-SE-01 Research and Innovation Programme under the Marie Sklodowska-Curie grant agreement number 101086388.

G.B. and G.F. dedicate this paper to Anita whose arrival has revolutionized our lives.

This research has been supported by the Munich Institute for Astro-, Particle, and BioPhysics (MIAPbP), which is funded by the Deutsche Forschungsgemeinschaft (DFG, German Research Foundation) under Germany's Excellence Strategy–EXC-2094–390783311.

This research has made use of both the BaSTI-IAC database (http://basti-iac.oa-abruzzo.inaf.it/index.html) and the CMD 3.7 web interface (http://stev.oapd.inaf.it/cgi-bin/cmd). This research has also made use of the GaiaPortal catalogs access tool, ASI—Space Science Data Center, Rome, Italy (http://gaiaportal.ssdc.asi.it).

Some of the observations reported in this paper were obtained with the Southern African Large Telescope (SALT).

Guoshoujing Telescope (the Large Sky Area Multi-Object Fiber Spectroscopic Telescope: LAMOST) is a National Major Scientific Project built by the Chinese Academy of Sciences. Funding for the project has been provided by the National Development and Reform Commission. LAMOST is operated and managed by the National Astronomical Observatories, Chinese Academy of Sciences.

Funding for the Sloan Digital Sky Survey V has been provided by the Alfred P. Sloan Foundation, the Heising-Simons Foundation, the National Science Foundation, and the Participating Institutions. SDSS acknowledges support and resources from the Center for High-Performance Computing at the University of Utah. SDSS telescopes are located at Apache Point Observatory, funded by the Astrophysical Research Consortium and operated by New Mexico State University, and at Las Campanas Observatory, operated by the Carnegie Institution for Science. The SDSS website is www.sdss.org. SDSS is managed by the Astrophysical Research Consortium for the Participating Institutions of the SDSS Collaboration, including the Carnegie Institution for Science, Chilean National Time Allocation Committee (CNTAC) ratified researchers, Caltech, the Gotham Participation Group, Harvard University, Heidelberg University, The Flatiron Institute, The Johns Hopkins University, L'Ecole polytechnique fédérale de Lausanne (EPFL), Leibniz-Institut für Astrophysik Potsdam (AIP), Max-Planck-Institut für Astronomie (MPIA Heidelberg), Max-Planck-Institut für Extraterrestrische Physik (MPE), Nanjing University, National Astronomical Observatories of China (NAOC), New Mexico State University, The Ohio State University, Pennsylvania State University, Smithsonian Astrophysical Observatory, Space Telescope Science Institute (STScI), the Stellar Astrophysics Participation Group, Universidad Nacional Autónoma de México, University of Arizona, University of Colorado Boulder, University of Illinois at Urbana-Champaign, University of Toronto, University of Utah, University of Virginia, Yale University, and Yunnan University.

This work has made use of data from the European Space Agency (ESA) mission Gaia https://www.cosmos.esa.int/gaia, processed by the Gaia Data Processing and Analysis Consortium (DPAC, https://www.cosmos.esa.int/web/gaia/dpac/consortium). Funding for DPAC has been provided by national institutions, in particular the institutions participating in the Gaia Multilateral Agreement.

This work made use of the Third Data Release of the GALAH Survey (Buder et al. 2021). The GALAH Survey is based on data acquired through the Australian Astronomical Observatory, under programs: A/2013B/13 (The GALAH pilot survey); A/2014A/25, A/2015A/19, A2017A/18 (The GALAH survey phase 1); A2018A/18 (Open clusters with HERMES); A2019A/1 (Hierarchical star formation in Ori OB1); A2019A/15 (The GALAH survey phase 2); A/2015B/19, A/2016A/22, A/2016B/10, A/2017B/16, A/2018B/15 (The HERMES-TESS program); and A/2015A/3, A/2015B/1, A/2015B/19, A/2016A/22, A/2016B/12, A/2017A/14 (The HERMES K2-follow-up program). We acknowledge the traditional owners of the land on which the AAT stands, the Gamilaraay people, and pay our respects to elders past and present. This paper includes data that has been provided by AAO Data Central (datacentral.org.au).

Funding for RAVE has been provided by: the Leibniz-Institut für Astrophysik Potsdam (AIP); the Australian Astronomical Observatory; the Australian National University; the Australian Research Council; the French National Research Agency (Programme National Cosmology et Galaxies (PNCG) of CNRS/INSU with INP and IN2P3, co-funded by CEA and CNES); the German Research Foundation (SPP 1177 and SFB 881: Project-ID 138713538); the European Research Council (ERC-StG 240271 Galactica); the Istituto Nazionale di Astrofisica at Padova; The Johns Hopkins University; the National Science Foundation of the USA (AST-0908326); the W. M. Keck foundation; the Macquarie University; the Netherlands Research School for Astronomy; the Natural Sciences and Engineering Research Council of Canada; the Slovenian Research Agency (research core funding no. P1- 0188); the Swiss National Science Foundation; the Science & Technology Facilities Council of

the UK; Opticon; Strasbourg Observatory; and the Universities of Basel, Groningen, Heidelberg, and Sydney.

This research used data obtained with the Dark Energy Spectroscopic Instrument (DESI). DESI construction and operations is managed by the Lawrence Berkeley National Laboratory. This research is supported by the U.S. Department of Energy, Office of Science, Office of High-Energy Physics, under Contract No. DE-AC02-05CH11231, and by the National Energy Research Scientific Computing Center, a DOE Office of Science User Facility under the same contract. Additional support for DESI is provided by the U.S. National Science Foundation, Division of Astronomical Sciences under Contract No. AST-0950945 to the NSF's National Optical-Infrared Astronomy Research Laboratory; the Science and Technology Facilities Council of the United Kingdom; the Gordon and Betty Moore Foundation; the Heising-Simons Foundation; the French Alternative Energies and Atomic Energy Commission (CEA); the National Council of Science and Technology of Mexico (CONACYT); the Ministry of Science and Innovation of Spain; and by the DESI Member Institutions (www.desi.lbl.gov/collaborating-institutions). The DESI collaboration is honored to be permitted to conduct astronomical research on Iolkam Du'ag (Kitt Peak), a mountain with particular significance to the Tohono O'odham Nation. Any opinions, findings, and conclusions or recommendations expressed in this material are those of the author(s) and do not necessarily reflect the views of the U.S. National Science Foundation, the U.S. Department of Energy, or any of the listed funding agencies.

This publication makes use of data products from the Wide-field Infrared Survey Explorer (WISE), which is a joint project of the University of California, Los Angeles, and the Jet Propulsion Laboratory/California Institute of Technology, and NEOWISE, which is a project of the Jet Propulsion Laboratory/California Institute of Technology. WISE and NEOWISE are funded by the National Aeronautics and Space Administration.

This publication makes use of data products from the Two Micron All Sky Survey (2MASS), which is a joint project of the University of Massachusetts and the Infrared Processing and Analysis Center/California Institute of Technology, funded by the National Aeronautics and Space Administration and the National Science Foundation.

Appendix A
Individual RRL Distances

Precise and homogeneous individual RRL distances are mandatory to constrain the radial gradients and the possible occurrence of local overdensities. A detailed description of the distance estimate will be provided in the next paper on the photometric catalog (V. F. Braga et al. 2025, in preparation), but here we discuss a few issues that are crucial for this work. One fundamental subsample to be defined is that of the RRLs with trustable Gaia parallaxes. These are all the RRLs that comply with the following selection criterion:

`gaiadr3.gaia_source.ruwe < 1.4 ANDgaiadr3.gaia_source.ipd_frac_multi_peak ⩽ 30 AND gaiadr3.gaia_source.parallax_corrected > 0 AND gaiadr3.gaia_source.parallax_over_error_corrected ⩾ 10.`

`Parallax_corrected` and `parallax_over_error_corrected` were obtained by adopting the zero-points calculated with the Python package by L. Lindegren et al. (2021).

We label this subsample, that contains 6666 RRLs, as *good_*π, meaning "good parallax."

The estimate of the individual distances moves along two different paths.

(i) RRLs for which no iron measurement/estimate is available. This is the largest sample, and includes roughly 90% of RRLs in PR3C. We label this sample *no_iron*.

(ii) RRLs for which an estimate of the iron abundance, based either on a spectroscopic measurement (LR, HR spectra) or on a photometric estimate (Fourier parameters), is available. We label this sample *has_iron*. SR3C is a subsample of *has_iron*.

Concerning the *no_iron* sample, we performed a test using predicted metallicity–independent period-luminosity (PL) and metallicity–dependent period–luminosity–metallicity (PLZ) relations for FU and FO RRLs (M. Marconi et al. 2015). To use the PLZ relations we adopted a mean metallicity of [Fe/H] = −1.56 that is the mean metallicity of halo RRLs (see Section 3.1). Note that TND/TCD RRLs and RRLs in retrograde orbits display, within the errors, similar peaks in their metallicity distribution.

Figure 24 shows the fractional difference for individual distances of FU and FO RRLs based on the PLZ and PL relations mentioned above ($W1$ in the top panel and K_s in the bottom panel). The test was performed on the *no_iron* sample. In both cases, the displacement from 0 is smaller than the typical relative uncertainty of the distance estimates and is due to a small difference between the slope of the PL and PLZ relations. The mean and the standard deviations of the distributions are 0.0264 ± 0.0064 ($W1$) and −0.00676 ± 0.00010 (K_s). This means that for the distance measurements of RRLs without an iron estimate we can safely adopt a PLZ by fixing [Fe/H] at –1.56.

The individual RRL distances for the *no_iron* sample were estimated using a mean iron abundance and the empirical PLZ relations provided either by J. P. Mullen et al. (2023, MIR), A. Bhardwaj (2022, K), M. Marconi et al. (2015, J, H), C. Cáceres & M. Catelan (2008, i, z), J. R. Neeley et al. (2019, I), or by Z. Prudil et al. (2024, G, G_{RP}).

The use of PLZ relations has several indisputable advantages when compared with the classical RRL absolute visual magnitude–metallicity (M_V–[Fe/H]) relation. (i) They are linear over the entire period range. (ii) They are minimally affected by evolutionary effects (off-ZAHB evolution). (iii) They are less sensitive to metallicity uncertainties, since the coefficient of the metallicity term in optical/NIR/MIR PLZ relations is at least a factor of two smaller compared to the M_V–[Fe/H] relation. (iv) The sensitivity to uncertainties in the reddening corrections is at least one order of magnitude smaller than in the optical bands.

The individual distances of the RRLs in the *has_iron* sample were estimated by using the individual abundances and their intrinsic errors with the same approach adopted for the *no_iron* sample. This homogeneity is the most important reason for which, in the end, we adopted PLZs for both groups.

For each RRL, we adopted a well-defined priority list for the estimate of individual distances. The periods mainly come from the Gaia dataset; when this was not available, we adopted the period from the original catalog (OGLE, ASAS-SN etc.) and for a small sample we provided our own estimates. Concerning the

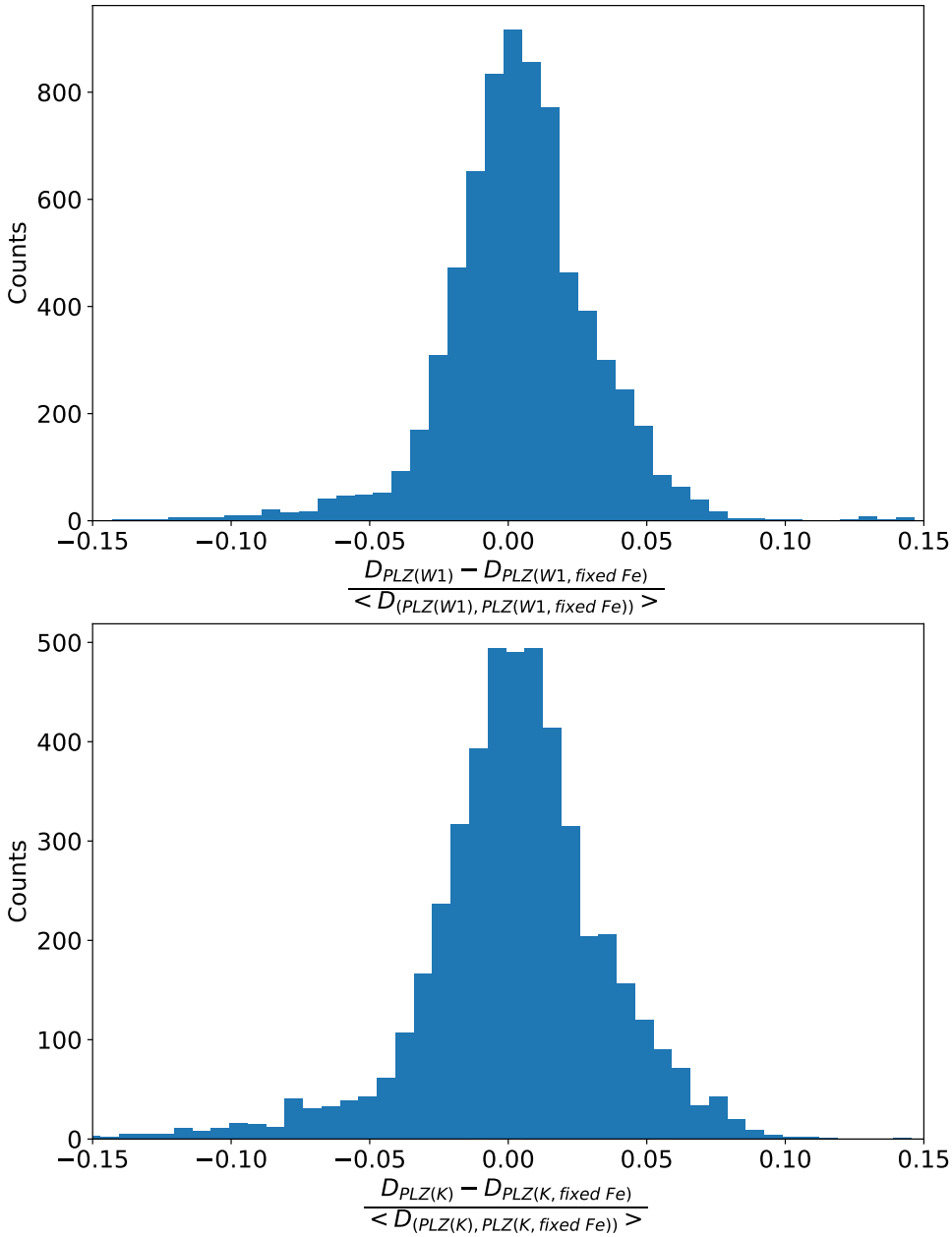

Figure 24. Top: fractional difference between distances based on the PLZ relation in the *W*1 band by either taking into account for the iron abundance or at a fixed [Fe/H] of –1.51 (M. Fabrizio et al. 2021). Bottom: same as the top, but for the *K* band.

apparent magnitudes, the highest priority was given to MIR and NIR magnitudes. The reasons are the following: (i) The pulsation amplitudes in the NIR/MIR bands are at least a factor of four/five smaller ($\Delta K = 0.2$–0.4 mag) than in the optical ($\Delta B = 1.0$–1.8) bands. This means that we can use either the mean of the measurements or the single epoch random measurements as a solid proxy of the mean magnitude based on the fit of the light curve (L. Inno et al. 2013; V. F. Braga et al. 2019). (ii) They are about one order of magnitude less affected by uncertainties in reddening corrections. (iii) They are homogeneous, since 2MASS and WISE cover the entire sky and they are rooted on accurate standard photometric systems. (iv) NIR/MIR PL/PLZ relations are steeper than in the optical regime. As a whole, 42% of the RRLs in PR3C have individual distances based on NIR/MIR PLZ relations.

The individual distances of the RRLs with no NIR/MIR measurements are based either on the i/z-band PLZ relations or in the G/G_{RP}-band PLZ relation or by Gaia parallaxes of the *good_*π sample. The fraction of RRLs in PR3C with individual distances based on optical PLZ relations is 52%.

Individual distances also require homogeneous reddening corrections. This is why we adopted the reddening map provided by E. F. Schlafly & D. P. Finkbeiner (2011). Although this map is not optimal for the bulge and TND, it is the best compromise between sky coverage (full), homogeneity, and reliability for halo stars, which represent our largest sample (O. A. Gonzalez et al. 2012, see their Figure 5). The reddening corrections were estimated in the different photometric bands by using the empirical reddening law provided by J. A. Cardelli et al. (1989).

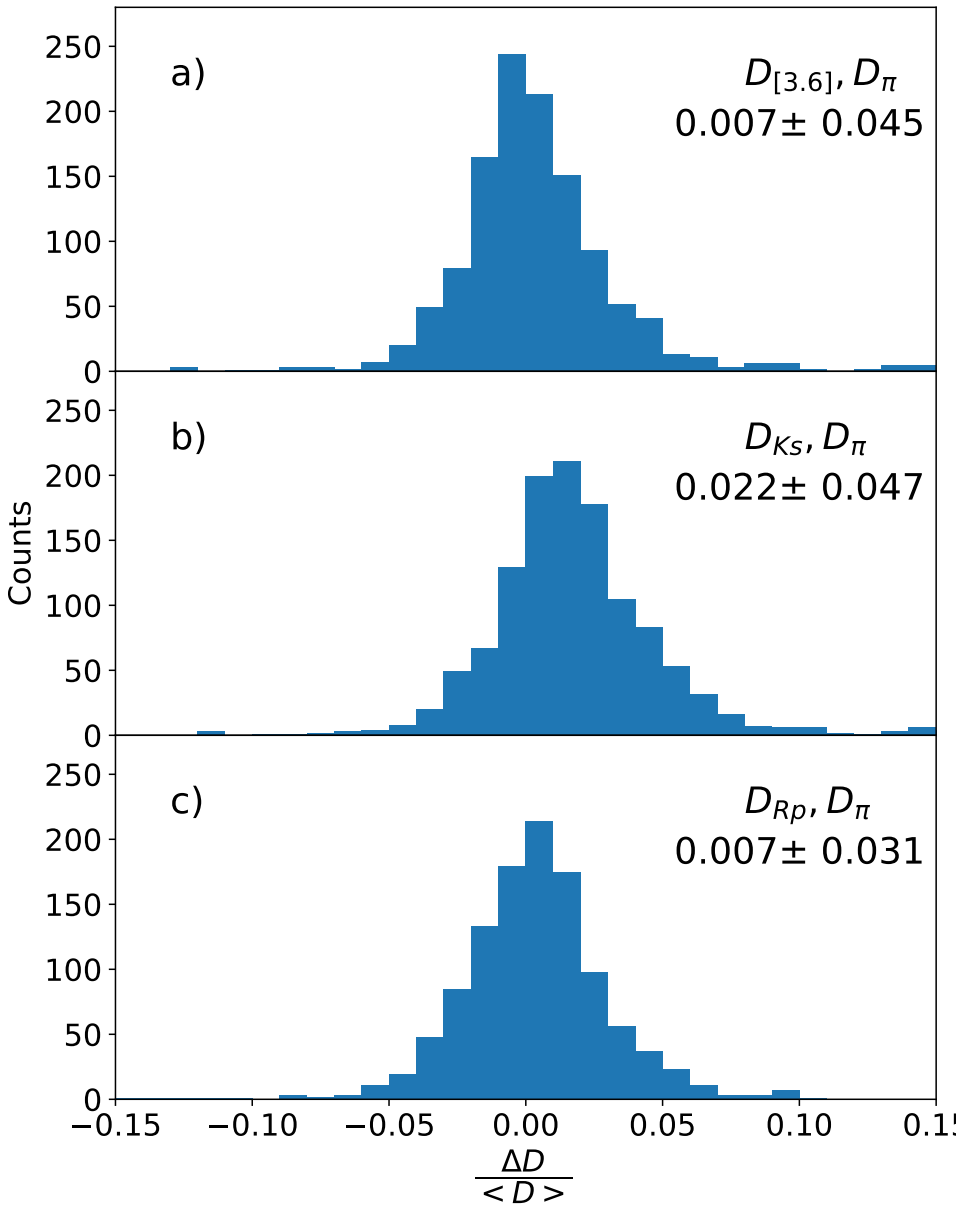

Figure 25. Panel (a): distribution of the relative difference in distance derived from the PLZ([3.6]) relation and from the inverse Gaia DR3 parallax, only for the intersection of the *good_*π and SR3C. The mean difference is labeled. Panel (b): same as Panel (a), but for the PLZ(K) relation. Panel (c): same as Panel (a), but for PLZ(R_p) relation.

Concerning the SR3C, we ended up with a sample of 7708 RRL stars with individual distances estimated using either the NIR (K band, 4%; H band, 1.5%; J band, 1.5%) or the MIR PLZ relations ($W1$ and $W2$, 93%; the $W1$ and $W2$ bands are centered at 3.6 and 4.5 μm, respectively).

The top panel of Figure 24 displays the fractional difference between the distances of RRLs of the *has_iron* sample obtained with the PLZ($W1$) by either fixing [Fe/H] at –1.56 (F21) or using the spectroscopic metallicity from our catalog. Figure 25 displays the same fractional difference in Galactocentric distance between Gaia parallaxes of the *good_*π sample and distances based on PLZ relations (from top to bottom, using the $W1$, Ks, and Rp PLZs). The fractional differences are, as expected, on average smaller than the standard deviations (see labeled values). This plot serves as a validation for our set of distances, since we are comparing the best geometric estimates to our sample.

Appendix B
Comparison between Different Galactic Potentials

In order to constrain the impact of the adopted MW potential on the RRLs associated with the main Galactic components and to the stellar streams, we performed an independent orbital integration by using the MW potential of P. J. McMillan (2017) as implemented in AGAMA (E. Vasiliev 2019). Interestingly enough, we found that both iron and α-element distribution functions based on the MW potential of J. Bovy (2015) (see Figure 8) and of P. J. McMillan (2017) (see Figure 26) are quite similar. The same outcome applies to the distribution in the different kinematic planes of the candidate RRLs associated with the main Galactic components (Figure 10 versus Figure 27) and to the selected stellar streams (Figure 11 versus Figure 28).

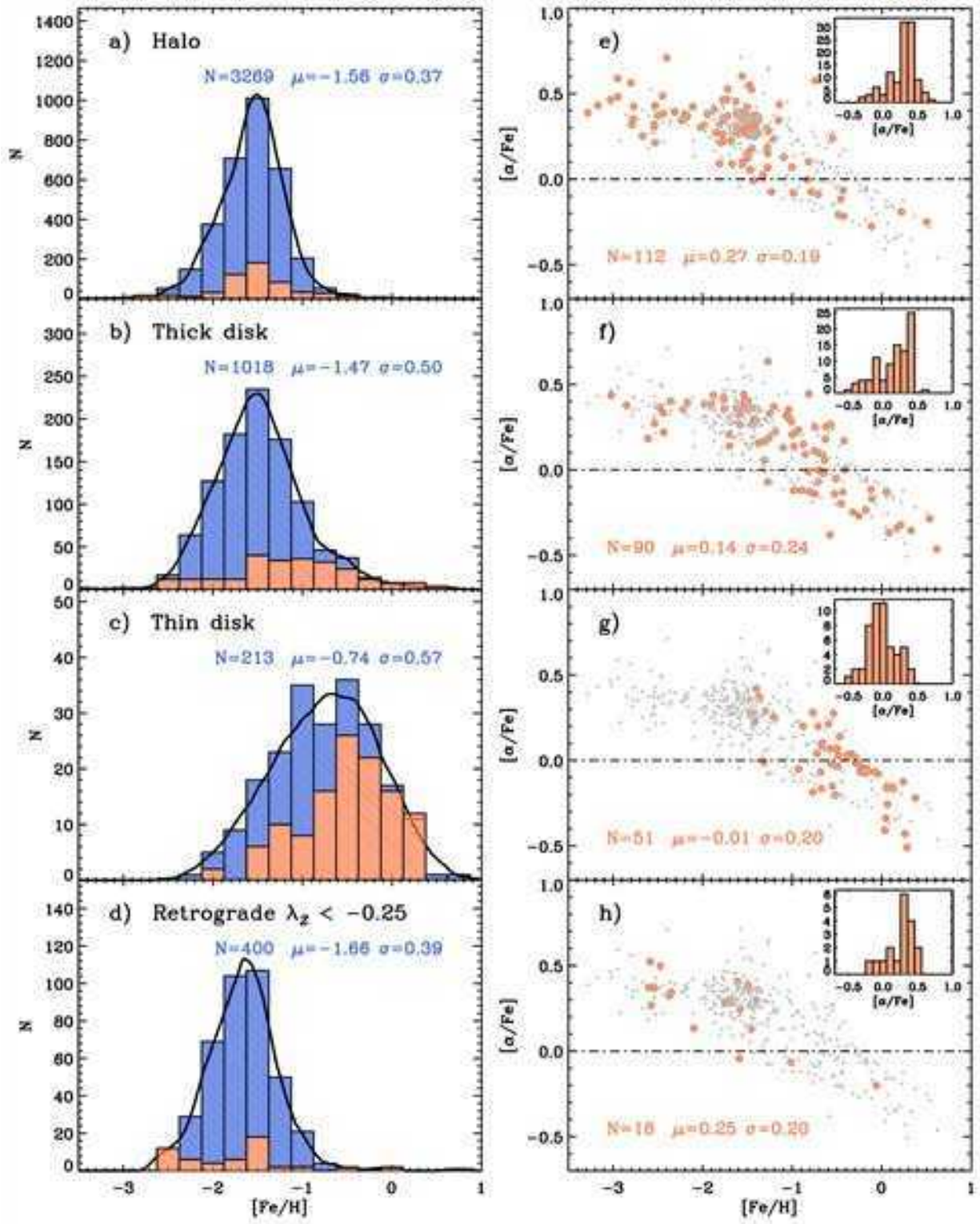

Figure 26. Same as Figure 8, but the orbits were integrated by using the MW potential of P. J. McMillan (2017).

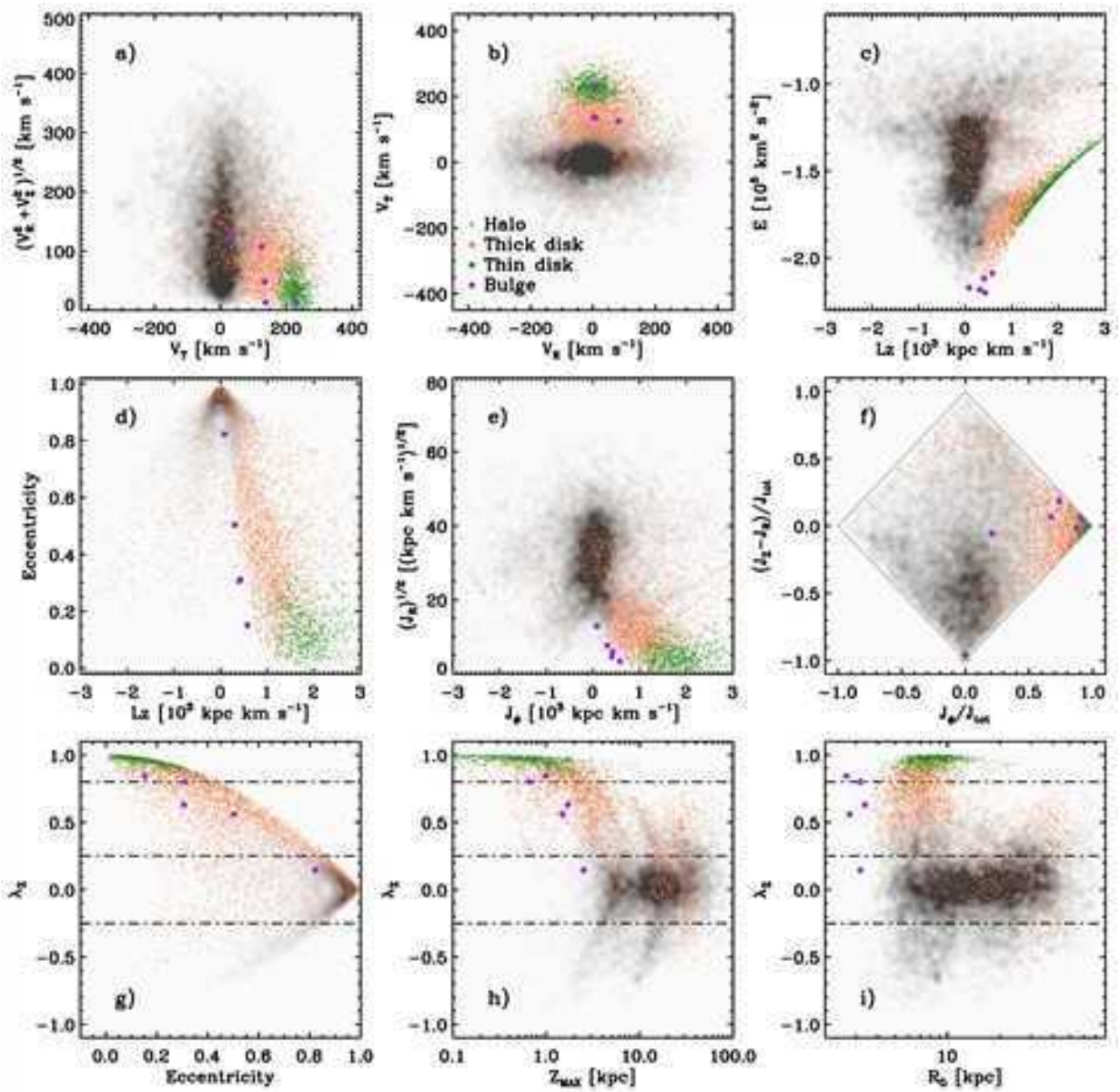

Figure 27. Same as Figure 10, but the orbits were integrated by using the MW potential of P. J. McMillan (2017).

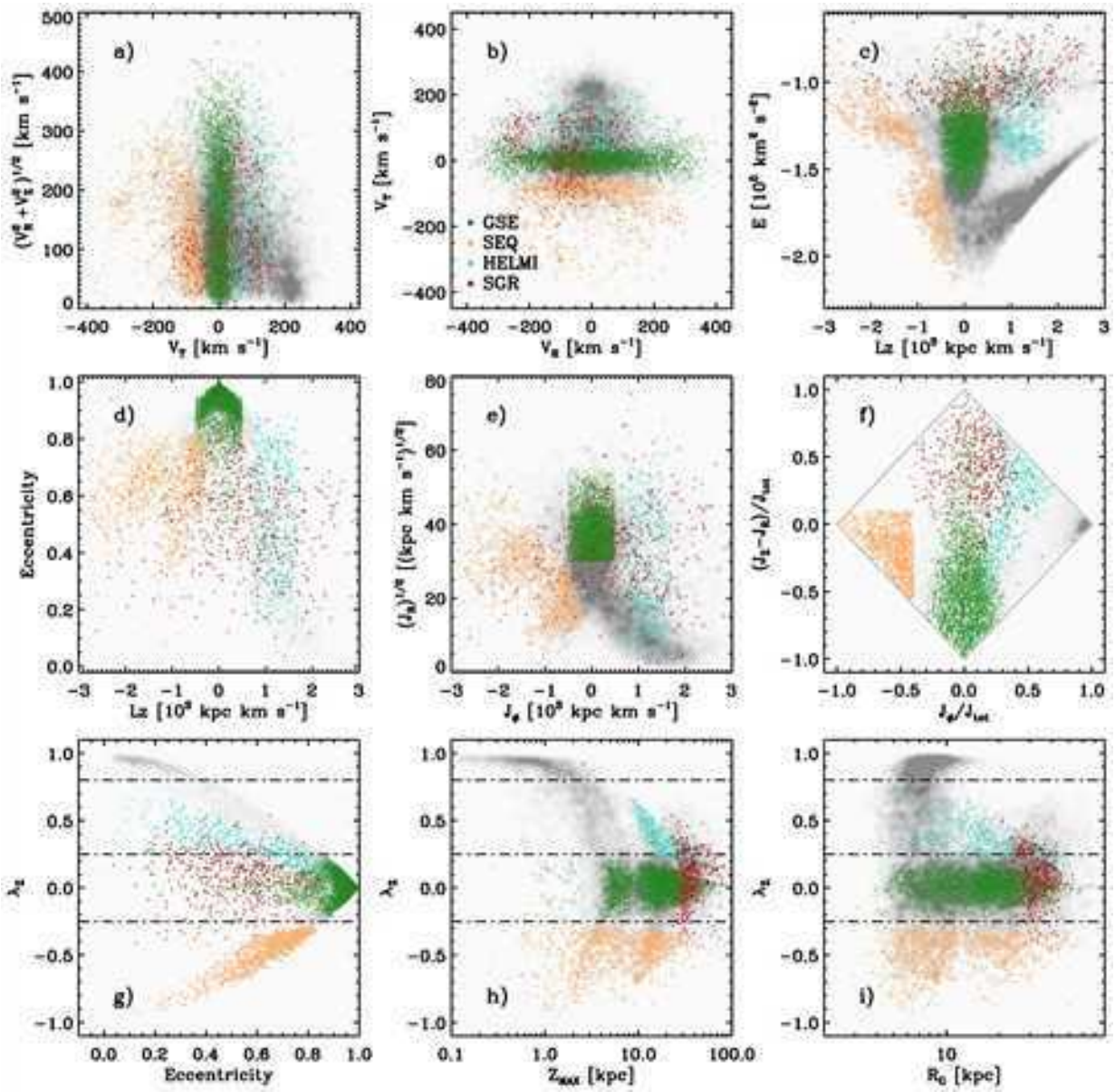

Figure 28. Same as Figure 11, but the orbits were integrated by using the MW potential of P. J. McMillan (2017).

Appendix C
Analytical Fits of the Iron Radial Gradients

The analytical fits of the iron radial gradient in the different Galactic components were performed by using both linear and logarithmic Galactocentric distances (see Section 5.1). The coefficients of the analytical fits are listed in Table 2, and the fits based on linear distances are shown in Figure 29.

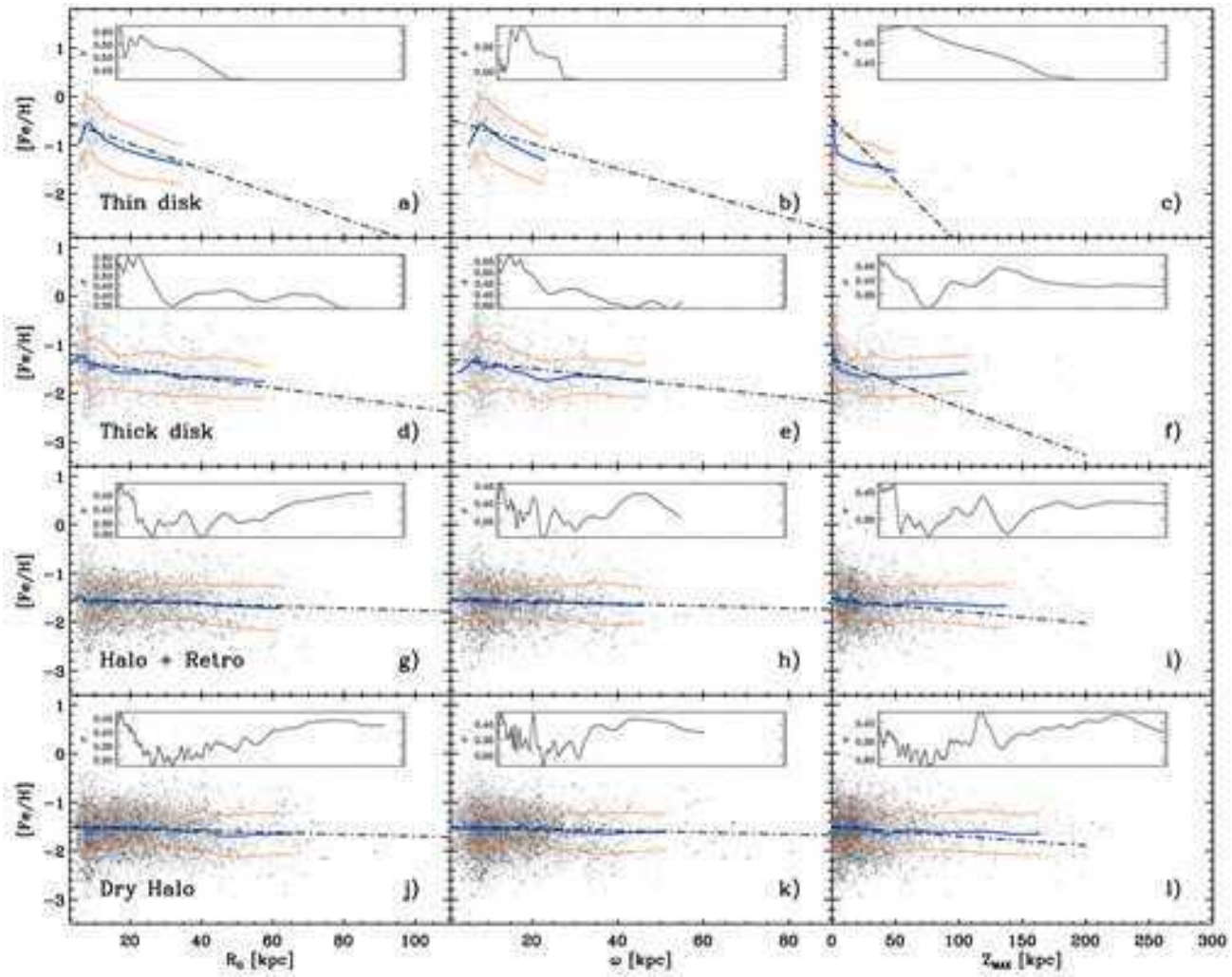

Figure 29. Panels (a), (b), (c): iron abundance for TND RRLs as a function of Galactocentric distance (panel (a)), distance projected onto the Galactic plane (panel (b)), and maximum height above the Galactic plane (panel (c)). The X-axes are in linear scale. The blue lines display the running average, while the orange lines the standard deviation of the running average. The dashed–dotted lines show the linear fit over the different subsamples. The insets display the standard deviation of the spectroscopic sample as a function of distance. Panels (d), (e), (f): same as the top, but for TCD RRLs. Panels (g), (h), (i): same as the top, but for Halo+Retro RRLs. Panels (j), (k), (l): same as the top, but for dry Halo+Retro RRLs. See text for more details.

Appendix D
Spectroscopic Rome RR Lyrae Catalog (SR3C)

D.1. Spectroscopic Rome RR Lyrae Catalog (SR3C_ab)

Tables 7 and 8 include individual elemental abundances of the RRLs in the SR3C based on HR spectra, and are published in their entirety in machine-readable format.

Table 7
Iron Abundances from HR Spectroscopy for the RRLs in the SR3C[a]

Gaia DR3 ID	α(ICRS)	δ(ICRS)	[Fe/H]$_{lit}$[b]	[Fe/H]$_{ours}$[c]	References[d]
6565527904791301504	324.51483	−44.68671	…	−0.47 ± 0.04	1,2
6380659528686603008	352.38918	−72.54447	…	−1.86 ± 0.01	1,2
6321161342439508480	229.59119	−8.46186	…	−0.54 ± 0.01	1,2
4818348922610995200	73.31013	−37.82105	…	−0.93 ± 0.03	1,2
3464204523694392192	177.48464	−35.64746	…	−0.77 ± 0.11	1,2

Notes.
[a] Table 7 is published in its entirety in a machine-readable format. A portion is shown here for guidance regarding its form and content.
[b] Iron abundances from the literature, when available.
[c] Iron abundances either estimated for this work or converted into our metallicity scale.
[d] References: (1) C21a, (2) C21b, (3) J. Fernley & T. G. Barnes (1996), (4) J. M. Nemec et al. (2013), (5) E. Pancino et al. (2015), (6) C. Sneden et al. (2017), (7) S. Andrievsky et al. (2018), (8) S. Duffau et al. (2014), (9) S. Buder et al. (2021), (10) D24, 11) G21.

(This table is available in its entirety in machine-readable form in the online article.)

Table 8
α-element Abundances from HR Spectroscopy for the RRLs in the SR3C[a]

Gaia DR3 ID	α(ICRS)	δ(ICRS)	[α/Fe]$_{lit}$[b]	[α/Fe]$_{ours}$[c]	Ref.[d]
77849374617106176	30.13959	14.19830	…	0.13 ± 0.02	1,2
80556926295542528	34.01548	17.53298	…	0.44 ± 0.12	1,2
3496128160933491 20	28.78455	43.76568	…	0.07 ± 0.06	1,2
5843716010263742 72	133.72292	6.43682	…	0.22 ± 0.09	1,2
6304219354318712 32	151.93102	23.99171	…	0.26 ± 0.11	1,2

Notes.
[a] Table 8 is published in its entirety in a machine-readable format. A portion is shown here for guidance regarding its form and content.
[b] α-element abundances from the literature, when available.
[c] α-element abundances either estimated for this work or converted into our metallicity scale.
[d] References: (1) C21b, (2) D24, (3) S. Buder et al. (2021).

(This table is available in its entirety in machine-readable form in the online article.)

D.2. Spectroscopic Rome RR Lyrae Catalog (SR3C_fe)

Table 9 lists iron abundances of the RRLs in the SR3C based on the ΔS method (MR or LR spectroscopy), and is published in its entirety in machine-readable format.

D.3. Spectroscopic Rome RR Lyrae Catalog (SR3C_rv)

Table 10 includes the orbital and kinematic parameters, calculated using the MWPotential2014, and the RV measurements for the RRLs in the SR3C, and is published in its entirety in machine-readable format.

Table 9
Iron Abundances from MR/LR Spectroscopy for the RRLs in the SR3C[a]

Gaia DR3 ID	α(ICRS)	δ(ICRS)	$[Fe/H]_{lit}$[b]	$[Fe/H]_{ours}$[c]	References[d]
780156482623646080	162.57884	42.56894	…	-1.05 ± 0.17	1
777128427600786176	166.91592	40.56588	…	-1.12 ± 0.19	1
776846196710082560	163.3049	41.31707	…	-1.83 ± 0.19	1
765539437605028096	169.09549	41.23367	…	-2.16 ± 0.14	1
717795623366814464	132.10925	36.33541	…	-1.72 ± 0.19	1

Notes.
[a] Table 9 is published in its entirety in a machine-readable format. A portion is shown here for guidance regarding its form and content.
[b] Iron abundances from the literature, when available.
[c] Iron abundances either estimated for this work or converted into our metallicity scale.
[d] References: (1) C21a, (2) R. Zinn et al. (2020), (3) G. C. Liu et al. (2020), (4) A. K. Dambis et al. (2013), (5) B. Sesar et al. (2013), (6) M. Steinmetz et al. (2020b), (7) G. E. Medina et al. (2023), (8) T. D. Kinman et al. (2012).

(This table is available in its entirety in machine-readable form in the online article.)

Table 10

Orbital and Kinematic Parameters, Calculated by Using the MWPotential2014, and Center of Mass RV (γ), from HR, MR, and LR Spectroscopy, for the RRLs in the SR3C, and Their Uncertainties

Gaia DR3 ID	α(J2000)	δ(J2000)	R_{Gal}[a]	Z_{max}[b]	e[c]	V_Z[d]	V_T[e]	V_R[f]	J_R[g]	J_ϕ[h]	J_Z[i]	L_Z[j]	E[k]	λ_Z[l]	γ[m]	References[n]
6771307454464848768	293.08657	−23.85379	7476.28999 ± 10.52805	$0.45477^{0.48649}_{0.42397}$	$0.78209^{0.78966}_{0.77391}$	$-25.80982^{-24.24645}_{-27.27631}$	$52.30631^{54.43635}_{50.32165}$	$15.60223^{18.06603}_{13.30678}$	$456.03313^{461.90186}_{449.80509}$	$390.86946^{407.31625}_{375.57891}$	$6.45489^{7.13120}_{5.78387}$	$390.86946^{407.31625}_{375.57891}$	$-150673.22640^{-150490.30277}_{-150832.624496}$	$0.34957^{0.36312}_{0.33683}$	-60.44 ± 2.04	1
2720896455287475584	333.85694	6.82262	8000.02440 ± 8.35446	$0.50384^{0.53211}_{0.47806}$	$0.29926^{0.30354}_{0.29501}$	$21.41938^{23.50233}_{19.33163}$	$180.69917^{182.22681}_{179.18736}$	$59.89313^{60.21600}_{59.58380}$	$97.15102^{99.54160}_{94.78423}$	$1444.65238^{1456.54736}_{1432.86493}$	$7.10791^{7.81510}_{6.48204}$	$1444.65238^{1456.54736}_{1432.86493}$	$-130363.21989^{-130113.47739}_{-130605.382171}$	$0.90490^{0.90834}_{0.90134}$	-71.38 ± 2.46	1
2857456211775108480	5.92951	29.40092	8315.02890 ± 8.11582	$0.40298^{0.42601}_{0.38189}$	$0.12897^{0.13130}_{0.12664}$	$-17.15670^{-15.92234}_{-18.44854}$	$220.93228^{221.68654}_{220.18918}$	$-37.45245^{-37.20558}_{-37.69041}$	$20.84389^{21.53783}_{20.16101}$	$1836.28753^{1843.32659}_{1829.35207}$	$4.63224^{5.09731}_{4.21910}$	$1836.28753^{1843.32659}_{1829.35207}$	$-121414.00417^{-121205.73969}_{-121617.37576}$	$0.97888^{0.97893}_{0.97880}$	−20.1 ± 1.24	1
5947570591534602240	269.79456	−49.43350	7316.30910 ± 12.67856	$0.70793^{0.72501}_{0.69542}$	$0.69600^{0.70232}_{0.68985}$	$37.01246^{37.54327}_{36.48057}$	$109.55267^{111.23729}_{107.84332}$	$-178.85091^{-177.21023}_{-180.51917}$	$519.41094^{528.84601}_{510.19189}$	$801.32543^{814.90901}_{787.57781}$	$9.26527^{9.53640}_{8.99720}$	$801.32543^{814.90901}_{787.57781}$	$-131058.15554^{-131003.82814}_{-131104.20290}$	$0.50813^{0.51722}_{0.49899}$	183.29 ± 1.90	1
6883653108749373568	315.37039	−15.22995	7429.18591 ± 16.52036	$10.82856^{11.92122}_{9.84896}$	$0.50039^{0.53291}_{0.46677}$	$-186.12153^{-181.41741}_{-190.79617}$	$-284.66154^{-278.18329}_{-291.09982}$	$-58.20650^{-55.01286}_{-61.39260}$	$525.11028^{636.45699}_{428.04163}$	$-2107.48638^{-2062.39184}_{-2152.20299}$	$386.36100^{401.06324}_{371.60424}$	$-2107.48638^{-2062.39184}_{-2152.20299}$	$-92737.24997^{-89869.13967}_{-95552.73995}$	$-0.63894^{-0.61353}_{-0.66354}$	−105.15 ± 1.34	1

Notes.

[a] Galactocentric distance.

[b] Maximum height above the Galactic plane.

[c] Eccentricity of the orbit.

[d] Vertical velocity component.

[e] Transversal velocity component.

[f] RV component.

[g] Radial orbital action.

[h] Azimuthal orbital action.

[i] Vertical orbital action.

[j] Vertical angular momentum component.

[k] Orbital energy.

[l] Circularity of the orbit.

[m] Center of mass RV.

[n] References (referring to γ velocity only): (1) G. Bono et al. (2020), (2) Gaia Collaboration et al. (2023b), (3) R. Zinn et al. (2020), (4) Z. Prudil (private communication), (5) S. Duffau et al. (2014), (6) G. E. Medina et al. (2023), (7) D24, (8) J. M. Nemec et al. (2013), (9) C. J. Hansen et al. (2011), (10) S. Buder et al. (2021), (11) J. Crestani (private communication), TW) This work.

(This table is available in its entirety in machine-readable form in the online article.)

ORCID iDs

G. Bono https://orcid.org/0000-0002-4896-8841
V. F. Braga https://orcid.org/0000-0001-7511-2830
M. Fabrizio https://orcid.org/0000-0001-5829-111X
M. Tantalo https://orcid.org/0000-0002-6829-6704
J. Crestani https://orcid.org/0000-0001-8926-3496
V. D'Orazi https://orcid.org/0000-0002-2662-3762
M. Dall'Ora https://orcid.org/0000-0001-8209-0449
G. Fiorentino https://orcid.org/0000-0003-0376-6928
M. Marengo https://orcid.org/0000-0001-9910-9230
C. E. Martínez-Vázquez https://orcid.org/0000-0002-9144-7726
M. Monelli https://orcid.org/0000-0001-5292-6380
J. P. Mullen https://orcid.org/0000-0002-1650-2764
Z. Prudil https://orcid.org/0000-0001-5497-5805
C. Sneden https://orcid.org/0000-0002-3456-5929
G. Altavilla https://orcid.org/0000-0002-9934-1352
M. Bergemann https://orcid.org/0000-0002-9908-5571
A. Calamida https://orcid.org/0000-0002-0882-7702
E. Carretta https://orcid.org/0000-0002-1569-1911
B. Chaboyer https://orcid.org/0000-0003-3096-4161
M. Correnti https://orcid.org/0000-0001-6464-3257
F. A. Gómez https://orcid.org/0000-0002-1947-333X
S. Kwak https://orcid.org/0000-0003-0957-6201
M. Marconi https://orcid.org/0000-0002-1330-2927
F. Matteucci https://orcid.org/0000-0001-7067-2302
A. Monachesi https://orcid.org/0000-0003-2325-9616
I. Musella https://orcid.org/0000-0001-5909-6615
V. Ripepi https://orcid.org/0000-0003-1801-426X
M. Sánchez-Benavente https://orcid.org/0000-0003-2693-279X
E. Spitoni https://orcid.org/0000-0001-9715-5727
P. B. Stetson https://orcid.org/0000-0001-6074-6830
F. Thévenin https://orcid.org/0000-0002-5032-2476
I. B. Thompson https://orcid.org/0000-0001-5130-6040
P. B. Tissera https://orcid.org/0000-0001-5242-2844
T. Tsujimoto https://orcid.org/0000-0002-9397-3658
E. Valenti https://orcid.org/0000-0002-6092-7145
A. K. Vivas https://orcid.org/0000-0003-4341-6172
A. R. Walker https://orcid.org/0000-0002-7123-8943
M. Zoccali https://orcid.org/0000-0002-5829-2267

References

Abbas, M., Grebel, E. K., Martin, N. F., et al. 2014, AJ, 148, 8
Abolfathi, B., Aguado, D. S., Aguilar, G., et al. 2018, ApJS, 235, 42
Akerlof, C., Amrose, S., Balsano, R., et al. 2000, AJ, 119, 1901
Alfaro, E. J., Cabrera-Cano, J., & Delgado, A. J. 1993, ApJL, 402, L53
Anders, F., Chiappini, C., Minchev, I., et al. 2017, A&A, 600, A70
Andrievsky, S., Wallerstein, G., Korotin, S., et al. 2018, PASP, 130, 024201
Antoja, T., Ramos, P., Mateu, C., et al. 2020, A&A, 635, L3
Armandroff, T. E., Da Costa, G. S., & Zinn, R. 1992, AJ, 104, 164
Aumer, M., & Binney, J. 2017, MNRAS, 470, 2113
Aumer, M., Binney, J., & Schönrich, R. 2017, MNRAS, 470, 3685
Baade, W. 1958, in Ricerche Astronomiche, Specola Vaticana, Proceedings of the Conference Sponsored by the Pontifical Academy of Science and the Vatican Observatory, 5, (North-Holland), 303
Baade, W. 1963, Evolution of Stars and Galaxies (Harvard Univ. Press)
Baumgardt, H., Hilker, M., Sollima, A., & Bellini, A. 2019, MNRAS, 482, 5138
Bellm, E. C., Kulkarni, S. R., Barlow, T., et al. 2019a, PASP, 131, 068003
Bellm, E. C., Kulkarni, S. R., Graham, M. J., et al. 2019b, PASP, 131, 018002
Belokurov, V., Zucker, D. B., Evans, N. W., et al. 2006, ApJL, 647, L111
Bennett, M., & Bovy, J. 2019, MNRAS, 482, 1417
Bensby, T., Feltzing, S., & Oey, M. S. 2014, A&A, 562, A71
Bhardwaj, A. 2022, Univ, 8, 122
Bobrick, A., Iorio, G., Belokurov, V., et al. 2024, MNRAS, 527, 12196
Bonifacio, P., Caffau, E., Monaco, L., et al. 2024, A&A, 684, A91
Bono, G., Caputo, F., Cassisi, S., Incerpi, R., & Marconi, M. 1997a, ApJ, 483, 811
Bono, G., Caputo, F., Cassisi, S., Castellani, V., & Marconi, M. 1997b, ApJ, 479, 279
Bono, G., Caputo, F., Cassisi, S., Castellani, V., & Marconi, M. 1997c, ApJ, 489, 822
Bono, G., Caputo, F., & Di Criscienzo, M. 2007, A&A, 476, 779
Bono, G., Caputo, F., & Stellingwerf, R. F. 1994, ApJL, 432, L51
Bono, G., Iannicola, G., Braga, V. F., et al. 2019, ApJ, 870, 115
Bono, G., Braga, V. F., Crestani, J., et al. 2020, ApJL, 896, L15
Borbolato, L., Rossi, S., Perottoni, H. D., et al. 2025, ApJ, 994, 126
Bovy, J. 2015, ApJS, 216, 29
Braga, V. F., Crestani, J., Fabrizio, M., et al. 2021, ApJ, 919, 85
Braga, V. F., Stetson, P. B., Bono, G., et al. 2016, AJ, 152, 170
Braga, V. F., Stetson, P. B., Bono, G., et al. 2019, A&A, 625, A1
Brown, T. M., Smith, E., Ferguson, H. C., et al. 2006, ApJ, 652, 323
Brown, T. M., Smith, E., Ferguson, H. C., et al. 2009, ApJS, 184, 152
Brusadin, G., Matteucci, F., & Romano, D. 2013, A&A, 554, A135
Buder, S., Sharma, S., Kos, J., et al. 2021, MNRAS, 506, 150
Bullock, J. S., & Johnston, K. V. 2005, ApJ, 635, 931
Butler, D., Carbon, D., & Kraft, R. P. 1976, ApJ, 210, 120
Butler, D., Kemper, E., Kraft, R. P., & Suntzeff, N. B. 1982, AJ, 87, 353
Cáceres, C., & Catelan, M. 2008, ApJS, 179, 242
Cacciari, C., & Clementini, G. 2003, LNP, 635, 105
Caldwell, N., & Romanowsky, A. J. 2016, ApJ, 824, 42
Caldwell, N., Schiavon, R., Morrison, H., Rose, J. A., & Harding, P. 2011, AJ, 141, 61
Callingham, T. M., Cautun, M., Deason, A. J., et al. 2022, MNRAS, 513, 4107
Cardelli, J. A., Clayton, G. C., & Mathis, J. S. 1989, ApJ, 345, 245
Carollo, D., Beers, T. C., Chiba, M., et al. 2010, ApJ, 712, 692
Carollo, D., Beers, T. C., Lee, Y. S., et al. 2007, Natur, 450, 1020
Carretta, E., Bragaglia, A., Gratton, R., D'Orazi, V., & Lucatello, S. 2009, A&A, 508, 695
Chadid, M., Sneden, C., & Preston, G. W. 2017, ApJ, 835, 187
Chiappini, C., Matteucci, F., & Gratton, R. 1997, ApJ, 477, 765
Clementini, G., Ripepi, V., Garofalo, A., et al. 2023, A&A, 674, A18
Clementini, G., Ripepi, V., Molinaro, R., et al. 2019, A&A, 622, A60
Colucci, J. E., Bernstein, R. A., & Cohen, J. G. 2014, ApJ, 797, 116
Conroy, C., Naidu, R. P., Zaritsky, D., et al. 2019a, ApJ, 887, 237
Conroy, C., Bonaca, A., Cargile, P., et al. 2019b, ApJ, 883, 107
Cooper, A. P., Parry, O. H., Lowing, B., Cole, S., & Frenk, C. 2015, MNRAS, 454, 3185
Crestani, J., Fabrizio, M., Braga, V. F., et al. 2021a, ApJ, 908, 20
Crestani, J., Braga, V. F., Fabrizio, M., et al. 2021b, ApJ, 914, 10
Cutri, R. M., Wright, E. L., Conrow, T., et al. 2013, Explanatory Supplement to the AllWISE Data Release Products https://irsa.ipac.caltech.edu/data/WISE/docs/release/AllWISE/expsup/index.html
Daflon, S., & Cunha, K. 2004, ApJ, 617, 1115
Dambis, A. K., Berdnikov, L. N., Kniazev, A. Y., et al. 2013, MNRAS, 435, 3206
Dambis, A. K., Rastorguev, A. S., & Zabolotskikh, M. V. 2014, MNRAS, 439, 3765
de Jong, J. T. A., Yanny, B., Rix, H.-W., et al. 2010, ApJ, 714, 663
De Lucia, G., & Helmi, A. 2008, MNRAS, 391, 14
Dékány, I., Hajdu, G., Grebel, E. K., et al. 2018, ApJ, 857, 54
Dietz, S. E., Yoon, J., Beers, T. C., & Placco, V. M. 2020, ApJ, 894, 34
D'Orazi, V., Braga, V., Bono, G., et al. 2025a, A&A, 694, A158
D'Orazi, V., Iorio, G., Cseh, B., et al. 2025b, A&A, 704, A12
D'Orazi, V., Storm, N., Casey, A. R., et al. 2024, MNRAS, 531, 137
Drake, A. J., Catelan, M., Djorgovski, S. G., et al. 2013, ApJ, 763, 32
Drake, A. J., Djorgovski, S. G., Mahabal, A., et al. 2009, ApJ, 696, 870
Drake, A. J., Djorgovski, S. G., Catelan, M., et al. 2017, MNRAS, 469, 3688
Drimmel, R., & Poggio, E. 2018, RNAAS, 2, 210
Duffau, S., Vivas, A. K., Zinn, R., Méndez, R. A., & Ruiz, M. T. 2014, A&A, 566, A118
Dye, S., Lawrence, A., Read, M. A., et al. 2018, MNRAS, 473, 5113
Eggen, O. J., Lynden-Bell, D., & Sandage, A. R. 1962, ApJ, 136, 748
Escala, I., Gilbert, K. M., Fardal, M., et al. 2022, AJ, 164, 20
Escala, I., Gilbert, K. M., Kirby, E. N., et al. 2020a, ApJ, 889, 177
Escala, I., Gilbert, K. M., Wojno, J., Kirby, E. N., & Guhathakurta, P. 2021, AJ, 162, 45
Escala, I., Kirby, E. N., Gilbert, K. M., et al. 2020b, ApJ, 902, 51
Fabrizio, M., Nonino, M., Bono, G., et al. 2015, A&A, 580, A18
Fabrizio, M., Bono, G., Braga, V. F., et al. 2019, ApJ, 882, 169
Fabrizio, M., Braga, V. F., Crestani, J., et al. 2021, ApJ, 919, 118

Fardal, M. A., Guhathakurta, P., Gilbert, K. M., et al. 2012, MNRAS, 423, 3134
Fernández-Alvar, E., Carigi, L., Allende Prieto, C., et al. 2017, MNRAS, 465, 1586
Fernández-Alvar, E., Kordopatis, G., Hill, V., et al. 2024, A&A, 685, A151
Fernley, J., & Barnes, T. G. 1996, A&A, 312, 957
Feuillet, D. K., Sahlholdt, C. L., Feltzing, S., & Casagrande, L. 2021, MNRAS, 508, 1489
Fiorentino, G., Bono, G., Monelli, M., et al. 2015b, ApJL, 798, L12
Fiorentino, G., Marconi, M., Bono, G., et al. 2015a, ApJ, 810, 15
Fiorentino, G., Monelli, M., Stetson, P. B., et al. 2017, A&A, 599, A125
Font, A. S., McCarthy, I. G., Crain, R. A., et al. 2011, MNRAS, 416, 2802
For, B.-Q., & Sneden, C. 2010, AJ, 140, 1694
For, B.-Q., Sneden, C., & Preston, G. W. 2011, ApJS, 197, 29
Gaia Collaboration, Recio-Blanco, A., Kordopatis, G., et al. 2023a, A&A, 674, A38
Gaia Collaboration, Vallenari, A., Brown, A. G. A., et al. 2023b, A&A, 674, A1
Garofalo, A., Cusano, F., Clementini, G., et al. 2013, ApJ, 767, 62
Gilbert, K. M., Kirby, E. N., Escala, I., et al. 2019, ApJ, 883, 128
Gilbert, K. M., Fardal, M., Kalirai, J. S., et al. 2007, ApJ, 668, 245
Gilbert, K. M., Guhathakurta, P., Kollipara, P., et al. 2009, ApJ, 705, 1275
Gilbert, K. M., Kalirai, J. S., Guhathakurta, P., et al. 2014, ApJ, 796, 76
Gilligan, C. K., Chaboyer, B., Marengo, M., et al. 2021, MNRAS, 503, 4719
Gómez, F. A., Helmi, A., Cooper, A. P., et al. 2013, MNRAS, 436, 3602
Gonzalez, O. A., Rejkuba, M., Zoccali, M., et al. 2012, A&A, 543, A13
GRAVITY Collaboration, Abuter, R., Amorim, A., et al. 2018, A&A, 615, L15
Gregersen, D., Seth, A. C., Williams, B. F., et al. 2015, AJ, 150, 189
Hansen, C. J., Nordström, B., Bonifacio, P., et al. 2011, A&A, 527, A65
Harris, W. E. 1996, AJ, 112, 1487
Harris, W. E. 2010, arXiv:1012.3224
Harris, W. E., & Canterna, R. 1979, ApJL, 231, L19
Hattori, K., & Yoshii, Y. 2011, MNRAS, 418, 2481
Helmi, A. 2020, ARA&A, 58, 205
Helmi, A., White, S. D. M., de Zeeuw, P. T., & Zhao, H. 1999, Natur, 402, 53
Horta, D., Schiavon, R. P., Mackereth, J. T., et al. 2023, MNRAS, 520, 5671
Ibata, R. A., Lewis, G. F., McConnachie, A. W., et al. 2014, ApJ, 780, 128
Inno, L., Matsunaga, N., Bono, G., et al. 2013, ApJ, 764, 84
Iorio, G., & Belokurov, V. 2019, MNRAS, 482, 3868
Ivezić, Ž., Goldston, J., Finlator, K., et al. 2000, AJ, 120, 963
Ivezić, Ž., Sesar, B., Jurić, M., et al. 2008, ApJ, 684, 287
Jayasinghe, T., Stanek, K. Z., Kochanek, C. S., et al. 2019, MNRAS, 485, 961
Kervella, P., Gallenne, A., Evans, N. R., et al. 2019a, A&A, 623, A117
Kervella, P., Gallenne, A., Remage Evans, N., et al. 2019b, A&A, 623, A116
Kim, Y. K., Lee, Y. S., & Beers, T. C. 2019, ApJ, 882, 176
Kinemuchi, K., Smith, H. A., Woźniak, P. R., McKay, T. A. & ROTSE Collaboration 2006, AJ, 132, 1202
Kinman, T., Castelli, F., Cacciari, C., et al. 2000, A&A, 364, 102
Kinman, T. D., & Brown, W. R. 2014, AJ, 148, 121
Kinman, T. D., Cacciari, C., Bragaglia, A., Buzzoni, A., & Spagna, A. 2007, MNRAS, 375, 1381
Kinman, T. D., Cacciari, C., Bragaglia, A., Smart, R., & Spagna, A. 2012, MNRAS, 422, 2116
Kinman, T. D., Suntzeff, N. B., & Kraft, R. P. 1994, AJ, 108, 1722
Koppelman, H. H., Helmi, A., Massari, D., Roelenga, S., & Bastian, U. 2019, A&A, 625, A5
Kunder, A., Bono, G., Piffl, T., et al. 2014, A&A, 572, A30
Kunder, A., Kordopatis, G., Steinmetz, M., et al. 2017, AJ, 153, 75
Lane, J. M. M., Bovy, J., & Mackereth, J. T. 2022, MNRAS, 510, 5119
Layden, A. C. 1994, AJ, 108, 1016
Layden, A. C. 1995, AJ, 110, 2288
Layden, A. C., Tiede, G. P., Chaboyer, B., Bunner, C., & Smitka, M. T. 2019, AJ, 158, 105
Lee, Y. S., Beers, T. C., Sivarani, T., et al. 2008, AJ, 136, 2022
Lindegren, L., Klioner, S. A., Hernández, J., et al. 2021, A&A, 649, A2
Liu, G. C., Huang, Y., Zhang, H. W., et al. 2020, ApJS, 247, 68
Liu, S., Du, C., Newberg, H. J., et al. 2018, ApJ, 862, 163
Lub, J. 1977, A&AS, 29, 345
Lucas, P. W., Hoare, M. G., Longmore, A., et al. 2008, MNRAS, 391, 136
Luongo, E., Ripepi, V., Marconi, M., et al. 2024, A&A, 690, L17
Mackey, A. D., Ferguson, A. M. N., Huxor, A. P., et al. 2019, MNRAS, 484, 1756
Magurno, D., Sneden, C., Braga, V. F., et al. 2018, ApJ, 864, 57
Magurno, D., Sneden, C., Bono, G., et al. 2019, ApJ, 881, 104
Mainzer, A., Bauer, J., Grav, T., et al. 2011, ApJ, 731, 53
Marconi, M., Coppola, G., Bono, G., et al. 2015, ApJ, 808, 50
Martínez-Vázquez, C. E., Monelli, M., Gallart, C., et al. 2016, MNRAS, 461, L41
Massari, D. 2025, RNAAS, 9, 64
Mateu, C., Vivas, A. K., Downes, J. J., et al. 2012, MNRAS, 427, 3374
McCarthy, I. G., Font, A. S., Crain, R. A., et al. 2012, MNRAS, 420, 2245
McMahon, R. G., Banerji, M., Gonzalez, E., et al. 2013, Msngr, 154, 35
McMahon, R. G., Banerji, M., Gonzalez, E., et al. 2021, yCat, II/367
McMillan, P. J. 2017, MNRAS, 465, 76
Medina, G. E., Hansen, C. J., Muñoz, R. R., et al. 2023, MNRAS, 519, 5689
Medina, G. E., Lemasle, B., & Grebel, E. K. 2021, MNRAS, 505, 1342
Medina, G. E., Li, T. S., Allende Prieto, C., et al. 2025b, arXiv:2505.10614
Medina, G. E., Li, T. S., Koposov, S. E., et al. 2025a, arXiv:2504.02924
Micali, A., Matteucci, F., & Romano, D. 2013, MNRAS, 436, 1648
Miceli, A., Rest, A., Stubbs, C. W., et al. 2008, ApJ, 678, 865
Minniti, D., Contreras Ramos, R., Zoccali, M., et al. 2016, ApJL, 830, L14
Monachesi, A., Gómez, F. A., Grand, R. J. J., et al. 2019, MNRAS, 485, 2589
Mullen, J. P., Marengo, M., Martínez-Vázquez, C. E., et al. 2021, ApJ, 912, 144
Mullen, J. P., Marengo, M., Martínez-Vázquez, C. E., et al. 2023, ApJ, 945, 83
Muraveva, T., Giannetti, A., Clementini, G., Garofalo, A., & Monti, L. 2025, MNRAS, 536, 2749
Neeley, J. R., Marengo, M., Freedman, W. L., et al. 2019, MNRAS, 490, 4254
Nemec, J. M., Cohen, J. G., Ripepi, V., et al. 2013, ApJ, 773, 181
Nemec, J. M., Smolec, R., Benkö, J. M., et al. 2011, MNRAS, 417, 1022
Nissen, P. E., & Schuster, W. J. 2010, A&A, 511, L10
Pagnini, G., Di Matteo, P., Khoperskov, S., et al. 2023, A&A, 673, A86
Pancino, E., Britavskiy, N., Romano, D., et al. 2015, MNRAS, 447, 2404
Parikh, T., Thomas, D., Maraston, C., et al. 2021, MNRAS, 502, 5508
Pietrukowicz, P., Kozłowski, S., Skowron, J., et al. 2015, ApJ, 811, 113
Pojmański, G. 1997, AcA, 47, 467
Pojmański, G. 2002, AcA, 52, 397
Pojmański, G. 2014, CoSka, 43, 523
Preston, G. W. 1959, ApJ, 130, 507
Preston, G. W. 1961, ApJ, 134, 633
Prudil, Z., Kunder, A., Dékány, I., & Koch-Hansen, A. J. 2024, A&A, 684, A176
Ratcliffe, B., Minchev, I., Anders, F., et al. 2023, MNRAS, 525, 2208
Romano, D., Karakas, A. I., Tosi, M., & Matteucci, F. 2010, A&A, 522, A32
Roškar, R., Debattista, V. P., Quinn, T. R., Stinson, G. S., & Wadsley, J. 2008, ApJL, 684, L79
Saha, A. 1985, ApJ, 289, 310
Saha, A., & Oke, J. B. 1984, ApJ, 285, 688
Sakari, C. M., Shetrone, M. D., McWilliam, A., & Wallerstein, G. 2021, MNRAS, 502, 5745
Sakari, C. M., Venn, K. A., Mackey, D., et al. 2015, MNRAS, 448, 1314
Sakari, C. M., & Wallerstein, G. 2022, MNRAS, 512, 4819
Salvadori, S., Schneider, R., & Ferrara, A. 2007, MNRAS, 381, 647
Samus', N. N., Kazarovets, E. V., Durlevich, O. V., Kireeva, N. N., & Pastukhova, E. N. 2017, ARep, 61, 80
Santucci, G., Brough, S., van de Sande, J., et al. 2023, MNRAS, 521, 2671
Sarajedini, A. 2024, MNRAS, 527, 11751
Sarajedini, A. 2025, AJ, 169, 154
Schlafly, E. F., & Finkbeiner, D. P. 2011, ApJ, 737, 103
Schönrich, R., Asplund, M., & Casagrande, L. 2011, MNRAS, 415, 3807
Searle, L., & Zinn, R. 1978, ApJ, 225, 357
Sesar, B., Jurić, M., & Ivezić, Ž. 2011a, ApJ, 731, 4
Sesar, B., Cohen, J. G., Levitan, D., et al. 2012, ApJ, 755, 134
Sesar, B., Grillmair, C. J., Cohen, J. G., et al. 2013, ApJ, 776, 26
Sesar, B., Stuart, J. S., Ivezić, Ž., et al. 2011b, AJ, 142, 190
Skrutskie, M. F., Cutri, R. M., Stiening, R., et al. 2006, AJ, 131, 1163
Sneden, C., Preston, G. W., Chadid, M., & Adamów, M. 2017, ApJ, 848, 68
Soszyński, I., Udalski, A., Szymański, M. K., et al. 2019a, AcA, 69, 87
Soszyński, I., Udalski, A., Wrona, M., et al. 2019b, AcA, 69, 321
Spitoni, E., Cescutti, G., Minchev, I., et al. 2019, A&A, 628, A38
Steinmetz, M., Zwitter, T., Siebert, A., et al. 2006, AJ, 132, 1645
Steinmetz, M., Matijevič, G., Enke, H., et al. 2020a, AJ, 160, 82
Steinmetz, M., Guiglion, G., McMillan, P. J., et al. 2020b, AJ, 160, 83
Stokes, G. H., Evans, J. B., Viggh, H. E. M., Shelly, F. C., & Pearce, E. C. 2000, Icar, 148, 21
Suntzeff, N. B., Kinman, T. D., & Kraft, R. P. 1991, ApJ, 367, 528
Suntzeff, N. B., Kraft, R. P., & Kinman, T. D. 1994, ApJS, 93, 271
Taam, R. E., Kraft, R. P., & Suntzeff, N. 1976, ApJ, 207, 201
Tissera, P. B., Beers, T. C., Carollo, D., & Scannapieco, C. 2014, MNRAS, 439, 3128
Tolstoy, E., Hill, V., & Tosi, M. 2009, ARA&A, 47, 371

Torrealba, G., Catelan, M., Drake, A. J., et al. 2015, MNRAS, 446, 2251
Vargas, L. C., Gilbert, K. M., Geha, M., et al. 2014, ApJL, 797, L2
Vasiliev, E. 2019, MNRAS, 484, 2832
Vivas, A. K., Zinn, R., & Gallart, C. 2006, RMxAC, 25, 37
Walker, A. R., & Terndrup, D. M. 1991, ApJ, 378, 119
Warren, S. J., Cross, N. J. G., Dye, S., et al. 2007, arXiv:astro-ph/0703037
Welsh, B. Y., Wheatley, J. M., Heafield, K., et al. 2005, AJ, 130, 825
Werner, M. W., Roellig, T. L., Low, F. J., et al. 2004, ApJS, 154, 1
Willett, E., Miglio, A., Mackereth, J. T., et al. 2023, MNRAS, 526, 2141
Wojno, J. L., Gilbert, K. M., Kirby, E. N., et al. 2023, ApJ, 951, 12
Wright, E. L., Eisenhardt, P. R. M., Mainzer, A. K., et al. 2010, AJ, 140, 1868
Xue, X.-X., Rix, H.-W., Ma, Z., et al. 2015, ApJ, 809, 144
Zhu, L., van den Bosch, R., van de Ven, G., et al. 2018, MNRAS, 473, 3000
Zinn, R., Chen, X., Layden, A. C., & Casetti-Dinescu, D. I. 2020, MNRAS, 492, 2161
Zinn, R., Horowitz, B., Vivas, A. K., et al. 2014, ApJ, 781, 22
Zoccali, M., Barbuy, B., Hill, V., et al. 2004, A&A, 423, 507
Zoccali, M., Quezada, C., Contreras Ramos, R., et al. 2024, A&A, 689, A240
Zolotov, A., Willman, B., Brooks, A. M., et al. 2009, ApJ, 702, 1058
Zolotov, A., Willman, B., Brooks, A. M., et al. 2010, ApJ, 721, 738